Optimization of point spread function of a high numerical aperture objective lens : application to high resolution optical imaging and fabrication

Qinggele Li

ENSC-2014 N° 285

Optimization of point spread function of a high numerical aperture objective lens:

Application to high resolution optical imaging and fabrication

Qinggele Li

A thesis presented for the degree of
Doctor of Philosophy

Jury

Jérôme PLAIN	Professor (LNIO, UTT Troyes)	Rapporteur
Denis GINDRE	Associate Professor (Univ. Angers)	Rapporteur
Henri BENISTY	Professor (Institut d'Optique)	Examinateur
Luc MUSEUR	Professor (Univ. Paris 13)	Examinateur
Isabelle LEDOUX-RAK	Professor (ENS Cachan)	Co-supervisor
Ngoc Diep LAI	Associate Professor (ENS Cachan)	Director

Laboratoire de Photonique Quantique et Moléculaire (UMR 8537 CNRS)

ÉCOLE NORMALE SUPÉRIEURE DE CACHAN

France

December 15, 2014

Résumé

Ce travail de thèse porte sur la caractérisation et l'optimisation du spot de focalisation d'un objectif de microscope de grande ouverture numérique pour des applications d'imagerie super-résolue et de nanofabrication.

Dans la première partie, nous avons systématiquement étudié les distributions de polarisation et d'intensité du faisceau laser dans la région du point focal en fonction de différents paramètres du faisceau incident tels que la phase, la polarisation, l'amplitude ainsi que l'influence du milieu de propagation, tel que l'indice de réfraction. Nous avons mis en oeuvre différentes méthodes théoriques pour contrôler et manipuler les distributions de polarisation et d'intensité du spot de focalisation. Ces prédictions théoriques sont vérifiées expérimentalement via un système optique confocal en mesurant l'image de fluorescence d'une nanoparticule d'or pour différentes caractéristiques.

Dans la seconde partie de ce travail, une nouvelle microscopie basée sur le mécanisme d'absorption ultra-faible à un photon a été démontré théoriquement et expérimentalement. Le calcul théorique basé sur l'approche vectorielle de Debye, qui prend en compte l'effet d'absorption du matériau, montre qu'il est possible de focaliser le faisceau lumineux en profondeur à l'intérieur d'un matériau si celui-ci présente une absorption linéaire ultra-faible à la longueur d'onde d'excitation. Cette méthode, dite (LOPA), a ensuite permis de fabriquer des structures 2D et 3D submicrométriques, similaires à celles obtenues par la méthode utilisant l'absorption à deux photons.

Abstract

Nowadays, far field optical microscopy is widely used in many fields, for fundamental research and applications. The low cost, simple operation, high flexibility are its main advantages. The key parameter of an optical microscope is the objective lens.

This thesis's work focuses mainly on the characterization and optimization of the point spread function (PSF) of a high numerical aperture (NA) objective lens (OL) for applications of high resolution imaging and nano-fabrication. In the first part of the thesis, we have systematically investigated the dependency of polarization and intensity distributions of the focusing spot on numerous parameters, such as the phase, the polarization, and the beam mode of incident beam, as well as the refractive index mismatch. Then, we demonstrated theoretically different methods for manipulation of the polarization and intensity distributions of the focusing spot, which can have desired shapes and are useful for different applications. By using a home-made confocal microscope, we have experimentally verified some of the theoretical predictions, for example, vector properties of light beam under a tight focusing condition. In the second part of dissertation work, a new, simple and inexpensive method based on the one-photon absorption mechanism has been demonstrated theoretically and experimentally for 3D sub-micrometer imaging and fabrication applications. The theoretical calculation based on vectorial Debye approximation and taken into account the absorption effect of material shows that it is possible to focus the light tightly and deeply inside the material if the material presents a very low one-photon absorption (LOPA) at the excitation wavelength. We have then demonstrated experimentally that the LOPA microscopy allows to achieve 3D imaging and 3D fabrication with submicrometer resolution, similar to those obtained by two-photon absorption microscopy.

List of publications (related to this work)

- **Q. Li**, M. T. Do, I. Ledoux-Rak and N. D. Lai, "*Concept for three-dimensional optical addressing by ultralow one-photon absorption method*," Opt. Lett. **38**, 4640-4643 (2013).
- M. T. Do, T. T. N. Nguyen, **Q. Li**, H. Benisty, I. Ledoux-Rak, and N. D. Lai, "*Submicrometer 3D structures fabrication enabled by one-photon absorption direct laser writing*," Opt. Express **21**, 20964-20973 (2013).
- **Q. Li**, M. T. Do, I. Ledoux-Rak and N. D. Lai, "*Three-dimensional optical addressing by ultra low one-photon absorption microscopy*," Proc. SPIE 9131(2014), doi: 10.1117/12.2051916.
- **Q. Li**, I. Ledoux-Rak and N. D. Lai, "*The influence of incident beam polarization on the intensity and polarization distribution of focusing spot*, " Advanced Device Materials, **1**, 1-7 (2014), http://www.maneyonline.com/ doi/full/10.1179/2055031614Y.0000000002.
- M. T. Do, **Q. Li**, I. Ledoux-Rak and N. D. Lai, "*Optimization of LOPA-based direct laser writing technique for fabrication of submicrometric polymer two- and three-dimensional structures*," Proc. SPIE 9127 (2014), doi: 10.1117/12.2051910.
- M. T. Do, **Q. Li**, T. T. N. Nguyen, H. Benisty, I. Ledoux-Rak, and N. D. Lai, "*High aspect ratio submicrometer two-dimensional structures fabricated by one-photon absorption direct laser writing*," Microsystem Technologies (Springer-Verlag) **20**, 2097–2102 (2014).
- T. T. N. Nguyen, M. H. Luong, M. T. Do, D. M. Kieu, **Q. Li** , D. T. T. Nguyen, Q. C. Tong, I. Ledoux-Rak, N. D. Lai, "*Micro and nanostructuration of polymer materials and applications*," Proc. SPIE 9171 (2014), doi:10.1117/12.2064653.

Conference contributions

- **Q. Li**, M. T. Do, I. Ledoux-Rak and N. D. Lai, "*Three-dimensional optical addressing by ultra low one-photon absorption microscopy,*" SPIE Photonic Europe, Brussels, Belgium (May 2014), Oral.
- **Q. Li**, M. T. Do, I. Ledoux-Rak and N. D. Lai, "*3D imaging by low one-photon absorption technique*," CLEO/Europe-IQEC, Munich, Germany (May 2013), Poster.
- **Q. Li**, M. T. Do and N. D. Lai, "*Generation of sharper focal spot for super-resolution imaging and nanofabrication*," The French Japanese Workshop-The Nanotech Revolution from Science to Society, Cachan, France (December 2011), Poster.
- **Q. Li**, M. T. Do, I. Ledoux-Rak and N. D. Lai, "*LOPA microscopy for 3D imaging and 3D fabrication,*" journée de l'IDA, ENS Cachan, France (May 2014), Oral.
  M. T. Do, **Q. Li**, I. Ledoux-Rak. I, and N. D. Lai, "*Optimization of LOPA-based direct laser writing technique for fabrication of submicrometric polymer threedimensional structures,*" SPIE Photonic Europe ,Brussels, Belgium (May 2014), Oral.
- M. T. Do, **Q. Li**, T. T. N. Nguyen, H. Benisty, I. Ledoux-Rak, and N. D. Lai, "*One-photon absorption direct laser writing: a novel approach for fabrication of three-dimensional sub-micrometric structures,*" CLEO/Europe-IQEC, Munich, Germany (May 2013), Oral.
- M. T. Do, **Q. Li**, T. T. N. Nguyen, H. Benisty, I. Ledoux-Rak, I, and N. D. Lai, "*Fabrication of sub-micrometer 3D structures by one-photon absorption direct laser writing,*" The 6th International Workshop on Advanced Materials Science and Nanotechnology (IWAMSN2012), Ha Long Bay, Vietnam (November 2012), Poster.
- M. T. Do, **Q. Li**, Nguyen, T. T. N., Benisty, H., Ledoux-Rak, I., and N. D. Lai, "*Ultra low one-photon absorption (LOPA) microscopy and applications,*" MEP1-O1, The 6th International Workshop on Advanced Materials Science and Nanotechnology (IWAMSN2012), Ha Long Bay, Vietnam (November 2012), Invited Talk.

Contents

PSF ..... point spread function

NA ..... numerical aperture

$\boldsymbol{n}$ ..... refractive index

OL ..... objective lens

OPA ..... one-photon absorption

AMOL ..... absorption modulation optical lithography

CLSM ..... confocal laser scanning microscopy

FDTD ..... finite-difference time-domain

L-G ..... Laguerre-Gaussian

TPA ..... two-photon absorption

AR ..... aspect ratio

FWHM ..... full width at half maximum

LOPA ..... low one-photon absorption

DLW ..... direct laser writing

EM ..... electromagnetic

STED ..... stimulated emission depletion

General introduction

Since its invention in the early seventeen centuries, the optical microscope has caught much attention from researchers for its easy operation processing, remarkable focusing spot size, and interesting applications. The principle of optical microscopy is based on the use of an optical lens to investigate the interested material. Recently, the existence availability of high numerical aperture (NA) objective lenses (OL) and their use in combination with different laser beam modes and optical masks has allowed light to be tightly focused into a sub-micrometer [1] or even a nanoscale spot [2, 3]. Focusing spots with a small size have being used in many domains, including physics, biology, information, medical and material science.

In particular, sub-wavelength focusing spot becomes an extremely important tool for optical data storage [4], nano-imaging [5], nano-fabrication [6, 7], as well as optical trapping and optical acceleration [8, 9].

Optical microscopy for imaging and fabrication

In spite of the development of high resolution SEM (scanning electron microscope), STM (scanning tunneling microscope), and AFM (atomic force microscope), optical microscopy still plays an important role in optical imaging, optical lithography and optical manipulation because of its easy operation and low cost.

As compared to wide field microscopy [10], the invention of confocal microscope, which is designed for eliminating the out of focus signal by introducing a pinhole in the detecting system, has greatly enhanced the optical microscope resolution, in particular the axial sectioning capability. Nowadays, in a confocal system based on a high NA OL, light can be tightly focused into a sub-micrometer scale, and thus

its resolving power is significantly increased. Generally, the confocal microscope is based on an one-photon absorption (OPA) mechanism, using a low cost and continuous laser whose wavelength is centered in the high absorption range of studied material. However, under tight focusing conditions, the tiny focusing spot is very sensitive to many parameters, which are correlated to the incoming light and also to the used OL. *A Better understanding of these parameters and the capacity to perform a desired focal shape are very important for applications.*

Besides, in practice, the studied material and also the experimental environment often degrade the quality of focusing spot. One of the most critical influences is the limited penetration depth of confocal microscope [1], caused by material absorption. Hence, the conventional confocal microscope does not allow to deal with deep tissue imaging and 3D fabrication of photonic structures.

In contrast to the conventional confocal microscope, the two-photon absorption (TPA) microscope presents a better axial resolution. In this case, the sample is selectively and efficiently excited only at the focal spot of a microscope objective, owing to the quadratic dependence of the material response with respect to the excitation intensity. By manipulating the focusing spot, complex 3D imaging or fabrication can be realized [11]. However, because of the nonlinear process, which only happens with very high excitation intensity, TPA requires a pulsed femtosecond or picosecond high power laser. Hence, this technique is rather expensive and complicated. *A method that is simple and low cost allowing to achieve 3D imaging and 3D fabrication as those obtained by TPA microscopy is a high demand.*

Super-resolution microscopy

In a standard microscopy, due to diffraction, which is the wave-nature of light, its resolving power is restricted to a half of the wavelength of the incoming light beam. To overcome this diffraction barrier and to observe or to manipulate single molecule or to fabricate nano-structures is a challenging task. For more than hundred years, researchers have been working to get a focusing spot size below the diffraction limit. Unfortunately, no remarkable progress has been made and the diffraction limit remained as a barrier limiting the optical microscopy applications. In 1984, the invention of the “scanning near field optical microscopy” (SNOM) [12] overcame the diffraction limit for the first time. However, in practice, this technique can only be suitable for some specific applications due to the working principle of contact

scanning. Thereafter, in the last decades, several fantastic super-resolution optical microscopes, based on far field optics have been proposed, such as stimulated emission depletion (STED) microscopy [2], absorption modulation optical lithography (AMOL) [13]. In principle, these techniques use two light sources, one for excitation, and the other one, which has a doughnut shape in the focal region, being used to suppress the "action" of the Airy spot of the first beam to achieve an effective Airy spot, which is much smaller than the diffraction limit. For the generation of doughnut spot in the focal region, a vortex plate [14] is often employed. The intensity distribution obtained from vortex mask has a transversal doughnut shape. Hence, in those methods, the resolution is enhanced mainly along lateral directions. The axial resolution remains in the sub-micrometer scale, which is similar to that of the standard confocal microscope. To improve axial resolution, some methods [15, 16] have been proposed by introducing of a third light source, which is modulated by a 0/pi phase plate to perform a longitudinal doughnut field distribution in the focal region. Hence, with the combination of transverse and longitudinal doughnut spots, 3D super-resolution can be obtained. In practice, due to the using of three laser beams, which need to overlap each other perfectly in the focal region, it requires a very complex optical system with a highly challenging optical alignment. *Therefore, using a simple method to effectively generate a 3D doughnut focusing spot is highly desired in the field of 3D super-resolution microscopy.*

Motivation and thesis outline

The aim of this thesis is to theoretically and experimentally investigate behaviour of a focusing spot under tight focusing condition and its optimization for the applications in the field of optical imaging and nano-fabrication. We target to quantitatively characterize the effects of polarization, phase and beam mode of incident beam, as well as the refractive index mismatch, on the polarization and intensity distributions of the focusing spot. Besides, we also aim to investigate simple and effective methods for the generation of a focusing spot with highly modulated intensity or polarization distribution, for example the generation of long needle, long dark channel, flattop focusing spot, as well as 3D isotropic doughnut focusing spot. Furthermore, in order to take advantage of both OPA and TPA microscopies, we focus on the investigation of a new type of optical microscopy, at low cost and a simple optical configuration, but allowing to achieve 3D imaging and 3D nano-fabrication.

The thesis is organized as follows:

In chapter 1, we introduce a general vector theory of the point spread function (PSF) of a high NA OL and the numerical calculation method allowing to obtain exact optical behaviour in the focal region. Then, we investigate in detail the influence of different parameters, such as NA of OL, polarization of incident beam, incident beam mode, optical mask (phase, amplitude), refractive index mismatch, on the intensity and polarization distributions of light beam in the focal region.

In chapter 2, we propose different theoretical ways to realize various shapes of the focusing spot, which are interesting for many applications. We show that, by controlling the phase, amplitude and polarization of an incident beam, it is possible to generate some particular field distributions, such as long-needle, long dark-channel or flattop focusing spots. We also demonstrate a method to achieve an isotropic focusing (a spherical focusing spot) by employing a particular double-hole mask.

In chapter 3, we demonstrate how to achieve 2D and 3D super-resolution optical microscopy. We investigate in detail the 2D stimulated emission depletion (STED) microscopy and the absorbance-modulation optical lithography (AMOL). We then introduce a general concept of a so-called "nano-pointer", which is interesting for 2D optical fabrication application. In addition, a new method for the creation of a 3D doughnut focusing spot, which could be used for 3D super-resolution STED microscopy, is also presented.

In chapter 4, by using a simple home-made confocal microscope and a gold nanoparticle as a probe bead, we experimentally characterize the field distribution in the focal region of high NA OLs. We also demonstrate the general behaviours of lens system, such as the influence of NA, the misalignment of the optical system, aberration effects, etc. Moreover, we demonstrate the influence of the input beam polarization on the intensity distribution in the focal region, and show how to control the focusing spot shape.

In chapter 5, based on the vectorial Debye theory, we further establish a new mathematics representation, in which the absorption effect of the studied material has been taken into account. This allows to explain the variation of light beam propagating through an absorbing medium. We quantitatively carry out the influence of the absorption coefficient of the studied material and the penetration depth of light

beam on the formation of a tight focusing spot. Furthermore, we propose for the first time a new concept of submicrometer 3D microscopy, entitled "low one-photon absorption microscopy" (LOPA), which is very useful for 3D optical imaging and 3D optical fabrication. LOPA microscopy concept is experimentally verified by using a simple fluorescence experimental method, and also by the demonstration of the successful fabrication of various 2D and 3D sub-micrometer structures.

In the last chapter, we summarize all important results of this work and show how they could be useful for different applications in optical imaging and fabrication. We also discuss about different prospects of this work.

Chapter 1

Fundamental study of light distribution in the focal region of a high NA OL

High spatial resolution is an essential requirement of imaging microscopes, such as confocal laser scanning microscopy (CLSM), near-field scanning optical microscopy (SNOM), scanning electron microscopy (SEM) and scanning tunneling microscope (STM), etc. Depending on the imaging system and a target sample properties, the resolving power can range from 1 μm down to 10^{-10} m. The resolution of a standard optical microscope (far-field) is limited at sub-micrometer scale. This limitation of the optical microscopy resolution is mainly caused by the well-known "diffraction limit", which is the consequence of the wave property of light.

In this chapter, we discuss about the behavior of the diffraction-limited focusing spot of a lens used in an optical microscope. First, a brief introduction of the diffraction theory and numerical computing methods used to calculate the electromagnetic (EM) field distribution in the focal region will be presented. Then, we investigate the effect of numerous parameters on the intensity distribution of a diffraction limited focusing spot, such as the NA of OL, the polarization and phase distributions of the incident light beam, etc.

1.1 Diffraction of light in a lens system

Diffraction is the wave nature of light [17]. When light encounters a "small" (size is close to light wavelength) object (transparent or opaque), a significant diffraction phenomenon is observed. As a consequence, instead of projected shadow of object, the intensity distribution, on the screen placed at the back side of the object, has rings or fringes shape. The diffraction effect was first theoretically proposed by Huygens and was further investigated by Fresnel [17]. The experimental observation of diffraction phenomena is referenced to the famous "Young's single and double slits experiment".

Diffraction is employed to explain numerous phenomena, for example, the interaction of light with a grating structure and the light behavior under tight focusing. It is well-known that, even with a perfect lens, it is impossible to obtain an ideally focused point. Figure 1.1 illustrates the propagation of a light beam, which is tightly focused by an aberration-free high NA OL. In the focal region, the focusing spot, instead of an ideal point, displays an ellipsoidal shape, with a rotational symmetry along the optical axis. The dimension of the focal spot is characterized by the so-called longitudinal (L) and transverse (T) size. The ratio L/T is often defined as its aspect ratio (AR).

The reason for the limited size (T, L) of the focusing spot is due to the diffraction when propagating through a lens aperture. Indeed, as any kind of diffraction aperture (*i.e.*, a slit, a rectangular hole), a lens pupil is considered as a diffracting aperture, which is constituted by infinite diffracting points. In the vicinity of the focal region, the EM field distribution is the superposition of all diffracted light rays that emerged from lens aperture. The focusing spot is therefore an interference image of all these rays, resulting in a finite size that cannot be reduced below the wavelength of the incident light.

1.1.1 Rayleigh criteria

The size and shape of the focusing spot has a direct impact on the resolving power of an optical microscope. For instance, the image of a point object on the camera is an image of the focusing spot, which is described as a so-called point spread function (PSF). If there are two points located in the focal region, which are close

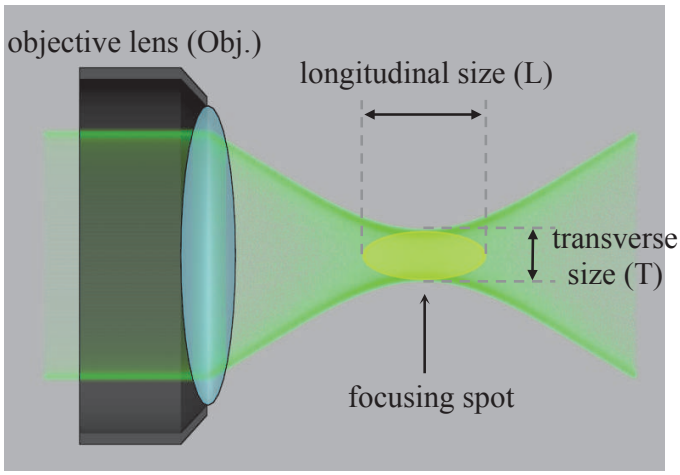

Figure 1.1: Light propagation under tight focusing condition by a high NA OL. The focusing spot sizes, T and L, are defined at full width at half maximum (FWHM) of its peak intensity along the transverse and longitudinal directions, respectively.

enough to each other, the relevant PSFs merge into each other and we no longer can distinguish the images of these points on the camera. Furthermore, in the case of an optical lithography, which is based on the use of a focused beam, it is not possible to fabricate a structure with a feature size smaller than the focusing spot size. The exact definition of focusing spot size or minimum resolvable distance is the most essential issue in optical microscope system. The mathematics representation of resolution is referred to two kinds of formulas, which are proposed by Abbe and Rayleigh [17], respectively. The two formulae are quite similar. The only difference is the coefficient of terms, which comes up from the different definitions of the minimum resolvable distance of two close point objects. In an imaging system, Rayleigh criteria is often considered as a standard definition. In this case, the minimum resolvable distance between two points is the distance in which the maximum intensity of relevant PSF of the first point is just overlapped with the first minimum of the PSF of second point. This distance is equal to half of a single PSF size. In the Rayleigh criteria, the transverse and longitudinal minimum distances are given as [17]: - *for the transverse (lateral) size*:

$$\mathrm{T}/2 = \frac{0.61\lambda}{\mathrm{NA}} \ , \tag{1.1}$$

- *for the longitudinal (axial) size*:

$$\mathrm{L}/2 = \frac{2\lambda}{\mathrm{NA}^2} \ , \tag{1.2}$$

where λ is the wavelength of light, NA is the numerical aperture of OL, which is defined as:

$$\mathrm{NA} = n \sin \alpha, \tag{1.3}$$

where n is the refractive index of the medium in which the light propagates, and α is half of the maximum angle through which the light is focused into the focal region.

According to these formulae, the resolution of an optical imaging system is referred to light wavelength, λ, and the NA of the used OL. For higher NA, smaller focusing spot and better resolution can be obtained. To be a high NA, one can increase the α-angle or use an immersed medium with higher refractive index, n. Therefore, there exist actually different kinds of OLs, classified as air ($n = 1$), water ($n = 1.33$), and oil ($n = 1.51$) immersion OLs, as well as solid ($n > 2$) immersion OL [18]. Nowadays, OLs with NAs varying from 0.2 to 1.65 are commercially available.

In order to achieve tightly localized field or a better resolving power, high NA OLs are often employed in optical systems. We note that the Rayleigh criteria (Eqs. (1.1), (1.2)) is determined based on the intensity profile of Airy disk, which is the diffraction pattern of a circular aperture. This diffraction is quantitatively studied by using the Fresnel-Kirchhoff scalar diffraction theory, in which the vector properties of light are omitted and the direction of energy flow (Poynting vector) is also ignored. Hence, Eqs. (1.1), (1.2) only partially reflect the behavior of focusing spot size. However, when working with an optical system possessing a high NA OL, there are numerous fascinating phenomena, which can be emerged, such as hollow focusing structures, asymmetric focusing behavior, etc. A diffraction theory taking into account the vectorial property of incident light is therefore necessary.

In the next section, we will discuss about the derivation of an exact mathematics representation of intensity distribution of the focusing spot under tight focusing condition.

1.1.2 Light distribution in the focal region of a high NA OL

In an optical imaging system, if the NA of OL is relatively high (> 0.7), as shown in Figure 1.2, the wavefront (w_i) of light beam at the exit of objective is converged significantly and turned into a spherical form. Hence, the approximations taken in

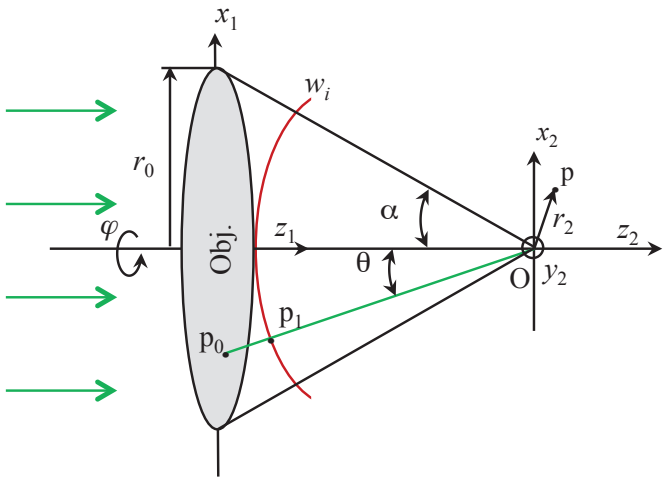

Figure 1.2: Geometrical representation of the propagation of a light wave, focused by a high NA (NA > 0.7) OL. The red curve represents the wavefront w_i of propagation beam at the exit of objective pupil. Subscripts 1, 2 in the Cartesian coordinates indicate the coordinates of lens (object) and focal region (image), respectively.

the scalar diffraction theory, such as paraxial approximation, Kirchhoff boundary condition, Fresnel or Fraunhofer approximation [19] are no longer satisfied. The corresponding derived results are not able to exactly reflect the behavior of the light field distribution in the vicinity of a focal point. In 1950's, Richard and Wolf proposed a complete mathematics representation of EM field distribution in the focal region of a high NA OL. The proposed formula considers the vector properties of the EM field, and the derivation is based on vectorial Debye approximation. The main idea of this theory can be summarized as follows [19, 20] :

i) the beam wavefront just after exit pupil has a spherical shape (Gaussian reference sphere) with a radius of f that is called the focal length of OL.

ii) each diffracted light ray is considered as a plane wave and propagates towards the geometrical focal point of lens, indicated by the wave vector, $\mathbf{k}$.

iii) $\cos(\theta,\ \mathbf{n}) \approx 1$, where $\mathbf{n}$ is the normal vector of diffraction aperture and θ is the angle of the propagation direction of diffracted ray and the optical axis.

Following Richard and Wolf, the electric field distribution at an arbitrary point p (Figure 1.2) in the focal region is given in Cartesian coordinates [20, 21] by:

$$\mathbf{E} = -\frac{ik\mathrm{C}}{2\pi}\iint_{\Omega}\mathbf{T}(s)\exp[ik(\Phi(s_x, s_y) + s_x x_2 + s_y y_2 + s_z z_2)]\mathrm{d}\Omega, \tag{1.4}$$

where C is a constant, $k = 2\pi n/\lambda$ is the wavenumber, λ is the wavelength of incident light, n is the refractive index of the immersion medium, and Ω is a solid angle of the objective aperture. Only inside this Ω angle, diffracted light rays are considered as propagating towards the focal point and contribute to the formation of a tight focusing spot. $\mathbf{s} = (s_x, s_y, s_z)$ is a dimensionless vector along a typical ray pointing towards the geometrical focal point O. $\Phi(s_x, s_y)$ is the wavefront distortion with respect to the Gaussian reference sphere in the case of aberration. In our calculation, it has been assumed as zero for an aberration-free focusing system, except for the case dealing with dielectric interface, which will be presented in Section 3.5 of this chapter. $\mathbf{T}(s)$ refers to the amplitude distribution of light at the exit of the objective pupil. The exact expression of this term is quite complicated, because it depends on different parameters, such as the apodization of the objective pupil and the input field vector. It will be expressed in detail in spherical coordinates in the later part of this chapter.

The physical interpretation of the Eq. (1.4) is that the EM vectorial field distribution at an arbitrary point $\mathrm{p}(x_2, y_2, z_2)$ in the focal region of a high NA OL is the superposition of all the diffracted plane waves ($\mathbf{s}$) which are emerged from exit of lens within the solid angle Ω. Moreover, the field amplitude of plane waves ($\mathbf{s}$), have direct relation with the employed lens and the incident vector beam.

In the general case, an OL aperture has a circular shape. The wavefront (w_i) of the diffracted beam at the exit of objective aperture is axially symmetric around the optical axis. Thus, it is convenient to express the wave vector $\mathbf{s}$ by introducing the spherical coordinates [22, 23]:

$$\mathbf{s} = (\sin\theta\cos\varphi, \sin\theta\sin\varphi, \cos\theta), \tag{1.5}$$

with $0 < \theta < \alpha$, where α is the maximum focusing angle of the OL (Figure 1.2), and φ is the azimuthal angle of object plane. We note that, in some cases, in order to compute the particular distribution of the wavefront, we also use Cartesian coordinates to express the unit vector $\mathbf{s}$ (see Section 2).

Besides, the solid angle Ω [22] can be expressed in Cartesian and spherical coordinates as:

$$\mathrm{d}\Omega = \frac{\mathrm{d}s_x \mathrm{d}s_y}{s_z} = \sin\theta \mathrm{d}\theta \mathrm{d}\varphi. \tag{1.6}$$

In our study, for the image plane, we use Cartesian coordinates to conveniently

express the intensity distribution at $(x_2y_2)-$, $(x_2z_2)-$, $(y_2z_2)-$planes of the focal region.

Substituting Eqs. (1.5) and (1.6) into Eq. (1.4), the diffraction integral formula therefore can be rewritten as [24] :

$$\mathbf{E}(x_2,y_2,z_2) = -\frac{i\mathrm{C}}{\lambda}\int_0^{\alpha}\int_0^{2\pi}\sin\theta \mathrm{A}(\theta,\varphi)\mathrm{B}(\theta,\varphi)\mathbf{P}(\theta,\varphi) \times \exp[ikn(z_2\cos\theta + x_2\sin\theta\cos\varphi + y_2\sin\theta\sin\varphi)]\mathrm{d}\theta\mathrm{d}\varphi, \quad (1.7)$$

where :

- $\mathrm{A}(\theta,\varphi)$ is the amplitude of the incident beam, referring to the beam profile (mode) of the incident laser beam. For example, in the case of a uniform beam, $\mathrm{A}(\theta,\varphi) = 1$. If there is a mask (phase or intensity modulation optical component)is placed in front of OL, this term will be accordingly modified. The influence of this term on the field distribution in the focal region will be discussed in Sections 3.2 and 3.3.

- $\mathrm{B}(\theta,\varphi)$ is the apodization factor, which indicates the energy conservation before and after lens aperture. In an aplanatic lens system, $\mathrm{B}(\theta,\varphi) = \sqrt{\cos\theta}$ [21].

- $\mathbf{P}(\theta,\varphi)$ indicates the polarization state of the EM field in the focal region. It is expressed as $\mathbf{P}(\theta,\varphi) = \mathrm{T}(\theta,\varphi)\mathbf{P_0}(\theta,\varphi)$, where $\mathbf{P_0}(\theta,\varphi)$ is a matrix vector related to the polarization of the input light and $\mathrm{T}(\theta,\varphi)$ is a 3×3 lens operator matrix to convert the polarization from object field to focal region. The mathematics form of the polarization of the input field can be expressed as:

$$\mathbf{P}_0 = \begin{bmatrix} \mathrm{p}_x(\theta,\varphi) \\ \mathrm{p}_y(\theta,\varphi) \\ \mathrm{p}_z(\theta,\varphi) \end{bmatrix}. \quad (1.8)$$

The lens operator matrix can be calculated by:

$$\mathrm{T}(\theta,\varphi) = R^{-1}CR, \quad (1.9)$$

with

$$R = \begin{bmatrix} \cos\varphi & \sin\varphi & 0 \\ -\sin\varphi & \cos\varphi & 0 \\ 0 & 0 & 1 \end{bmatrix}, C = \begin{bmatrix} \cos\theta & 0 & \sin\theta \\ 0 & 1 & 0 \\ -\sin\theta & 0 & \cos\theta \end{bmatrix}, \quad (1.10)$$

where R, C describe the rotation of the coordinate system around the optical axis

and the change of polarization during the propagation through the lens [23], respectively. We note that $\mathrm{T}(\theta, \varphi)$ only indicates the polarization conversion of the incident beam in the case of homogeneous medium. If there is any dielectric interface after the lens aperture, Fresnel coefficients must be introduced to take into account the different transmissions of different polarizations (see Section 3.5).

Thus, by using Eq. (1.8), Eq. (1.9) and Eq. (1.10), the polarization states of the field in the focal region, $\mathbf{P}(\theta, \varphi)$, can be rewritten as :

$$\mathbf{P}(\theta,\varphi) = \begin{bmatrix} 1+(\cos\theta-1)\cos^2\varphi & (\cos\theta-1)\cos\varphi\sin\varphi & -\sin\theta\cos\varphi \\ (\cos\theta-1)\cos\varphi\sin\varphi & 1+(\cos\theta-1)\sin^2\varphi & -\sin\theta\sin\varphi \\ \sin\theta\cos\varphi & -\sin\theta\sin\varphi & \cos\theta \end{bmatrix} \begin{bmatrix} \mathrm{p}_x(\theta,\varphi) \\ \mathrm{p}_y(\theta,\varphi) \\ \mathrm{p}_z(\theta,\varphi) \end{bmatrix}. \tag{1.11}$$

The influence of the incident beam polarization on the intensity distribution of a tight focusing spot was theoretically studied and will be presented in Section 3.4. The corresponding experimental investigation will be presented in Chapter 3.

Based on this vectorial Debye theory, for a light beam focused by a high NA OL, we can see that the EM field distribution in the focal region depends on various parameters, such as, the input laser beam mode, the polarization of incident light, the NA of OL, etc. In the next section, we will present a numerical method to calculate the exact intensity and polarization distributions of a tight focusing in the focal region, as well as the influence of different input parameters.

1.2 Numerical calculation method & simulation script based on Matlab

In principle, there are an infinite number of diffracted rays within the range of the θ ($0 \leq \theta \leq \alpha$) and φ angles ($0 \leq \varphi \leq 2\pi$), which emerge from lens aperture and propagate toward to the focal region. However, dealing with an infinite number rays is not practical. For numerical computing, considering the time needed for calculation, and accuracy tolerance, an appropriate limit amount of diffracted rays should be adopted.

Hence, for numerical computing, we assume that the angle θ is discretized from 0 to α by an equally spacing step of $\Delta\theta$, and accordingly, the azimuthal angle φ is discretized from 0 to 2π by a equally spacing step of $\Delta\varphi$. In the simulation program,

we assume that θ is discretized by N_θ linear steps as:

$$\begin{aligned}
&\theta_1 = 0, \\
&\theta_m = \theta_{m-1} + \Delta\theta, \ (1 \leq m \leq \mathrm{N}_\theta, \text{ integer}), \\
&\Delta\theta = \alpha/\mathrm{N}_\theta,
\end{aligned}$$

and the azimuthal angle φ is discretized by N_φ linear steps as:

$$\begin{aligned}
&\varphi_1 = 0, \\
&\varphi_n = \varphi_{n-1} + \Delta\varphi, \ (1 \leq n \leq \mathrm{N}_\varphi, \text{ integer}), \\
&\Delta\varphi = 2\pi/\mathrm{N}_\varphi.
\end{aligned}$$

Consequently, the integration formula (Eq. (1.7)) may be simplified by summing up a quite number of plane waves. It can be written by a numerical computing way as:

$$\begin{aligned}
\mathbf{E}(x_{2_i}, y_{2_j}, z_{2_k}) = &\sum_{m=1}^{N_\theta} \sum_{n=1}^{N_\varphi} \sin\theta_m \mathrm{A}(\theta_m, \varphi_n)\mathrm{B}(\theta_m, \varphi_n)\mathbf{P}(\theta_m, \varphi_n) \\
&\times \exp[ikn(z_{2_k}\cos\theta_m + x_{2_i}\sin\theta_m\cos\varphi_n + y_{2_j}\sin\theta_m\sin\varphi_n)]\Delta\theta\Delta\varphi. \qquad (1.12)
\end{aligned}$$

Besides, similar to finite-difference time-domain (FDTD), the area of interest (observation plane) is assumed to be a 3D grid distribution (N_x, N_y, N_z) with a spacing size less than $\lambda/10$. In our case, these parameters are set, for example, as N_θ=N_φ=200, N_x=N_y=N_z=200, for a high NA OL ($\alpha \approx 67.5°$), and for a simulation region of 0.5 μm $\times$ 0.5 μm $\times$ 0.5 μm.

In this study, the numerical calculation way is programmed by a personal code script based on Matlab software. The detail of the script is attached in Appendix A.

Furthermore, for convenience, we have packaged numerous scripts into a graphic interface package. The representation of the software is shown in Figure 1.3. This package allows to simulate intensity and polarization distributions of a tightly focused spot under different conditions, such as different NAs of OL, different incident beam polarizations, different beam modes, etc. The detail of these studies will be presented in the next Section.

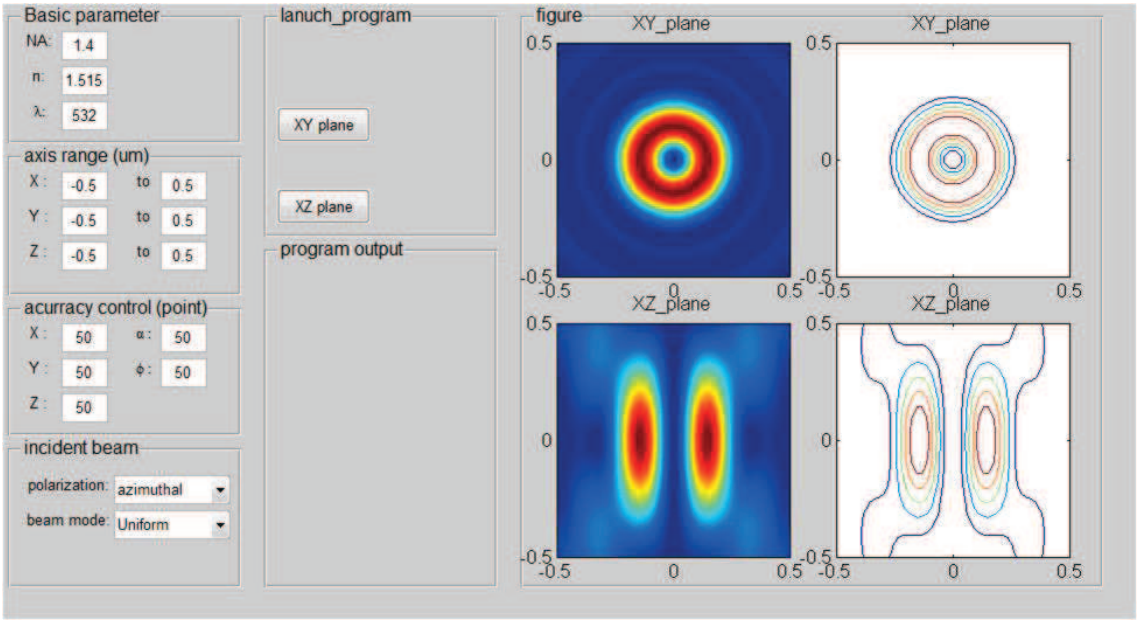

Figure 1.3: Graphic interface of the developed software, which is used to systematically study the intensity and polarization distributions of a tight focusing spot.

1.3 Fundamental study of EM field distribution in the focal region

In this section, the basic properties of a tight focusing spot is presented in detail.

1.3.1 EM field distribution in the focal region as a function of NA

As mentioned in the definition of the Rayleigh criteria, the NA of OL is a crucial parameter for characterizing the optical imaging system. NA is proportional to the maximum opening angle (α) of the OL. NA also depends on the refractive index (n) of the immersion medium, as shown in Figure 1.4. In this work, as shown in the first row of Table 1.1, we have theoretically studied the intensity distribution in the focusing region of six different OLs. All these OLs possess high NAs, and are immersed in different media (air, water and oil). In simulation, we have assumed that the incident beam is right circularly polarized and that the light source is monochromatic with wavelength $\lambda = 532$ nm.

The numerical calculations of the focusing spot at $(x_2y_2)-$plane (z_2=0) are shown

NA	0.7	0.9	1.1	1.25	1.4	1.49
n	1.0	1.0	1.33	1.33	1.51	1.51
α (°)	44.42	64.16	55.80	70.03	67.53	80.66

Table 1.1: Different NAs and corresponding α-angles used to calculate the intensity distribution in the focal region. The refractive index of immersed medium is changed according to each OL.

in Figure 1.4. It is clear that, in all cases, the transverse size of the focusing spot is symmetric around the optical axis, and its size is decreased when NA increases.

Figure 1.5 shows the intensity distribution of the focusing spot at $(x_2 z_2)-$plane. We can see a dramatic decrease of the focal spot size along the longitudinal direction when increasing of NA of the OL. Following a relation similar to that of the Rayleigh criteria (Eq. (1.2)). In spite of this dramatic decreasing rate, the longitudinal size (L) is always larger than that of the transverse direction (T). This is due to the fact that in a focusing system with the use of a single OL, it is only able to focus or collect the light in one direction (propagating along z_2-axis) with omitting the light (information) from other directions. In order to further reduce the longitudinal focal size, one possibility is to use a 4-pi configuration optical path [25], in which a second OL is placed at the opposite side of the first one to modulate the light field along the optical axis of the system.

The calculated values of the full width at half maximum (FWHM) of the transverse (T) and longitudinal (L) sizes of the focusing spot are shown in Figure 1.6(a). It is clear that the longitudinal size decreases dramatically from 1.6 μm to about 0.4 μm while the transverse direction decreases from 0.4 μm to 0.20 μm. By companying the focusing spot sizes of different media, we found that the size of NA=1.1 ($n = 1.33$) is smaller than the air objective with NA = 0.9 ($n = 1$), despite the α angle is smaller. That is due to the fact that the wavelength in dense medium is shorter. The aspect ratio (L/T) of the focusing spot is shown in Figure 1.6(b). It also decreases down to around 2 at NA=1.49. Further reduction of this ratio is quite important for many applications. Indeed, 3D imaging and 3D optical fabrication, requires the same resolution along all directions. The study of isotropic 3D intensity distribution of focusing spot will be presented in Chapter 3.

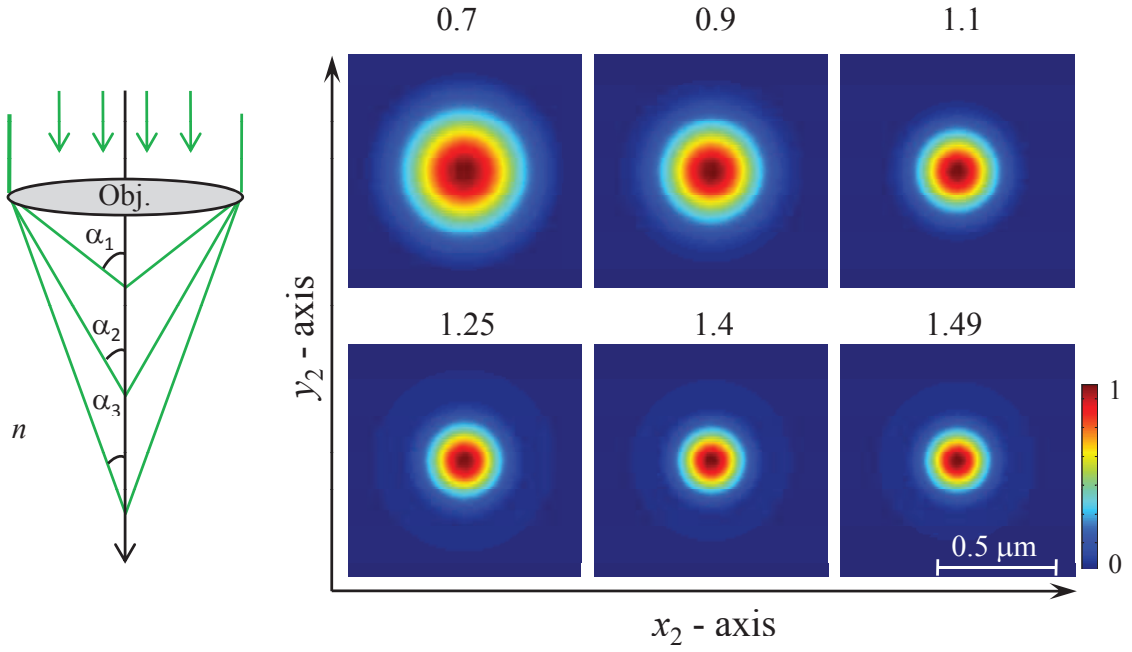

Figure 1.4: Transversal intensity distribution of the focusing region as a function of the NAs (see Table 1.1). $NA_{1,2,3...}$=nsin($\alpha_{1,2,3...}$)Results are obtained by using a circularly polarized uniform beam with $\lambda = 532$ nm.

We note that the theoretical FWHM size of the focusing spot is smaller than the value predicted by the Rayleigh criteria (1.22λ/NA). This reflects the difference of scalar diffraction and vectorial Debye theories. For a rough estimation of the ffocusing spot size, both theories are acceptable, but in the case of high resolution imaging and nano-fabrication, the correct calculation from vectorial Debye theory should be employed.

1.3.2 Effect of the input beam profile on form and size of focusing spot

Because the laser beam is often employed as a light source, it is important to characterize the focusing behavior of different laser beams under tight focusing conditions. Up to now, the most frequently reported results of laser beams are referred to Gaussian beam [26], Bessel-Gaussian beam [27] and Laguerre-Gaussian beam [28]. In this section, we study the effect of the three kinds of input beam modes on the intensity distribution of the focusing spot, which are: *uniform*; *Gaussian*; and *Laguerre-*

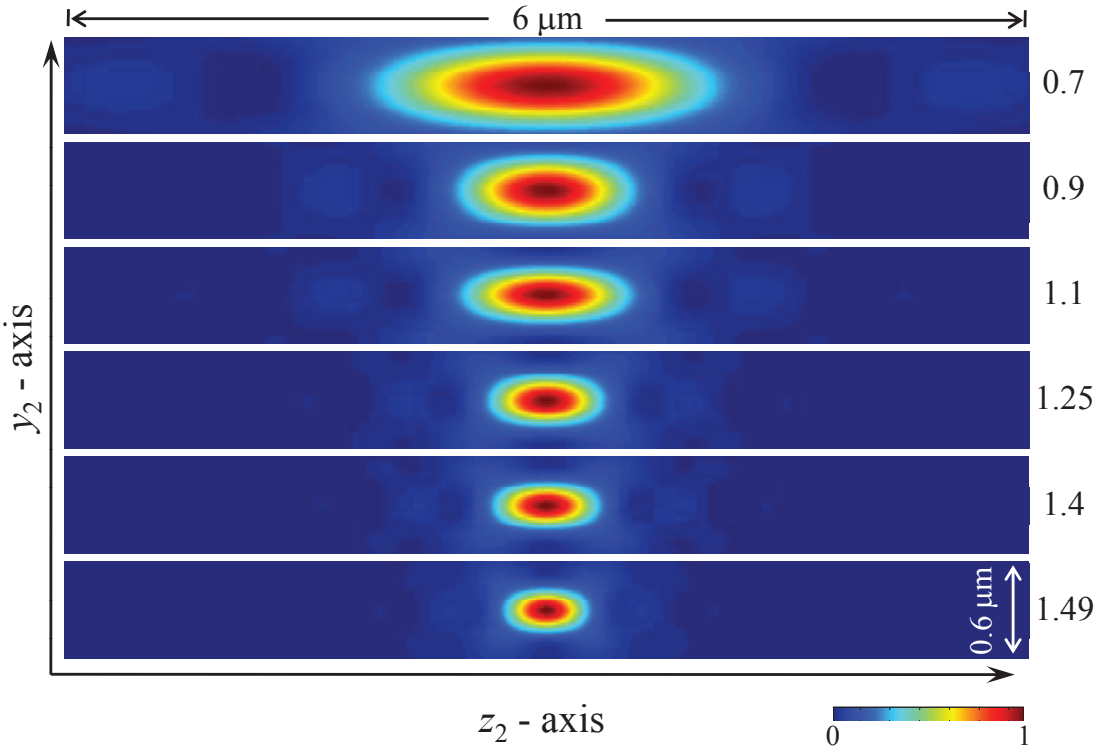

Figure 1.5: Longitudinal intensity distribution in the focusing region as a function of the numerical aperture (NA=0.7, 0.9, 1.1, 1.25, 1.4, 1.49). Results are obtained by using same parameters as those used in Figure 1.4.

Gaussian beams, respectively. The mathematics representations of the amplitudes of these beam modes can be described as shown in Table 1.2.

We note that for the Laguerre-Gaussian (L-G) beam mode, we only consider the first-order mode, *i.e.*, $p = 1$. In this case, $L_1^1(x) = 2 - x$, and the L-G beam has the shape of a double-ring. This mode however depends on the β-ratio, which is defined as the ratio of the pupil radius and the beam waist in front of the OL. In our calculation, we set $\beta = 2.0$ to ensure that the two rings of this beam profile pass through the OL pupil.

The cross sections of the incident laser beams profiles in front of lens aperture are shown in the first row of Figure 1.7. The relevant calculated field distributions in the focal region at $(x_2y_2)-$ and $(x_2z_2)-$planes are presented in Figure 1.7 (a_1-c_1) and (a_2-c_2), respectively. The numerical calculation results are obtained under a tight focusing condition (NA = 1.4, $n = 1.515$), and the incident beam possesses a right circular polarization. With different beam profiles the at entrance of the OL,

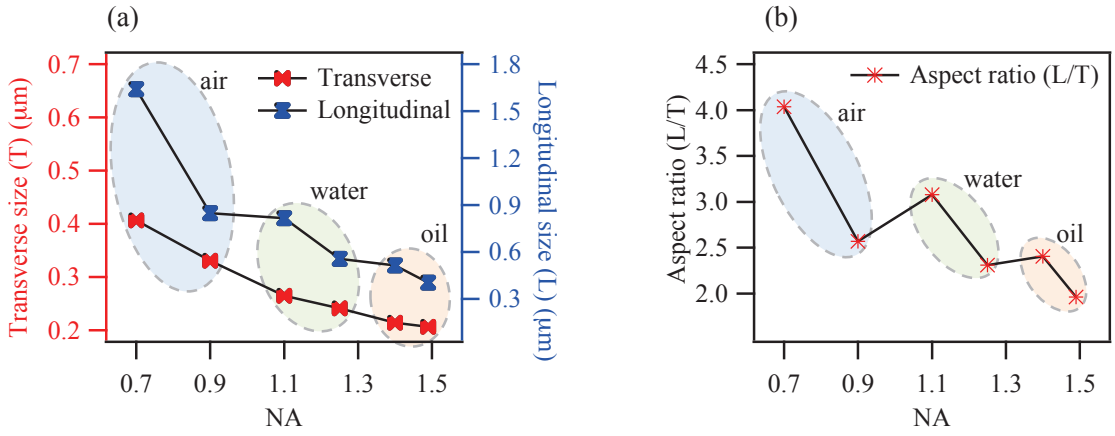

Figure 1.6: (a) FWHM size of the focal spot, along transverse and longitudinal directions. (b) Aspect ratio of the focusing spot as a function of the NA. Results are obtained by using same parameters as those obtained in Figures 1.4 and 1.5.

Uniform beam	$\mathrm{A}(\theta,\varphi) = 1$
Gaussian beam	$\mathrm{A}(\theta,\varphi) = \exp(-\frac{x_1^2+y_1^2}{w^2})$
Laguerre-Gaussian beam	$\mathrm{A}(\theta,\varphi) = \beta^2\frac{\sin\theta}{\sin^2\alpha}\exp[-(\beta\frac{\sin\theta}{\sin\alpha})^2]L_p^1[2(\beta\frac{\sin\theta}{\sin\alpha})^2]$

Table 1.2: Different beam modes used to calculate the intensity distribution in the focusing region of a high NA OL. $\mathrm{A}(\theta,\varphi)$ represents the amplitude of the beam mode. w is the waist of Gaussian beam. β is the ratio of pupil radius and beam waist. θ and φ are polar coordinates of lens aperture (see Figure 1.2). L_p^1 is the generalized Laguerre polynomial.

the intensity distributions in the focusing region are also different.

As compared to the uniform beam, Gaussian beam allows to obtain a very similar focusing spot but with a larger size. This can be explained by the fact that the light intensity of the Gaussian beam is concentrated in the beam center, which can be equivalent to the sum of a large aperture of the one of the uniform beam (high NA) and a small aperture of uniform beam (low NA). Hence, the resulted intensity distribution is larger than the one obtained with a single uniform beam (high NA). Because of a large transverse size, the aspect ratio of the focusing spot obtained by a Gaussian beam becomes smaller. With a proper beam waist of the Gaussian beam, it is possible to generate a focusing spot with a quasi-isotropic shape, which is a

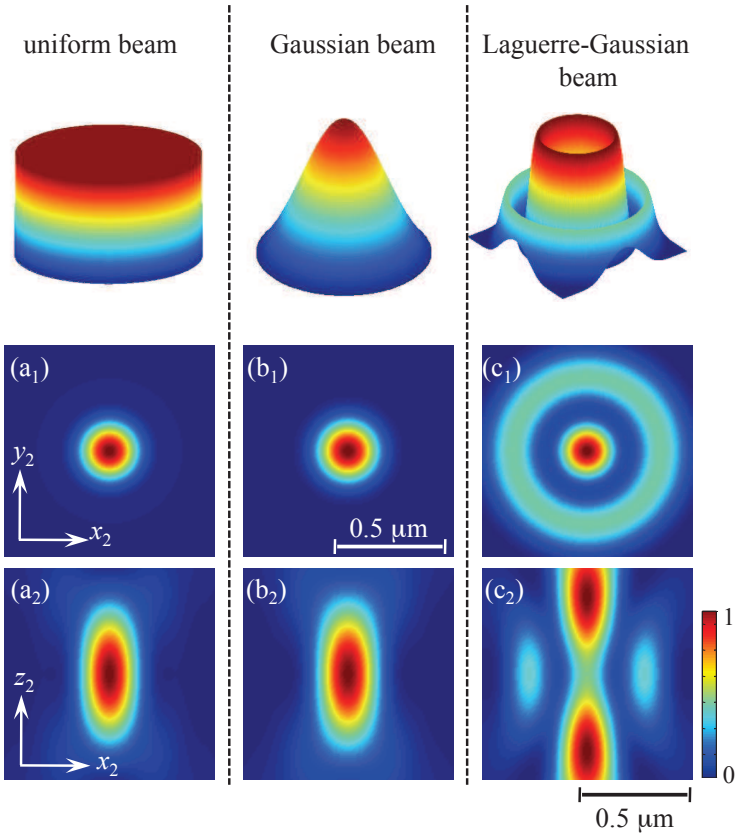

Figure 1.7: Comparison of the intensity distributions in the focusing region of a high NA OL, realized with different incident beam modes. Simulation parameters: $\lambda = 532$ nm, circularly polarized incident beam, NA $= 1.4$, $n = 1.515$.

high demand for many applications, such as 3D imaging and 3D fabrication. In the case of a L-G incident beam, the intensity distributions at $(x_2y_2)-$, $(x_2z_2)-$planes show that the shape of the focal spot is strongly modified. A significant portion of side ring along transverse direction is emerged. On $(x_2z_2)-$plane, the peak intensity has been splitted in two peaks along the optical axis (z_2-axis). This intensity distribution behavior can be explained by the fact that the focusing spot is the consequence of the interference of diffracted light rays in the focal region. In the case of L-G beam, the light of the inner and outer rings possess different phases, and thus when the diffracted rays are added up in the focal region, they interfere destructively and the total intensity at the focal point is weaken. In theory, with a fine control of the order of L-G and β, a focusing spot with zero intensity at focal point can be obtained, which is very interesting for super-resolution microscopy [15]

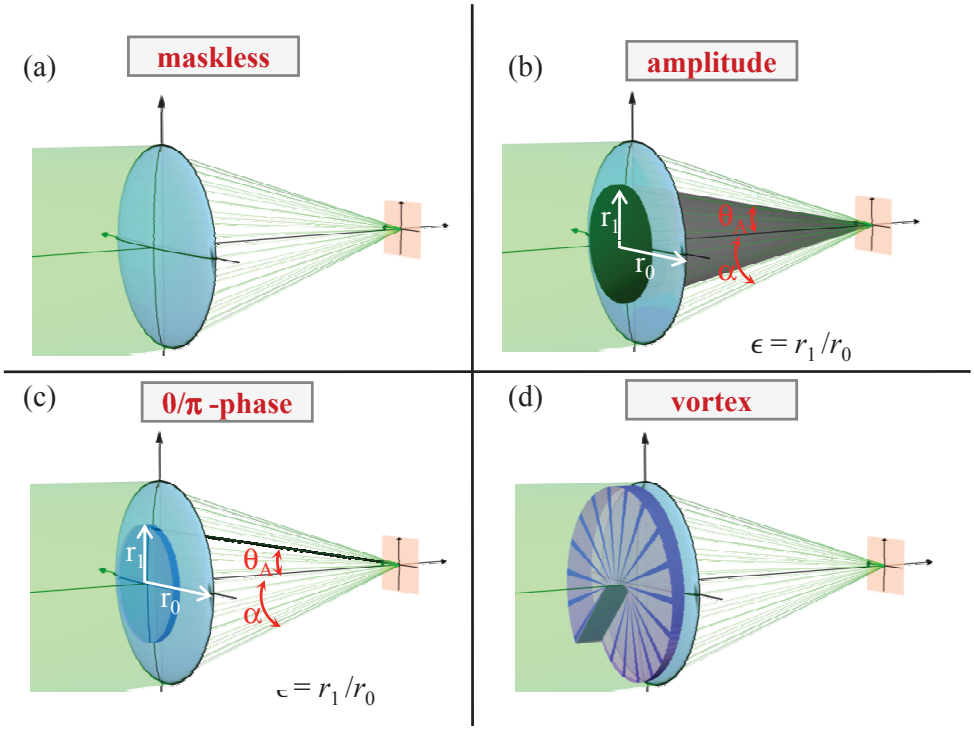

Figure 1.8: Modulation of the incident beam profile by different masks. (a) Maskless: uniform beam profile (reference beam); (b) Amplitude mask: to stop center part of light beam; (c) $0/\pi-$phase mask: introducing $\pi-$phase delay of center and outer parts of laser beam; (d) Vortex mask: phase of incident beam is rotationally shifted from 0 to 2π around the optical axis.

or optical trapping [29]. In practice, due to the fact that the intensity strength of two rings are not equal (first ring is dominant), the total intensity at focal plane is just weakened.

This study shows that the intensity distribution of focusing spot strongly depends on the profile of incident beam. For instance, the beam profile is varied by using different laser beam modes. In the next part, we will introduce alternative ways to modulate the incident beam profile and study their effects on the intensity distribution of tight focusing spot.

1.3.3 Effect of different masks on EM field distribution in the focal region

In this section, we present the influence of several masks, which are applied to modulate the incoming beam profile, on the size and form of a tight focusing spot. In this case, we assume that the incident beam displays an uniform beam profile, as already discussed in the last section. By using a proper mask, it is able to transform the uniform plane wave to a particular desired beam shape, such as hollow beam, phase singularity vortex beam, etc. Different optical masks investigated in this work are illustrated in Figure 1.8. In particular, we focus on three kinds of most frequently used masks, which shown an axial symmetry around the optical axis. Hence, it is convenient to define the diffracted wave vector using spherical coordinates (Eq. (1.5)). When using a mask (to modulate the uniform beam), the $\mathrm{A}(\theta, \varphi)$ is designed accordingly to the expected formation operated by the mask:

– *amplitude mask* (Figure 1.8(b))

$$\mathrm{A}(\theta,\varphi) = \begin{cases} 0 & : \text{blocked area } (\theta < \theta_{\mathrm{A}}), \\ 1 & : \text{unblocked area } (\theta_{\mathrm{A}} \leq \theta < \alpha), \end{cases} \tag{1.13}$$

where θ_{A} is the angle between the optical axis and the edge marginal line of the inner opaque area. As shown in Figure 1.8(b), $\sin\theta_{\mathrm{A}} = \varepsilon \sin\alpha$, where ε is the ratio between r_1 and r_0 ($\varepsilon = r_1/r_0$).

– *0/π phase plate* (Figure 1.8(c))

$$\mathrm{A}(\theta,\varphi) = \begin{cases} \exp(i\pi) & : \pi - \text{phase shift } (\theta < \theta_{\mathrm{A}}) \\ \exp(i0) & : 0 - \text{phase shift } (\theta_{\mathrm{A}} \leq \theta < \alpha), \end{cases} \tag{1.14}$$

where, θ_{A} is defined as the angle of blocked area in the case of amplitude mask.

–*vortex phase mask* (Figure 1.8(d))

$$\mathrm{A}(\theta,\varphi) = \exp(im\varphi) : 0 \rightarrow 2m\pi \text{ phase shift (axial rotation)}, \tag{1.15}$$

where m is an integer, which represents the order of the phase shift of a light beam around the symmetric optical axis.

We note that, in order to investigate the effect of masks on the intensity distribution in the focal region, we set a reference aperture (maskless), which is shown in Figure 1.8(a). Its intensity distribution has been shown in Figure 1.7($a_{1,2}$).

For all simulations of field distribution in the focal region, the parameters are: NA = 1.4, $n = 1.515$, $\lambda = 532$ nm, right circularly polarized incident beam. Under tight focusing, the numerical calculation results of the mask shows numerous crucial behaviors, as will be shown in detail in next subsections.

1.3.3.1 Amplitude mask

Figure 1.9 shows the calculated intensity distribution in the focal region of a high NA OL using an amplitude mask (Figure 1.8(b)). Compared to the maskless configuration, when $\varepsilon = 0.8$ for example, the transverse size (Figure 1.9(a)) of the focusing spot is decreased by about 15% while the longitudinal size is elongated along optical axis. Note that when introducing amplitude mask, there appears a side ring around the Airy disk. The intensity of this ring varies with ε. The EM field components along the x_2- and z_2-axes further indicate that the cause of the smaller transverse size is the shrink of radial components (E_{x_2} and E_{y_2}), and the creation of the ring is due to the longitudinal component E_{z_2} (Figure 1.9(e_1)). The elongated shape along the optical axis is the consequence of increased E_{x_2} (Figure 1.9(c_2)) and E_{y_2} (Figure 1.9(d_2)) components along optical axis. A focusing spot showing a smaller transverse size and longer longitudinal size is important for many applications, such as high resolution 2D microscope, optical tweezers, etc. The use of an amplitude mask to precisely control the focusing spot shape for different applications will be investigated again in Chapter 2.

1.3.3.2 $0/\pi-$phase plate

Instead of stopping the central part of an incident light beam, a $\pi-$phase retardation of this part with respect to the outer part, lead to strongly different results. Figure 1.10 shows the numerical results of a focusing spot using a $0/\pi-$phase plate (Figures 1.8(c)) in front of the entrance of objective aperture. As shown in Figure 1.10(a_1, a_2), at $(x_2y_2)-$plane, the initial Airy spot vanishes and a double-ring shape emerges, but with a relatively weak intensity. At $(x_2z_2)-$plane, it is clear that the field energy is splitted into two symmetric small focusing spots along the optical

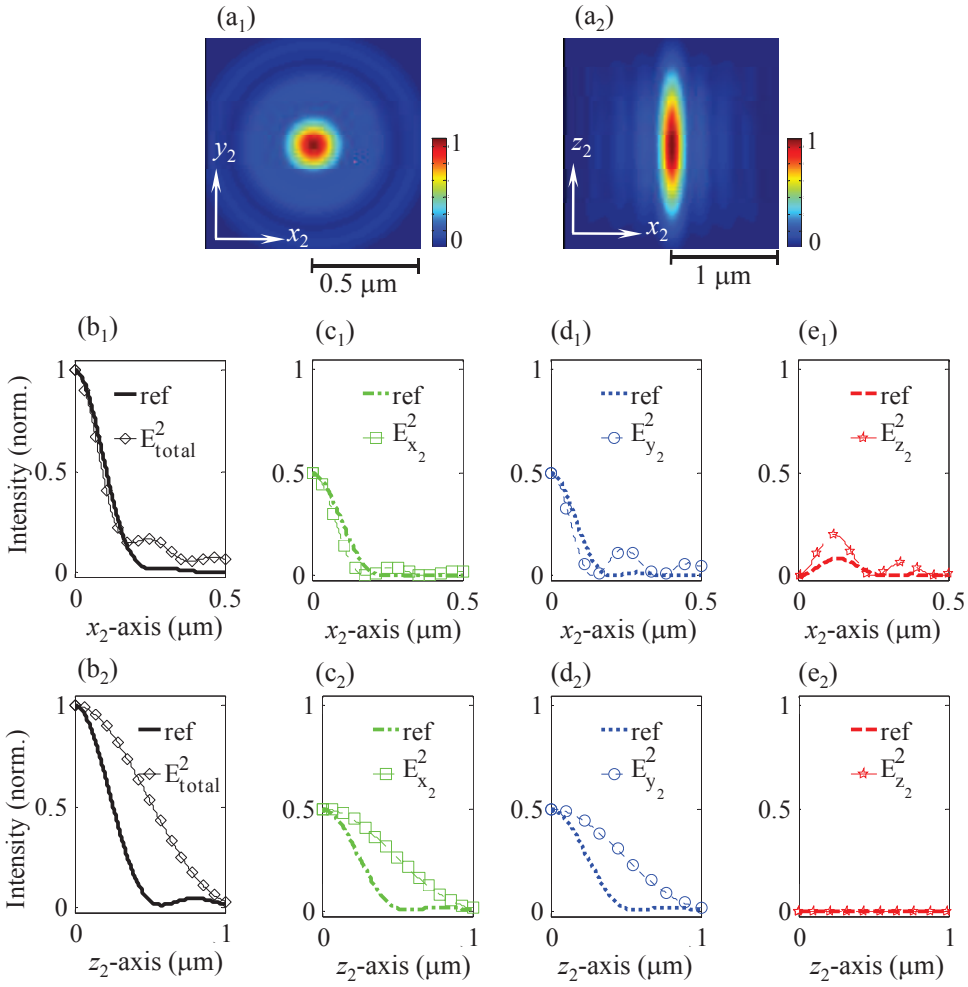

Figure 1.9: Influence of amplitude mask on the intensity distribution in the focal region. [a_1-e_1], [a_2-e_2] show the intensity distribution of total field, $E_{x_2}-$, $E_{y_2}-$, $E_{z_2}-$components along x_2-axis, y_2-axis, and z_2-axis, respectively. Reference beam (ref) is a circularly polarized uniform beam with wavelength, $\lambda = 532$ nm. The simulation parameters are: $\varepsilon = 0.8$, NA $= 1.4$, $n = 1.515$.

axis. The plotted intensity distribution of the different components show that, along the transversal direction (x_2-axis), all three components are eliminated. Along the longitudinal direction (z_2-axis), the peak intensity is shifted to its original first minimal position, which is mainly caused by the shift of radial components (E_{x_2} and E_{y_2}) to the two sides of the focal point as shown in Figure 1.10(c_2, d_2). This behavior can be also explained by the fact that due to the $\pi-$phase shift of the inner part of the incident beam, when the rays are adding up at the focal region, the phase difference of rays induces destructive interference at the focal point, while at

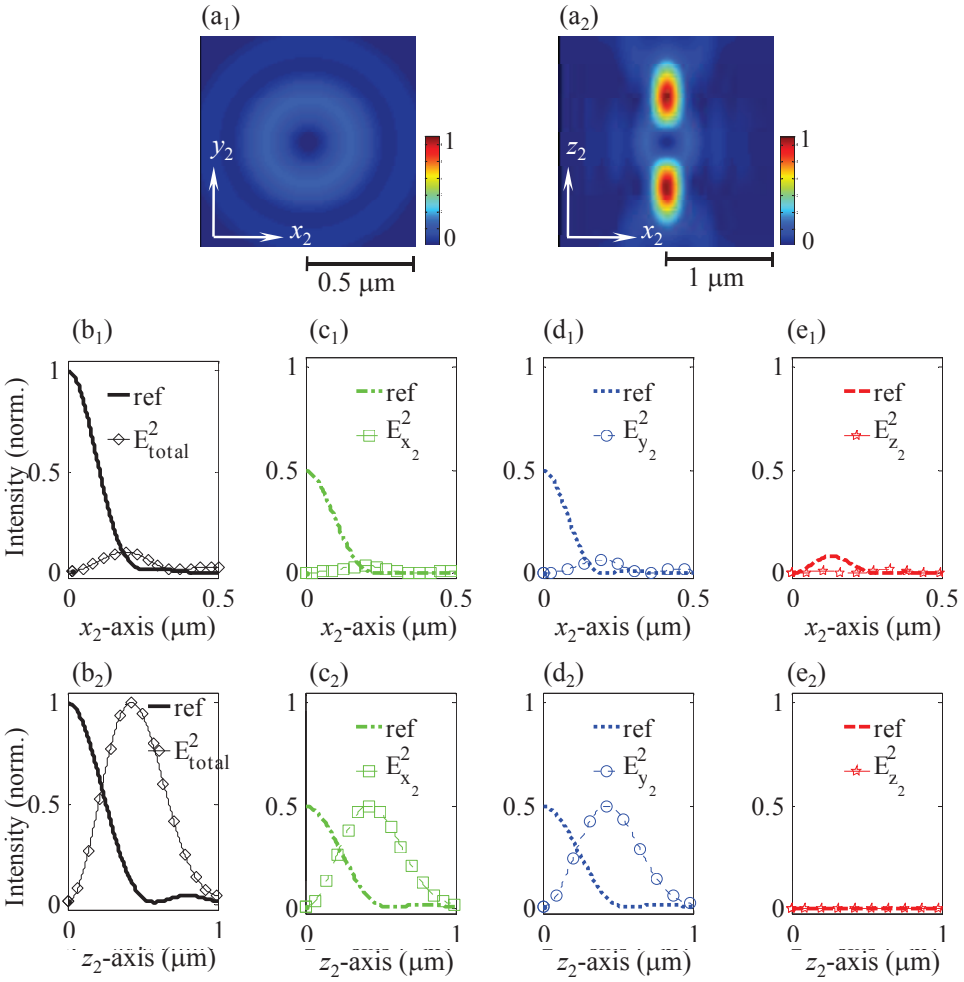

Figure 1.10: Influence of $0/\pi-$phase mask on the intensity distribution in the focal region. The simulation parameters are: $\varepsilon = 0.75$, NA $= 1.4$; $n = 1.515$.

its vicinity, rays are in phase and thus a constructive field distribution appears. The focusing spot created by the $0/\pi-$phase plate plays a key role for 3D imaging [30] and 3D fabrication [31] applications, as will be explained in chapter 3.

1.3.3.3 Vortex mask

The amplitude mask and $0/\pi-$phase mask modulate either the amplitude or the phase between the central and outer parts of the incident beam. The modulation from a vortex mask, which changes the phase of the incident beam around the optical axis, is also very interesting to analyse.

In our calculation, we set $m = 1$ (Eq. (1.15)) to impose a phase change of the

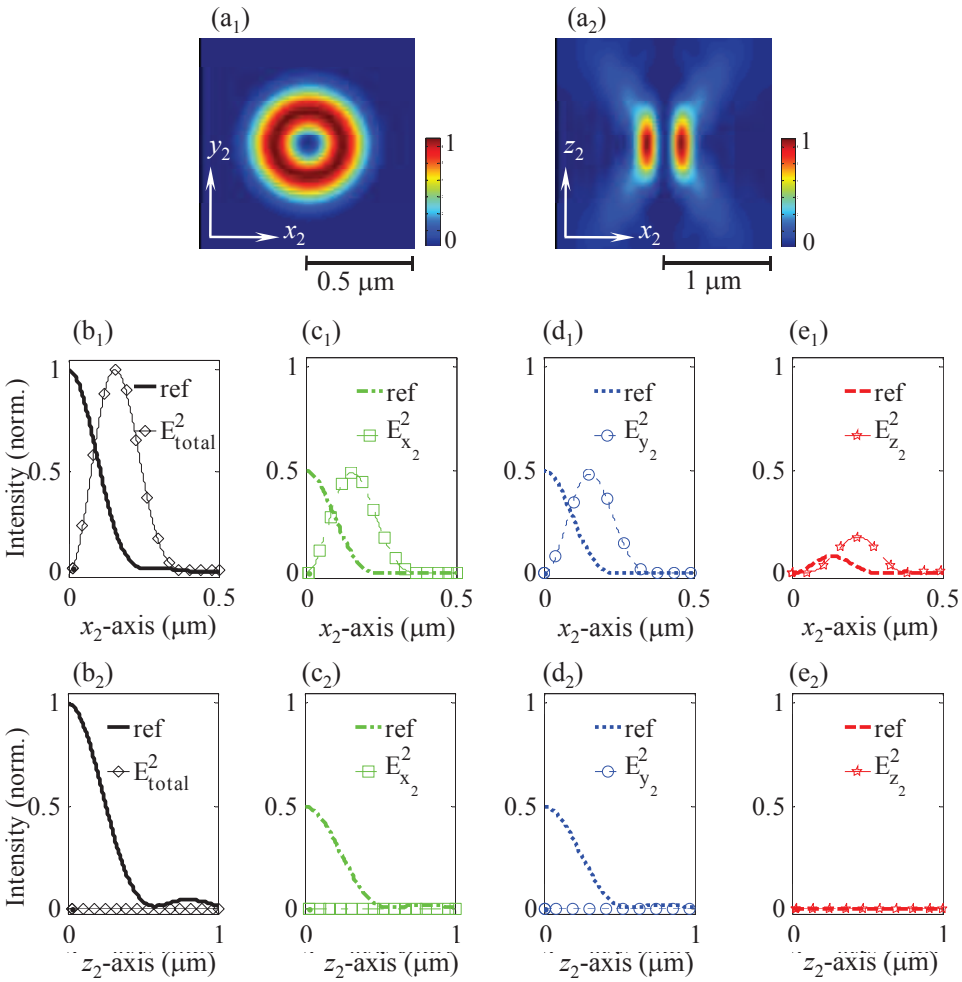

Figure 1.11: Influence of vortex mask on the intensity distribution of focusing spot. Simulation are realized with the same parameters as in Figure 1.9.

incident beam from 0 to 2π around the optical axis. 0 is assumed to be the phase of the light rays located at the positive part of the $x-$axis of the OL. In this case, there is a phase singularity in the center of the phase-modulated beam. However, in the numerical calculation, it does not affect the results, since the diffracted ray from this single point shows a negligible contribution to the focusing spot, as compared to those from the whole aperture. In Figure 1.11, the calculated intensity distribution shows that, at $(x_2y_2)-$plane, a doughnut shaped distribution appears instead of an Airy disk. At $(x_2z_2)-$plane, the intensity is vanished all along the optical axis. This intensity distribution is a strong evidence of the vector properties of light. Indeed, the plotted different field components along the x_2-axis (Figure 1.11(b_1-e_1))

show that the creation of a doughnut shape in the focal region mainly results from the change of the radial components (E_{x_2} and E_{y_2}) from an Airy to a doughnut distribution. The longitudinal component (E_{z_2}), which has an initial doughnut profile, is shifted far away from the optical axis. The intensity of the z_2-component displays a little increase (less than 20% of total intensity). The three components along the z_2-axis (Figure 1.11(b_2-c_2)) show that, in all cases, there are no intensity distribution along optical axis, resulting in a focal spot with a hollow shape.

The 2D doughnut focusing spot is very important for many applications. For instance, in a STED microscopy, the doughnut focal spot is introduced to deplete unwanted spontaneous emission. In super-resolution optical lithography, the doughnut spot is also used to inhibit the photoresist from polymerization.

The three presented masks, amplitude, $0/\pi$ and vortex phase plates allow to symmetrically modulate the beam intensity profile or phase distribution around the optical axis. It is interesting then to investigate the intensity distribution of the focusing spot when the incident light beam has an arbitrary amplitude or phase distribution.

1.3.3.4 Focusing a laser beam with an arbitrary wavefront or intensity profile

In order to work with a laser beam, showing an asymmetric intensity or phase distribution, we employed the Cartesian coordinates. The geometry of the mask used to modulate the incident beam profile is shown in Figure 1.12(a). This amplitude mask has a double-hole shape allowing to modulate the incident beam to perform an isotropic focusing spot in the focal region. As shown in Figure 1.12(b), due to this particular amplitude mask, only certain parts of the incident beam, corresponding to the two open areas Σ_1 and Σ_2, are able to propagate through an objective aperture and towards to the focal region.

The calculated intensity distributions at $(x_2 z_2)-$plane of this particular incident beam are shown in Figure 1.13. For this numerical calculation, the radii of the two open areas are $r_1 = r_2 = 2.1$ mm; the center of the two circles (O_{1a}, O_{1b}) are located at a distance d = 2.9 mm from the optical axis. The radius of the full aperture size is $r_0 = 5$ mm; the employed OL has NA = 1.4, $n = 1.515$; the wavelength of input beam is $\lambda = 532$ nm. Due to these small off-axis open areas Σ_1, Σ_2, the light from each area results in a "tilted" focusing spot in the focal region (Figure 1.13(a,b)).

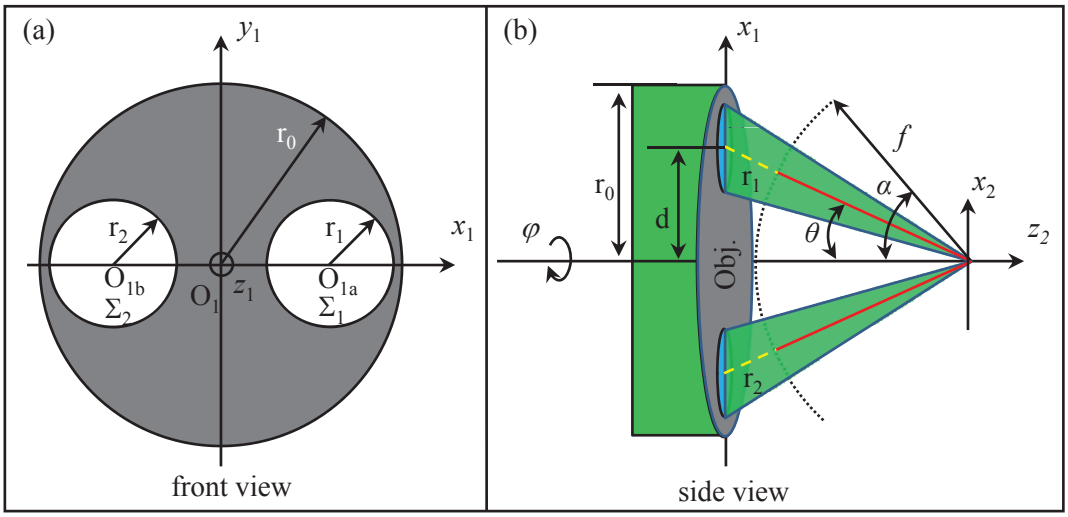

Figure 1.12: Focusing the light via a double-hole mask. (a) front view. (b) side view. r_1, r_2 are the radii of the opened areas Σ_1, Σ_2, respectively. The center of these two areas, O_{1a}, O_{2b}, are located at a distance d from the optical axis of objective aperture.

Thus, if there is no correlation between the two PSFs, when adding up their respect contributions in the focal region, a 3D isotropic PSF is obtained (Figure 1.13(c)). The FWHM size of this PSF is about 1 μm for both x_2- and z_2- axis. The size of this 3D PSF is relatively large, because light propagates through small areas, which is equivalent to the case of a light beam focused by a small NA OL.

According to the vectorial properties of light, the focusing spot size can be further reduced. In the next part, we will present the influence of the incident beam polarization on the intensity distribution of a tight focusing spot.

1.3.4 Influence of polarization of the incident light on the intensity distribution of a tight focusing spot

In the previous sections, we studied the effects of the beam modes of incoming light and input masks on the intensity distribution in the focal region. In this section, we investigate the influence of different types of polarization, which are

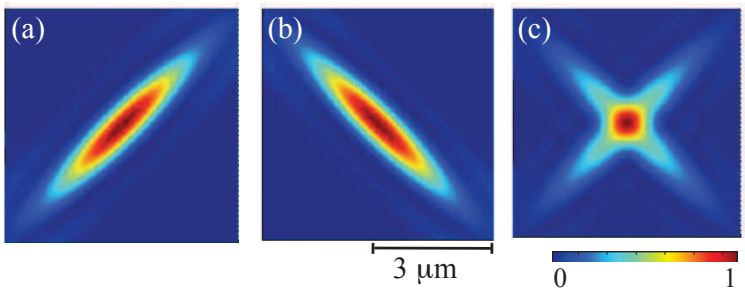

Figure 1.13: Calculated intensity distribution of a tightly focused beam in the focal region. Focusing spot obtained by light beam corresponding to the area Σ_1 (a), area Σ_2 (b) and both areas (c), respectively. $r_1 = r_2 = 2.1$ mm, $d = 2.9$ mm, $r_0 = 5$ mm. $\lambda = 532$ nm, NA $= 1.4$, $n = 1.515$.

shown schematically in Figure 1.14 (left side of each subfigure), on the intensity distribution of the focusing spot. The polarization strength of radial (p_x, p_y) and longitudinal (p_z) components, are presented in the Table 1.3 [24]. In all cases, the laser beam is assumed to propagate in the direction of the optical axis. Hence, p_z is set as zero to indicate that the incident beam is transversely polarized before entering OL aperture.

Polarization	x-linear	y-linear	RC	LC	elliptical	radial	azimuthal
p_x	1	0	$\frac{1}{\sqrt{2}}$	$\frac{i}{\sqrt{2}}$	$\frac{2}{\sqrt{5}}$	$\cos\varphi$	-sin φ
p_y	0	1	$\frac{i}{\sqrt{2}}$	$\frac{1}{\sqrt{2}}$	$\frac{i}{\sqrt{5}}$	$\sin\varphi$	$\cos\varphi$
p_z	0	0	0	0	0	0	0

Table 1.3: Different polarization states of the incident light beam that are used to study the intensity distribution of the focusing spot of a high NA OL. RC: right circular polarization. LC: left circular polarization.

The polarizations of the laser beam before and after lens aperture are illustrated in Figure 1.14 (right side of each subfigure). The related mathematics representation of the polarization conversion, T (θ, φ) (Eq. (1.9)), has been presented earlier in Section 1.2.

As shown in Figure 1.14, when a light beam propagates through an objective aperture, its polarization states are modulated. If the NA of the OL is relatively high, the effect of the polarization of incident beam on the intensity distribution of

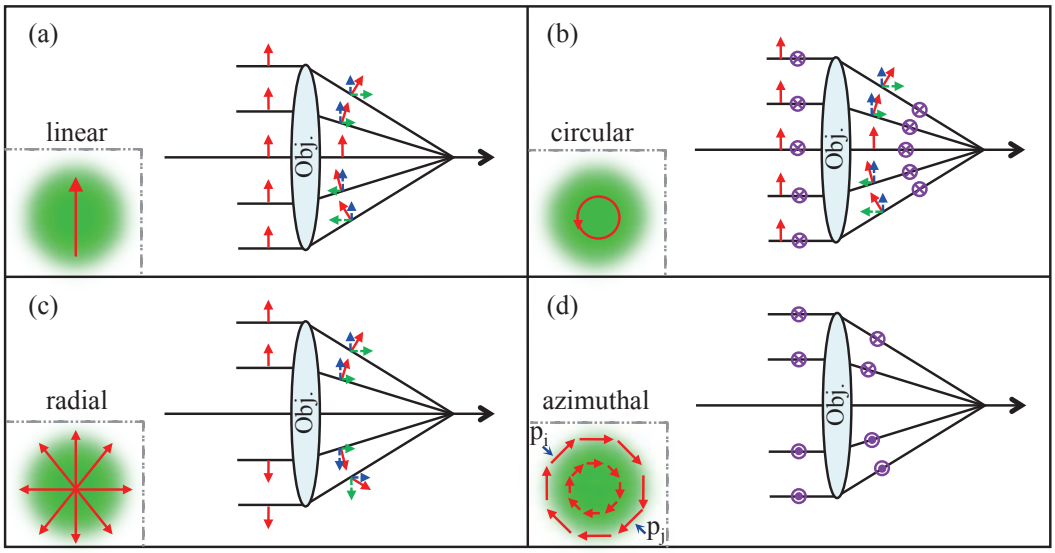

Figure 1.14: Illustration of polarization conversion in a tight focusing system. The left part of each sub graph is the schematic representation of the polarization of the incident beam: linear (a), circular (b), radial (c), azimuthal (d). The right part of each sub graph shows the polarizations before and after the OL. The signs $\otimes$ and $\odot$ indicate the polarizations of the EM field, pointing in and out of plane, respectively.

the focusing spots is significant [19]. Here, we use a high NA OL (NA = 1.4, n = 1.515) to investigate the influence of the incident beam polarization on the intensity distribution of a tight focusing spot.

1.3.4.1 Focusing spot of a $x-$linearly polarized incident beam

In the case of a $x-$linearly polarized incident beam, as shown in Figure 1.15(a), the total intensity distribution of the focusing spot at $(x_2y_2)-$plane shows an elongated shape along the incident light polarization direction. The different $E^2_{x_2}$, $E^2_{y_2}$ and $E^2_{z_2}$ components, which are normalized to the total intensity E^2_{total}, are shown in Figures 1.15 (b_1-d_1). It is clear that, because the incident beam is $x-$linearly polarized, the $E^2_{x_2}-$component, which has a symmetric shape, plays a dominant role in the focal region. However, as shown in Figure 1.15(d_1), it is interesting to note that, under tight focusing conditions, the input light beam induces a longitudinal component (E_{z_2}) at focal region of the OL. The reason is that, when the $x-$linearly polarized beam passes through the OL aperture, as illustrated in Figure 1.14(a), light rays significantly converge, and their polarization rotates accordingly. Thus,

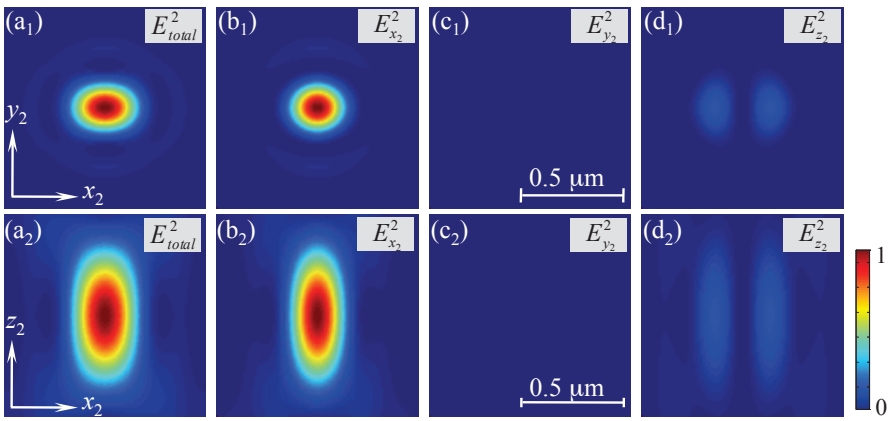

Figure 1.15: EM field distribution of $x-$linearly polarized incident beam in the focal region. [(a) - (d)] show the intensity distribution of total field, longitudinal component E_{z_2}, and two radial components, E_{x_2} and E_{y_2}, respectively. Subscripts 1, 2 indicate the intensity distribution at $(x_2y_2)-$ and $(x_2z_2)-$planes. $\lambda = 532$ nm, NA $= 1.4$, $n = 1.515$.

there are x_2-component (blue arrow) and z_2-component (green arrow) in the focusing region. The x_2-component keeps a same phase, and thus the induced intensity distribution ($E^2_{x_2}$) shows a constructive pattern at the focal point. In contrast, for the emerging z_2-component, the rays from the upper part of the $x-$axis (positive direction) have a direction opposite ($\pi-$phase difference) to that respect to those from the lower part of the $x-$axis (negative direction). Hence, when diffracted rays add up in the focal region, destructive interference occurs at the optical axis and constructive interference occurs at its vicinity (Figure 1.15(d$_1$)). Due to the significant contribution of this longitudinal component, the focusing spot displays an asymmetric shape in the focal region. When increasing of NA, this asymmetric shape becomes more significant.

The intensity distribution profile of different components along the x_2-, y_2-, z_2-axes are shown in Figure 1.16. The longitudinal component $E^2_{z_2}$ represents about 14% of total intensity while the $E^2_{y_2}$ contributes to less than 0.5% of total intensity.

Because of the asymmetrical focusing spot, the FWHM of the total intensity along y_2-axis (black line in Figure 1.16(b)) is about 182 nm while the one along the x_2-axis (black line in Figure 1.16(a)) is about 254 nm. Note that, in the case of a $y-$linearly polarized incident beam, the focusing spot has the same elongated shape as that obtained by a $x-$linear polarization, but the long axis of the focusing spot

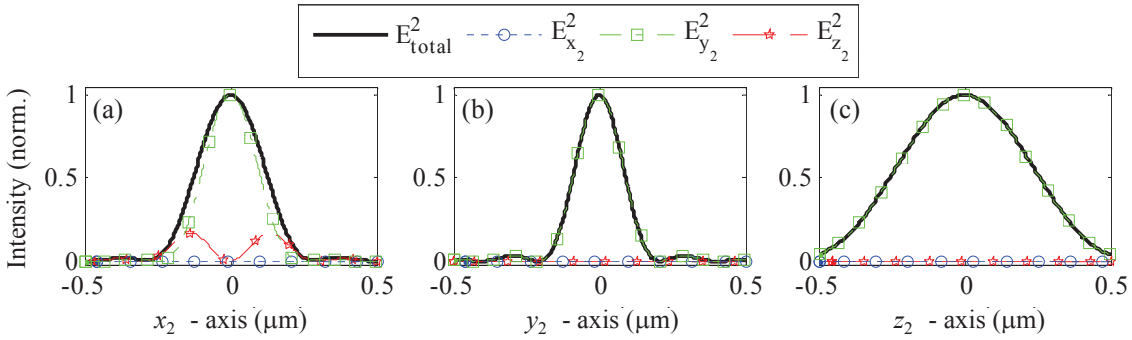

Figure 1.16: Intensity distribution of $x-$linearly polarized incident beam in the focal region. (a) - (c): EM field distribution along x_2-, y_2-, z_2-axes, respectively. Numerical calculation parameters are same as those in Figure 1.15.

is parallel to the y_2-axis. In practice, for a high resolution imaging or fabrication, the asymmetric distribution caused from linearly polarized incident beam is a drawback. In contrast, the small focusing spot of the E_{x_2} component could be useful for some applications, such as single molecule excitation or surface plasmonic polariton excitation. In practice, since the focusing spot size is in the sub-micrometer scale, it is quite challenging for experimental characterization of this asymmetric behavior. The experimental measurement of the asymmetric focusing spot will be presented in detail in chapter 4.

1.3.4.2 Focusing spot of a circularly polarized incident beam

As discussed earlier, the asymmetric focusing spot often induces unwanted issues. In practice, a circularly polarized beam is usually used for tight focusing because it induces a perfectly symmetric focusing spot, as shown in Figure 1.17(a). In fact, there is an equivalent distribution of the two radial components $E_{x_2}^2$ (Figure 1.17(b)) and $E_{y_2}^2$ (Figure 1.17(c)). Hence, when these components add up in the focal region, it produces a symmetric focusing spot.

The field distribution of different components along the x_2-, y_2- and z_2-axis in the focal plane are shown in Figure 1.18. It is clear that the intensity of E_{x_2} and E_{y_2} are the same and each of them contributes 46% of total intensity. E_{z_2} has the same profile along both directions (Figure 1.18(a,b)), but its intensity is only 8% of the total intensity. However, this longitudinal component possesses a doughnut shape as shown in Figures 1.17(d_1). In the focal region, the doughnut shape often tends to enlarge the spot size. Comparing to the focal spot obtained by a linearly

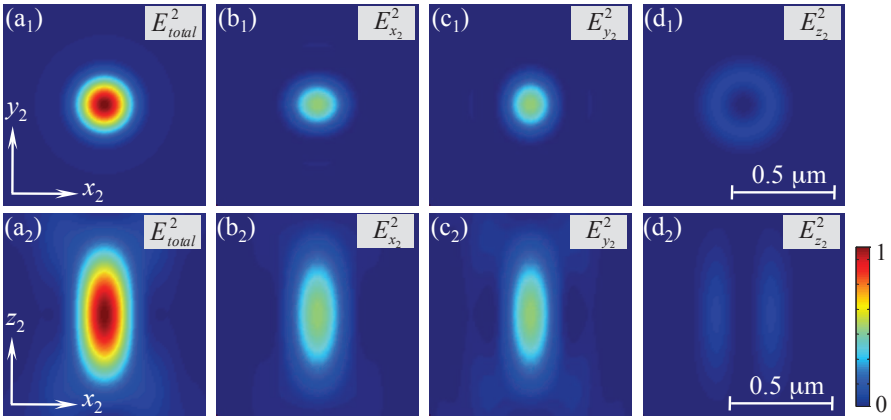

Figure 1.17: EM field distribution of circularly polarized incident beam in the focal region. [(a) - (d)] show the intensity distribution of total field, longitudinal component E_{z_2}, and two radial components, E_{x_2}, E_{y_2}, respectively. Subscripts 1, 2 indicate the intensity distribution at $(x_2y_2)-$, $(x_2z_2)-$planes, respectively. Results are obtained with $\lambda = 532$ nm, NA $= 1.4$, $n = 1.515$.

polarized beam, the size of the focusing spot in this case (210 nm) is smaller than that along the elongated direction (254 nm), but larger than the size along its short axis (182 nm). Since the left circularly polarized beam also possesses a symmetric focal spot in the focal region which is the same as for the right circularly polarization, we do not show these numerical results. Also, in the case of an elliptically polarized incident beam, depending on the polarization strength of p_x and p_y, the shape of focusing spot continuously varies in between the shapes of the linear and circular polarization cases.

In practice, in order to obtain a circularly polarized beam, a quarter-wave plate is introduced to convert an incident beam polarization state from linear to either right or left circular cases. Recently, by using devices based on liquid crystal arrays, such as spatial light modulator and polarization converter, the polarization of laser beam can be modulated at will. In the next section, we will present the focusing behavior of the incident beam with a highly modulated polarization distribution.

1.3.4.3 Focusing spot of a radially polarized incident beam

As depicted in the left side of Figure 1.14(c), the radial polarization is the combination of different linear polarizations whose orientations are axially distributed along optical axis. The intensity distribution of the focusing spot induced from a radially

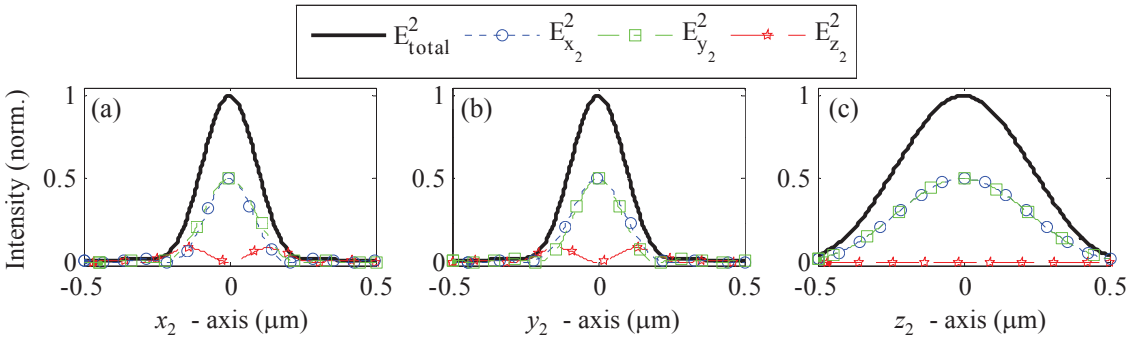

Figure 1.18: Intensity distribution in the focusing region obtained by circularly polarized incident beam. (a) - (c): EM field distribution along x_2-, y_2-, z_2-axes, respectively. Numerical calculation parameters are taken same as those in Figure 1.17.

polarized incident beam is shown in Figure 1.19. At $(x_2y_2)-$plane, the total intensity distribution (a_1) has a symmetric shape, but as compared to the case of circular polarization, the focusing spot is larger. It is due to fact that, as shown schematically in the Figure 1.14(c) (right side), the emerged radial components of the light rays (blue arrow) located at the upper part of the optical axis have opposite directions ($\pi-$phase difference) to those located at the lower part of optical axis. Thus, when light rays add up in the focal region, due to the destructive interference at focal region, the radial components (E_{x_2}, E_{y_2}) show a double-spot shape. In contrast to the radial component, due to the same direction (in phase) of the emerged longitudinal component (green arrow) at the exit of OL aperture, the intensity distribution of longitudinal component has constructive shape in the focal region.

The intensity distributions of the different components of the focusing spot along the x_2-, y_2- and z_2-axes are shown in Figure 1.20. It shows clearly that the larger profile of total intensity distribution (240 nm) is caused from significant portion (30%) of the radial components (E_{x_2}, E_{y_2}), which have a double-spot shape in the focal region. The FWHM size of the longitudinal component along lateral direction is only 170 nm, which is much smaller than the diffraction-limited size. Hence, suppressing the radial components, meanwhile enhancing the longitudinal component, is one way to obtain a sub-diffraction limited focusing spot. This will be discussed in detail in Chapter 2.

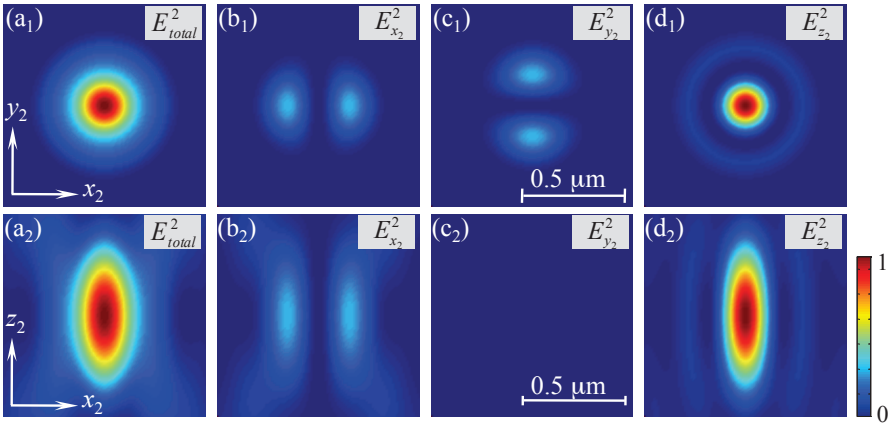

Figure 1.19: EM field distribution of radially polarized incident beam in the focal region. [(a) - (d)] show the intensity distribution of total field, longitudinal component E_{z_2}, and two radial components, E_{x_2} and E_{y_2}, respectively. Subscripts 1, 2 indicate the intensity distribution at $(x_2y_2)-$ and $(x_2z_2)-$planes. $\lambda = 532$ nm, NA $= 1.4$, $n = 1.515$.

1.3.4.4 Focusing spot of an azimuthally polarized incident beam

The azimuthal polarization is illustrated in Figure 1.14(d) (left side). It consists of numerous linearly polarized segments whose orientations are axially symmetric around the optical axis. The intensity distribution of the focusing spot of an azimuthally polarized incident beam is shown in Figure 1.21. Unlike the cases of linearly, circularly and radially polarized incident beams, the use of a laser beam with azimuthal polarization allows to obtain a transversal dark hole in the focal region (Figure 1.21(a_1)). It is due to the fact that the orientation of the local polarization is orthogonal to the axial direction of the incident beam and the optical axis of OL, when it passes through the OL aperture, no longitudinal component can emerge (Figure 1.14(d)). Hence, there is no contribution from the longitudinal component to the field distribution in the focal region (Figure 1.21($d_{1,2}$)). Moreover, in the case of an azimuthal polarization, there always exists a pair of rays, having $\pi-$phase difference, symmetrically located around the optical axis (*i.e.*, p_i and p_j, see Figure 1.14(d)). Thus when these rays are interfering in the focal region, a destructive interference is obtained (Figure 1.21(b_1, c_1)).

The intensity distributions of different components along the x_2-, y_2- and z_2-axes in the focal region are shown in Figure 1.22. The longitudinal component (red dash line) is zero for all three axes. The field distributions in the focal

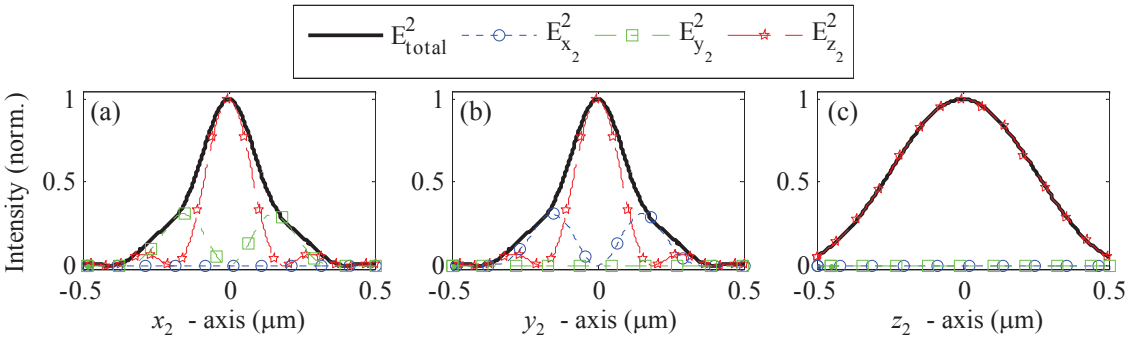

Figure 1.20: Intensity distribution of in the focal region obtained by a radially polarized incident beam. (a) - (c): EM field distribution along x_2-, y_2-, z_2-axes, respectively. Numerical calculation parameters are taken same as those in Figure 1.19.

region are purely transversely polarized. The FWHM size of the dark area of the doughnut spot is about 142 nm, which is smaller than the diffraction limit. This small transversal doughnut focusing spot has many important applications, such as 2D STED microscopy and saturated absorption microscopy, etc.

In principle, for each application, the optical mask, and the incident beam polarization can be well defined to perform a desired field in the focal region. However, in practice, the focusing quality is also affected by other factors. The degradation of the focusing quality caused by the refractive index mismatch introduced by an interface is one of the most often faced problems. In the next section, we will present the intensity distribution of the focusing spot in the presence of a dielectric interface.

1.3.5 Focal shift of a tightly focused beam in the presence of a refractive index mismatch

In practice, one critical problem concerning optical microscopy application is aberration, which degrades the capability of optical microscope. In this section, we will discuss about one of the most important effects caused by the refractive index mismatch media: spherical aberration.

As illustrated in Figure 1.23, in a tight focusing system, when light is focused through a dielectric interface D, due to refraction, it does not reach the geometrical focal point O_0. Depending on the values of $n_1$and n_2, the focusing spot appears either at the left (O_1) or right side (O_2) of its original focal point (O_0). Joel *et*

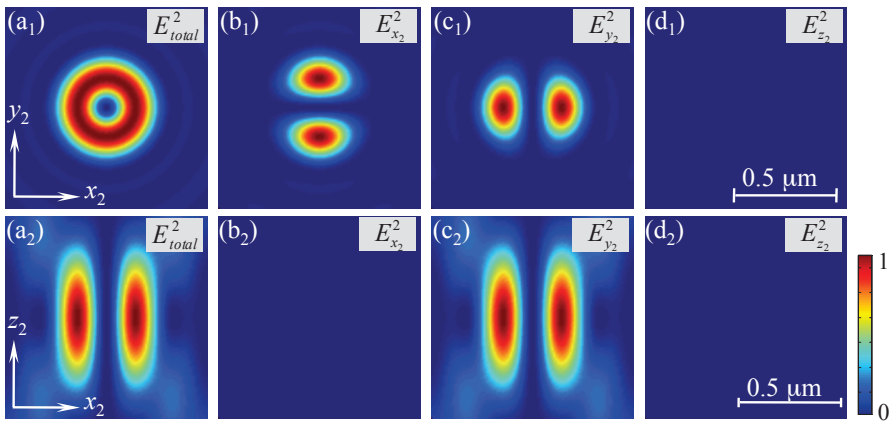

Figure 1.21: EM field distribution of azimuthally polarized incident beam in the focal region. [(a) - (d)] show the intensity distribution of total field, longitudinal component E_{z_2}, and two radial components, E_{x_2} and E_{y_2}, respectively. Subscripts 1, 2 indicate the intensity distribution at $(x_2y_2)-$ and $(x_2z_2)-$planes. $\lambda = 532$ nm, NA $= 1.4$, $n = 1.515$.

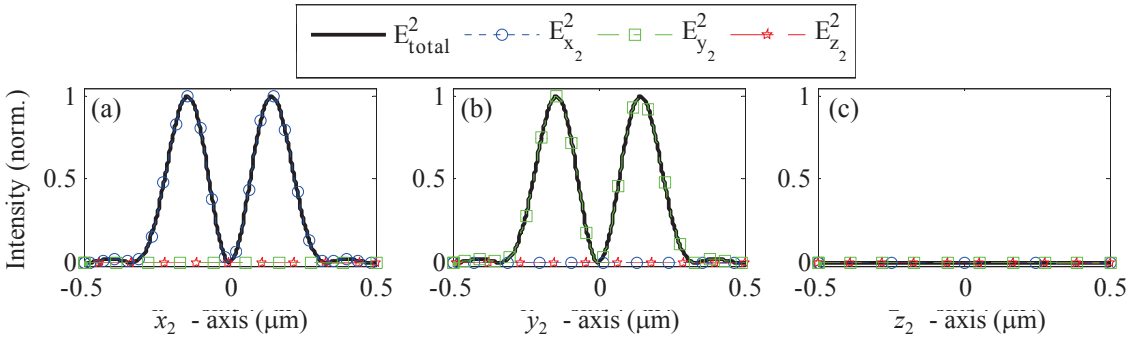

Figure 1.22: Intensity distribution of in the focusing region obtained by an azimuthally polarized incident beam in the focal region. (a) - (c): EM field distribution along x_2-, y_2- and z_2-axis, respectively. Numerical calculation parameters are taken same as those in Figure 1.21.

al. [32] reported that, according to quantitative measurement of this shift, a lens system can be used to measure the refractive index of material. However, their study mainly focused on the case of a low NA OL, in which the vectorial properties of light is neglected. In the case of a high NA focusing system, light rays significantly converge and the transmission (Fresnel coefficient) of s- p- polarizations have to be considered.

As compared to the EM field distribution in a homogeneous medium, the additional points must be further considered: the first one is the nonequivalent trans-

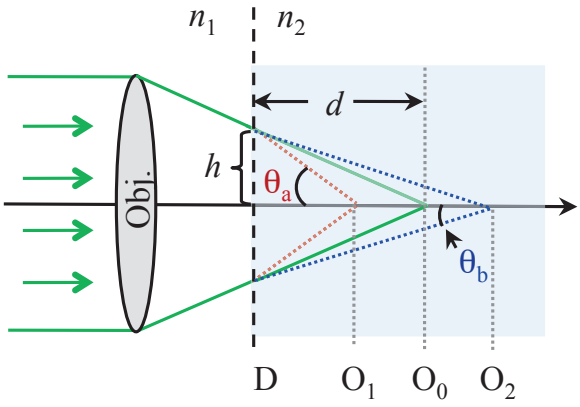

Figure 1.23: Schematic illustration of the propagation of a tightly focused beam in the presence of refractive index mismatch. n_1, n_2 are the refractive indices of first and second media, respectively. O_0 is the focal point in the case of homogeneous medium ($n_1 = n_2$), and O_1, O_2 are the shifted focal points induced by refractive index mismatched cases. D is the interface between two media. d is the distance between D and O_0.

mission of different field components, and the other is phase aberration ($\Phi(\theta, \varphi)$). Therefore, we should rewrite the polarization conversion equation (Eq. (1.9)) which has been discussed in Section 1.1. In the first medium, n_1:

$$\mathrm{P}_1(\theta_1, \varphi) = \mathrm{T}_1(\theta_1, \varphi)\mathrm{P}_0 = R^{-1}CR\mathrm{P}_0, \tag{1.16}$$

where P_1 represents the polarization distribution in medium 1, P_0 is the incident beam polarization, R and C describe the rotation of the coordinate system around the optical axis (see Eq (1.10) in Chapter 1). The polarization distribution in the second medium is then given by [33–35]:

$$\mathrm{P}_2(\theta_1, \theta_2, \varphi) = \mathrm{T}_2(\theta_1, \theta_2, \varphi)\mathrm{P}_1(\theta, \varphi) = \mathrm{T}_2(\theta_1, \theta_2, \varphi)\mathrm{T}_1(\theta_1, \varphi)\mathrm{P}_0, \tag{1.17}$$

where :

$$\mathrm{T}_2(\theta_1, \theta_2, \varphi) = [L^{(2)}]^{-1} I L^{(1)}, \tag{1.18}$$

and:

$$I = \begin{bmatrix} t_p & 0 & 0 \\ 0 & t_s & 0 \\ 0 & 0 & t_p \end{bmatrix}, L^{(i)} = \begin{bmatrix} \cos\theta_i & 0 & -\sin\theta_i \\ 0 & 1 & 0 \\ \sin\theta_i & 0 & \cos\theta_i \end{bmatrix}, \tag{1.19}$$

which describes the rotation of the coordinate system into s- and p-polarized vectors, $i = 1, 2$ represent the light rays before and after the interface D, I represents the transmission of the dielectric interface and t_s and t_p are the Fresnel coefficients:

$$t_s = \frac{2\sin\theta_2\cos\theta_1}{\sin(\theta_1+\theta_2)}, \quad t_p = \frac{2\sin\theta_2\cos\theta_1}{\sin(\theta_1+\theta_2)\cos(\theta_1-\theta_2)}, \tag{1.20}$$

θ_1 ($i = 1$) and θ_2 ($i = 2$) are the propagation angles of diffracted ray in medium 1 and medium 2, respectively. According to Snell's law, $n_1\sin\theta_1 = n_2\sin\theta_2$.

Besides, due to the presence of the dielectric interface, the induced aberration factor is given as [34] :

$$\Phi(\theta_1, \theta_2, d) = -d(n_1\cos\theta_1 - n_2\cos\theta_2), \tag{1.21}$$

where d is the distance between the dielectric interface D and the focal point O_0 (Figure 1.23).

Using $\Phi(\theta_1, \theta_2, d)$ and $P_2(\theta_1, \theta_2, \varphi)$, Eq. (1.7), is rewriten as [34]:

$$\begin{aligned} \mathbf{E}(x_2, y_2, z_2) = -\frac{i\mathrm{C}}{\lambda}\int_0^{\alpha}\int_0^{2\pi} \sin\theta_1 \mathrm{A}(\theta_1,\varphi)\mathrm{B}(\theta_1,\varphi)\mathbf{P}_2(\theta_1,\varphi) \\ \times \exp[ik_0(n_2 z_2\cos\theta_2 + n_1 x_2\sin\theta_1\cos\varphi + n_1 y_2\sin\theta_1\sin\varphi) + \Phi(\theta_1,\theta_2,d)]\mathrm{d}\theta_1\mathrm{d}\varphi \end{aligned} \tag{1.22}$$

By using this equation, we study the intensity distribution of a tightly focused beam with the presence of different dielectric interfaces.

1.3.5.1 Dependency of the focal shift on different dielectric interfaces

Figure 1.24 shows the calculated results of intensity distribution for a tightly focused EM field in the vicinity of the focal region in the presence of different dielectric interfaces. Numerical calculations are carried out with: NA = 0.9, distance d = 5 μm, and different dielectric interfaces with $n_1/n_2 = 1.2/1.5$, $n_1/n_2 = 1.2/1.2$ and $n_1/n_2 = 1.5/1.2$, respectively. The incident beam is a right circularly polarized

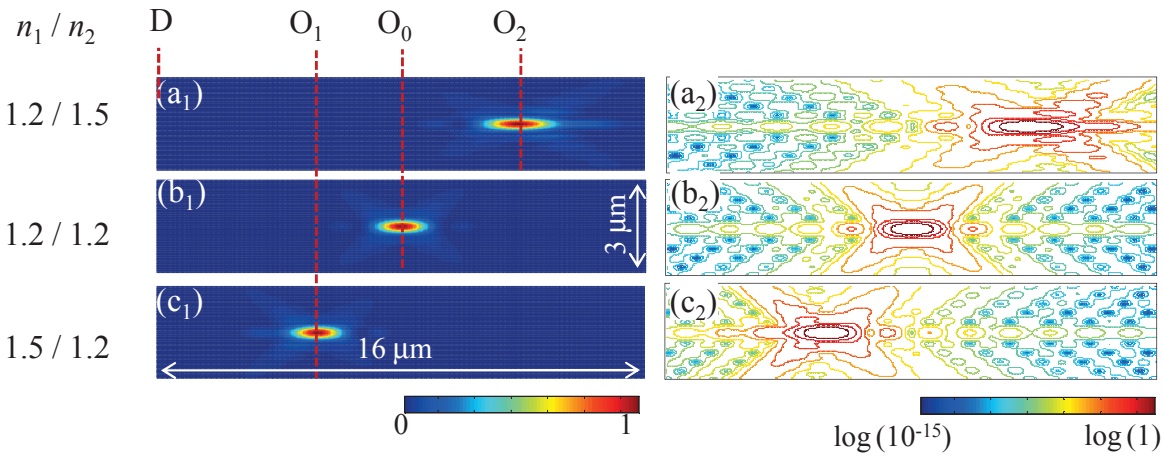

Figure 1.24: Influence of refractive index mismatch on the intensity distribution of focusing spot. (a_1) $n_1 = 1.2$, $n_2 = 1.5$, actual focal point is shifted to O_2 by $z_{\text{shift}} = +3.83$ μm. (b_1) $n_1 = n_2 = 1.2$, homogeneous medium, $z_{\text{shift}} = 0$ μm. (c_1) $n_1 = 1.5$, $n_2 = 1.2$, the focal point is shifted to O_1 by $z_{\text{shift}} = -2.76$ μm. [(a_2) - (c_2)] contour plots of intensity distribution (log scale) of [(a_1) - (c_1)]. $\lambda = 532$ nm, NA = 0.9. The interface D is positioned at left side of focal point with a distance $d = 5$ μm.

monochromatic plane wave ($\lambda = 532$ nm).

It is obvious that, as compared to homogeneous medium (Figure 1.24(b)), when the light beam propagates from a sparse to a dense material (Figure 1.24(a)), the focal spot is shifted to the right side of focal point O_0 ($z_{\text{shift}} = +3.83$ μm). In contrast, when light propagates from higher n to a lower refractive index, the focal spot is shifted to ($z_{\text{shift}} = -2.76$ μm) the left side of the initial focal point O_0 (Figure 1.24(c)).

We note that the absolute value of the focal point shifts are not the same with respect to the initial focal point O_0. A larger displacement of focal point is obtained in Figure 1.24(a) than in Figure 1.24(c). It is due to the fact that, for each diffracted ray, for example, the marginal ray, as illustrated in Figure 1.23, the distance $DO_{1(2)} = h \cot \theta_{a(b)}$, does not depend linearly on $\sin \theta$ (Snell's law). Hence, the relevant focal shift, (d−DO_1) and ($DO_2 - d$) are not same. The contour plot [Figures 1.24(a_2-c_2)], shows clearly that, due the to the spherical aberration caused from refractive index mismatch, the focusing spot shape is not symmetric along the optical axis and its size is bigger than the one obtained in the case of a homogeneous medium.

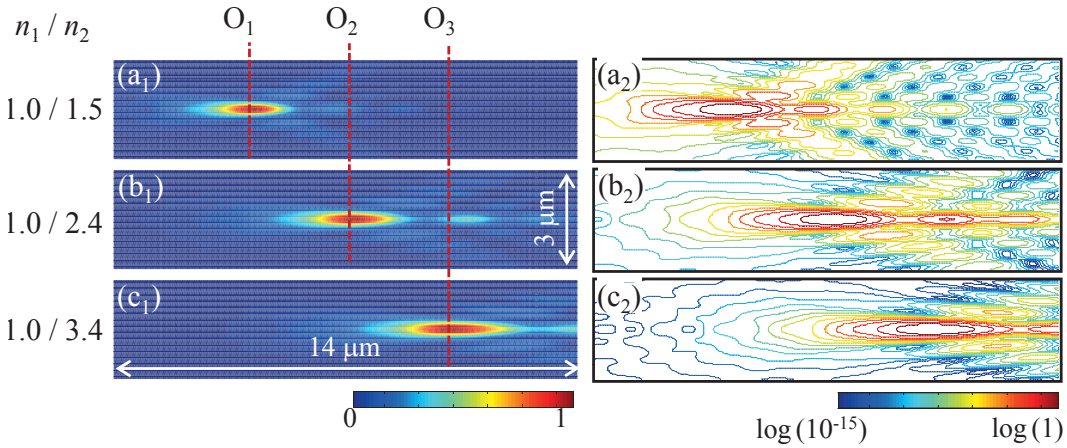

Figure 1.25: Effects of refractive index difference of medium on the intensity distribution of focusing spot (a_1): $n_1/n_2 = 1.0/1.5$, $z_{\text{shift}} = 4.11$ μm. (b_1): $n_1/n_2 = 1.0/2.4$, $z_{\text{shift}} = 10.36$ μm. (c_1): $n_1/n_2 = 1.0/3.4$, $z_{\text{shift}} = 17.72$ μm. [(a_2) - (c_2)] contour plots of intensity distribution (log scale) showed in [(a_1) - (c_1)]. $\lambda = 532$ nm, NA = 0.9. The interface D is positioned at left side of focal point with a distance $d = 5$ μm.

Similar to above calculations, we investigate the focal shift caused by the propagation from air ($n_2 = 1.0$) to different materials ($n_1 > 1.0$). The studied materials are oil ($n_2 = 1.5$), diamond ($n_2 = 2.4$) and silicon ($n_2 = 3.4$), respectively. As shown in Figure 1.25(a-c), when increasing the refractive index of the second medium (n_2 = 1.5 to 3.4), the focal spot is shifted dramatically from $z_{\text{shift}} = 4.11$ μm (a_1) to $z_{\text{shift}} = 17.72$ μm (c_1). The size of the focusing spot is much larger and shows some kind of 'tail' at the right side of focusing spot.

Figures 1.25(a_2-c_2) represent the contour plots (the log scale) of the intensity distributions shown in Figures 1.25(a_1-c_1). It is clear that, when the difference of refractive indices between the first and the second medium increases, the degradation of focusing spot quality becomes critical.

The calculated focal shift as a function of the refractive index of the second medium (n_2) is shown in Figures 1.26. Numerical results are obtained with NA = 0.9, $d = 5$ μm, and $n_1 = 1.0$. The focal shift shows a linear dependence on the refractive index of second medium (n_2). The correlation of the focal shift and the n_2 can be summarized as $z_{\text{shift}} = 7.09 \times (n_2 - 1.0)$ [μm]. Here, we note that, the formula derived from diagram (Figures 1.26) is obtained with fixed $n_1 = 1.0$ and fixed location of dielectric interface D (d = 5 μm). In the next section, we will

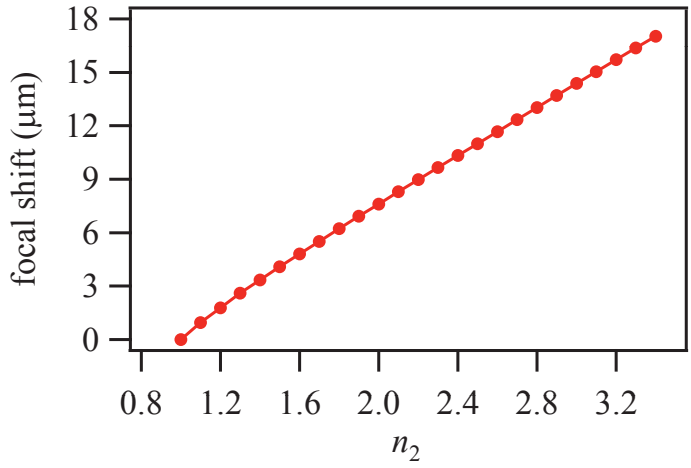

Figure 1.26: Calculation of focal shift as a function of refractive index of second medium (n_2). We assumed that $n_1 = 1.0$, $\lambda = 532$ nm, NA $= 0.9$. The interface D is positioned at left side of focal point with a distance $d = 5$ μm.

discuss about the influence of the location of the dielectric interface on the intensity distribution near the focal region of a high NA OL.

1.3.5.2 Dependence of the focal shift on the position of a dielectric interface

The variation of intensity distribution of the focusing spot as a function of the location of the dielectric interface D is shown in Figure 1.27. We have studied four different positions of D, which are: $d = 0$ μm; 5 μm; 10 μm; 15 μm, respectively. Numerical calculation results are obtained with NA $= 0.9$, $n_1 = 1.0$, $n_2 = 1.5$ and the incident beam is assumed to be circularly polarized ($\lambda = 532$ nm).

Figure 1.27 shows clearly that, when the depth of the interface (negative z_2 direction) increases from $d = 0$ to $d = 15$ μm, the focusing spot is shifted from 0 to 14.13 μm. Moreover, as compared to the spot size along the lateral direction, a dramatical elongation appears along optical axis. Hence, in various applications introducing focused beams, such as multi-layer compact disk, if there is a refractive index mismatch problem at the surface of disk, the vertical spacing of different layers inside the disk has to be increased to avoid an unwanted signal caused from the elongated shape (Figure 1.27(d)).

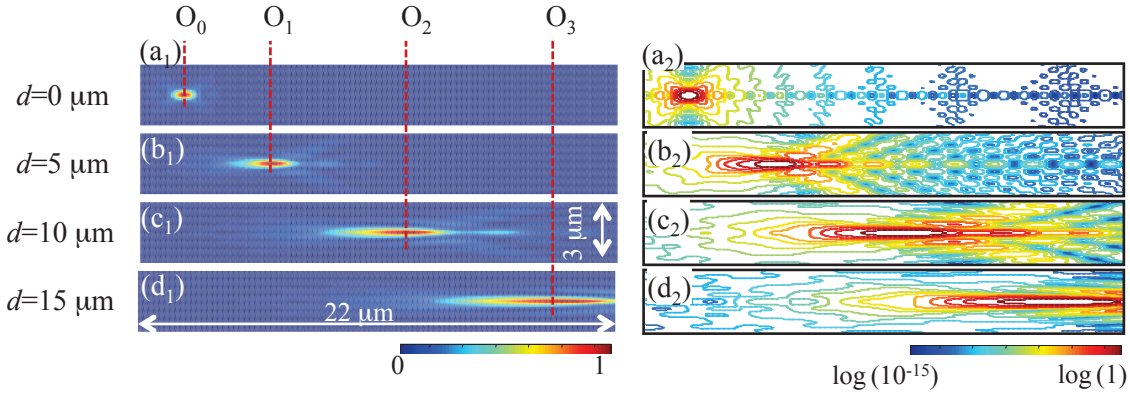

Figure 1.27: Effects of the depth (d) on the intensity distribution of focusing spot. (a) $d = 0$ μm, $z_{\text{shift}} = 0$ μm, (b) $d = 5$ μm, $z_{\text{shift}} = 4.11$ μm, (c) $d = 10$ μm, $z_{\text{shift}} = 7.25$ μm, (d) $d = 15$ μm, $z_{\text{shift}} = 10.13$ μm. [(a_2) - (c_2)] contour plots of intensity distribution (log scale) of [(a_1) - (c_1)]. $\lambda = 532$ nm, NA = 0.9. $n_1 = 1.0$, $n_2 = 1.5$.

Figures 1.27(a_2-d_2), show the contour plots (log scale) of intensity distributions corresponding to Figures 1.27($a_1 - d_1$). It further indicates the degradation of quality of focusing spot caused by the depth of the dielectric interface. However, since the lateral size is not significantly modulated, it can be used as a method for the generation of long needle-like fields in the focal region.

In conclusion, refractive index mismatch strongly affects the quality of a focusing spot. Hence, in practice, it is preferable to choose a coverslip, which has a proper thickness as well as same refractive index with respect to studied material.

Conclusion of chapter 1

In this Chapter, we have theoretically studied the intensity distribution of a focusing spot under tight focusing conditions. The main results can be summarized as follows :

- The NA of the OL has a direct impact on the size of the focusing spot. Numerical calculation showed that, when increasing NA, focusing spot size along transverse direction decreases towards the diffraction-limit, its longitudinal size also showing a dramatic decreasing trend. Moreover, under tight focusing

condition, (NA = 1.49, n = 1.515), the aspect ratio (L/T) of focusing spot decreases down to 2;

- Under tight focusing condition, the incident beam profile influences the shape of the focusing spot. For instance, with a higher order beam mode, Laguerre-Gaussian beam for example, instead of forming a Airy spot, a complex EM field distribution appears near the focal region;
- Introducing an optical mask in front of OL can induce numerous interesting results: Incident beam modulated by an amplitude mask induces a sub-diffraction limit focusing spot; A transversal doughnut spot is obtained from the incident beam modulated by a vortex mask; Light beam combined with $0/\pi-$phase mask possesses a longitudinal doughnut distribution in the focal region. Besides, we introduced a Cartesian coordinates system to simulate the intensity distribution of a tightly focused beam, with an asymmetric incident intensity profile. Numerical calculation results showed that an incident beam combined with a double-hole amplitude mask is able to create an isotropic focusing spot in the focal region. These focusing spots have very important applications, such as high capacity optical data storage, a 2D and 3D super resolution STED microscopies;
- With a high NA OL, the influence of the incident beam polarization on the intensity distribution of focusing spot is very significant. A linearly polarized incident beam induces an asymmetric focusing spot, which is elongated along the incident beam polarization direction. a circularly polarized incident beam is able to perform a perfectly symmetric distribution in the focal region. In the case of a radially polarized beam, a focusing spot with a dominant longitudinal component is obtained. A transversal doughnut focusing spot, which is purely transversally polarized, is obtained in the case of an azimuthally polarized incident beam;
- Refractive index mismatch causes focal shift in the focal region of OL. Due to the induced spherical aberration, the focusing spot quality is degraded. Hence, in high resolution imaging systems, using oil or other dielectric materials as immersion medium to preserve minimum aberration is important.

The fundamental investigation of the focusing behavior of high NA OLs indicate that a "good" focusing depends on many parameters. In the next chapter, we will discuss how to properly use those parameters to optimize the field distribution in the focal region for high resolution applications.

Chapter 2

Optimization of point spread function for different applications

2.1 Introduction

In some applications, a focusing spot with a particular intensity or polarization distribution can improve the working efficiency of optical microscopy. For example, for fluorescent imaging [1], a long focus depth is highly desired. For optical trapping [36] and STED microscopy, a narrow 'dark channel' field is preferred [37]. For micro-drilling, a focusing spot with a uniform flattop shape is necessary [38]. For single molecule detection and electron acceleration, a focusing spot with a particular polarization [39–41] distribution is highly demanded. Hence, the optimization of the standard Airy spot to satisfy the different applications is particularly interesting.

In recent years, many methods have been proposed to obtain a focusing spot with a particular intensity or polarization distribution. Wang *et al.* [27] reported the generation of long-needle (4λ) by using a radially polarized Bessel-Gaussian beam with a combination of a high NA OL and a binary phase mask. A sub-wavelength focal spot with a long focusing depth generated by a radially polarized annular beam was proposed by Kitamura *et al.* [42]. Bo *et al.* [43] reported a method for the creation of a sub-diffraction limited focal hole (0.5λ) with a long depth of focusing by using an azimuthally polarized Laguerre-Gaussian combined with an amplitude mask.

In this chapter, we investigate in detail the focusing behavior of a tightly focused beam with different polarizations and its combination to the optical masks.

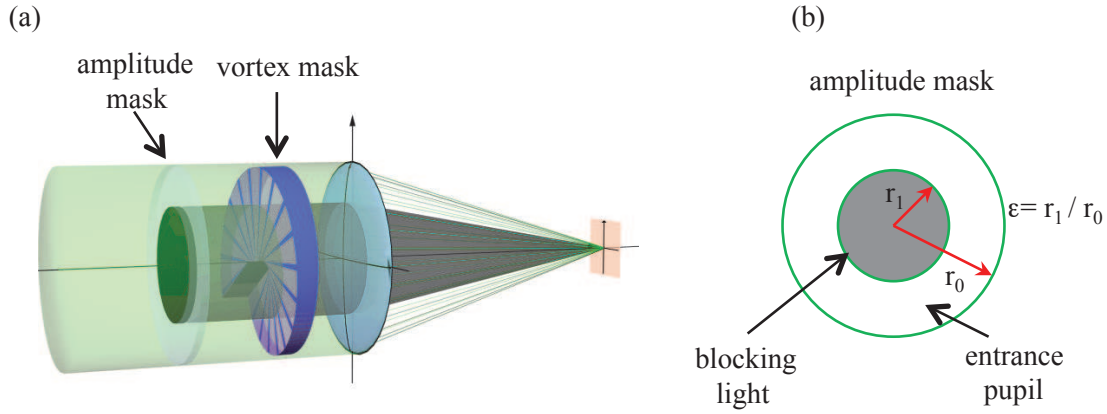

Figure 2.1: (a) Schematic of a high NA OL combined with vortex mask and amplitude mask. Vortex mask covers full aperture of objective pupil, and the blocked area of amplitude mask depends on ε, as shown in (b).

Moreover, we further propose methods for the optimization of the shape and the polarization distribution of focusing spot. The chapter is organized as follows: the generations of a long needle and long dark channel EM field in the focal region are presented in section 2; the new method for shaping a flattop focusing spot is introduced in section 3; the characterization and control of the polarization distribution in the focal region is discussed in section 4, and the main results and discussions will be presented in the last section.

2.2 Generation of a long needle and long dark channel field in the focal region

As shown schematically in Figure 2.1(a), we use different masks to realize the modulation of the phase and/or amplitude of different polarized incident beams. The introduced vortex mask, which fully covers the OL aperture of the objective, is used for the modulation of the phase of the incident beam. Intensity modulation of laser beam is realized by the amplitude mask. Depending on ε, which is the ratio of the radii of the blocked area and the OL aperture (Figure 2.1(b)), a laser beam with different intensity profiles are obtained.

2.2.1 Generation of a long needle focusing spot

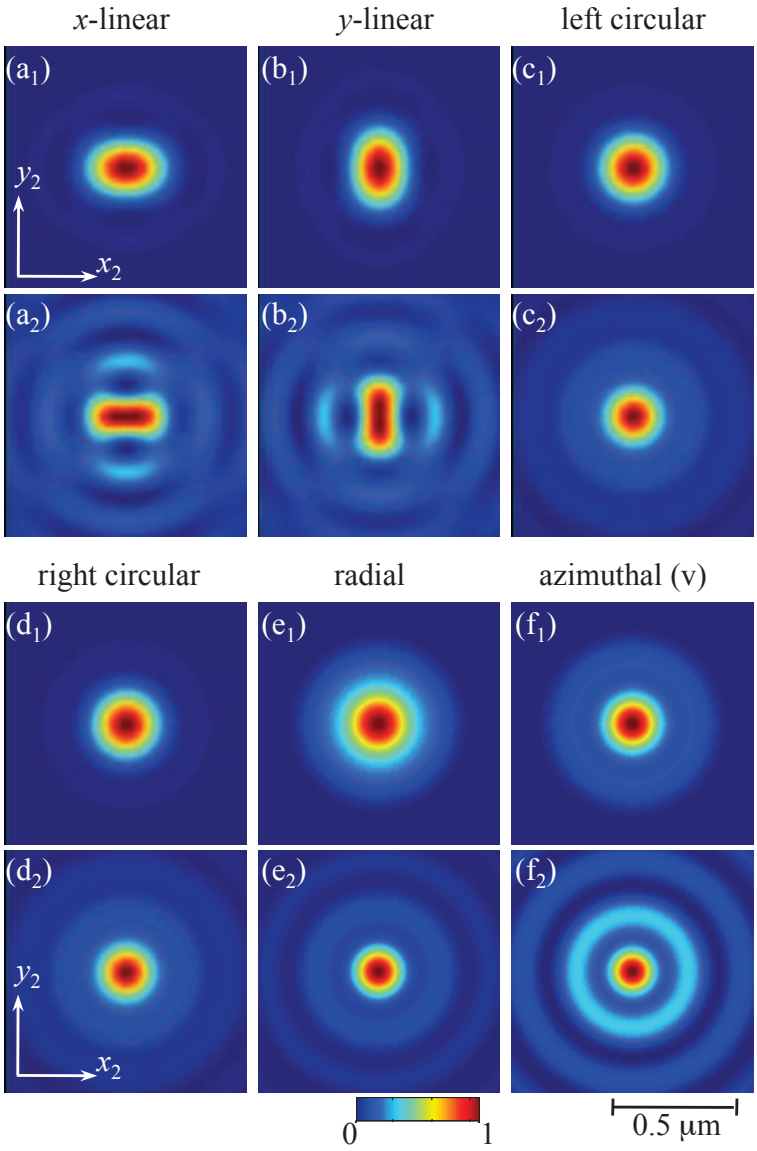

Figure 2.2: Calculated intensity distributions of the tightly focused of different polarized beams at $(x_2y_2)-$plane of focal region. [(a_1)-(f_1)] Absence of amplitude mask. [(a_2)-(f_2)] With presence of amplitude mask ($\varepsilon = 0.95$). The numerical calculation parameters are: $\lambda = 532$ nm, NA $= 1.4$, $n = 1.515$. In the figure (f), the "azimuthal (v)" indicates that the azimuthally polarized incident beam is modulated by vortex mask.

For the generation of a long needle-like focusing spot, using an amplitude mask is a proper choice, since it is able to compress the focusing spot along the transversal

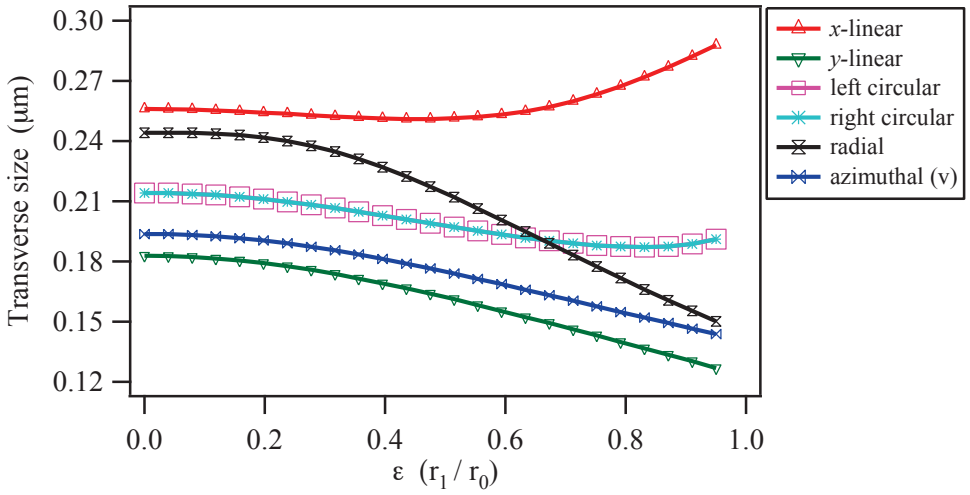

Figure 2.3: Variation of the transverse size (measured along x_2-axis) of the tightly focused different polarized beams as a function of the amplitude mask size.The numerical simulation parameters are: $\lambda = 532$ nm, NA $= 1.4$, n =1.515. "azimuthal (v)" indicates that the incident azimuthally polarized beam is modulated by vortex mask.

direction while elongating it along the optical axis (see Chapter 1).

As shown in Figure 2.2, the different polarized beams combined with an amplitude mask show many interesting behaviors. Figures 2.2(a_1-e_1) show the intensity distributions of different polarizations in the absence of amplitude mask ($\varepsilon = 0$), as studied in Chapter 1. Figures 2.2(a_2-f_2) display the relevant intensity distributions of the focusing spot in the presence of an amplitude mask ($\varepsilon = 0.95$). Figure 2.2(f_1) shows the Airy spot obtained from an azimuthal polarized incident beam modulated by a vortex phase plate ("azimuthal (v)"). It is due to the fact that the original existence of a $\pi-$phase difference in the azimuthally polarized beam (Figure 1.14(d) p_i and p_j) has been compensated by the vortex mask, and thus there is a constructive interference occurring when those diffracted rays, which are in phase, are adding up in the focal region.

In the case of $x-$ and $y-$linearly polarized incident beams, as compared to the absence of amplitude mask (Figures 2.2(a_1,b_1)), the asymmetric focusing behavior is quite significant (Figure 2.2(a_2,b_2)). It is due to the fact that, when an amplitude mask ($\varepsilon = 0.95$) is introduced, the contribution of the longitudinal component (E_{z_2}), which shows a doughnut shape along incident beam polarization direction (see Figure 1.15(d_1) in Chapter 1), is significantly enhanced. Thus, a pronounced

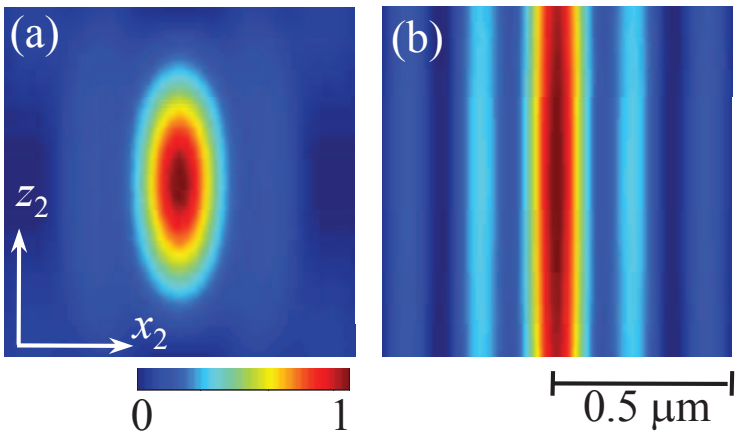

Figure 2.4: Generation of a long needle like field at focal region from a tightly focused azimuthally polarized beam combined with amplitude and vortex masks. (a) Field distribution in the absence of amplitude mask. (b) Field distribution in the presence of amplitude mask ($\varepsilon = 0.95$). The used parameters are: $\lambda = 532$ nm, NA $= 1.4$, $n = 1.515$.

asymmetric intensity distribution appears in the focal region. The linear polarization combined with amplitude mask is not suitable to generate a symmetric long needle field in the focal region.

Figures 2.2(c_2-f_2) show that, in the presence of an amplitude mask ($\varepsilon = 0.95$), the beams having a the right circular, left circular, radial and azimuthal (v) polarization possess symmetric intensity distributions in the focal region, and the obtained focusing spots are smaller than those in the absence of an amplitude mask (Figure 2.2(c_1-f_1)).

The calculated FWHM of the lateral sizes (measured along the x_2-axis) of the focusing spot at different ε of the amplitude mask are shown in Figure 2.3.

When increasing of ε, only the transverse size of the $x-$linearly polarized light (red line) exhibits an increasing trend. In the case of the $y-$linearly polarized light (green line), the lateral size is reduced to only 127 nm, which is much smaller than the diffraction limit (≈ 230 nm). However, as shown in Figure 2.2(b_2), the linearly polarized beam has an asymmetric focusing spot, its size being reduced along x_2-axis only. The size along the other transverse direction y_2-axis, should show the same behavior as the one in the case of $x-$linearly polarized beam along the x_2-axis (Figure 2.3 (red line)).

The right and left circularly polarized light beams have similar behaviors, in

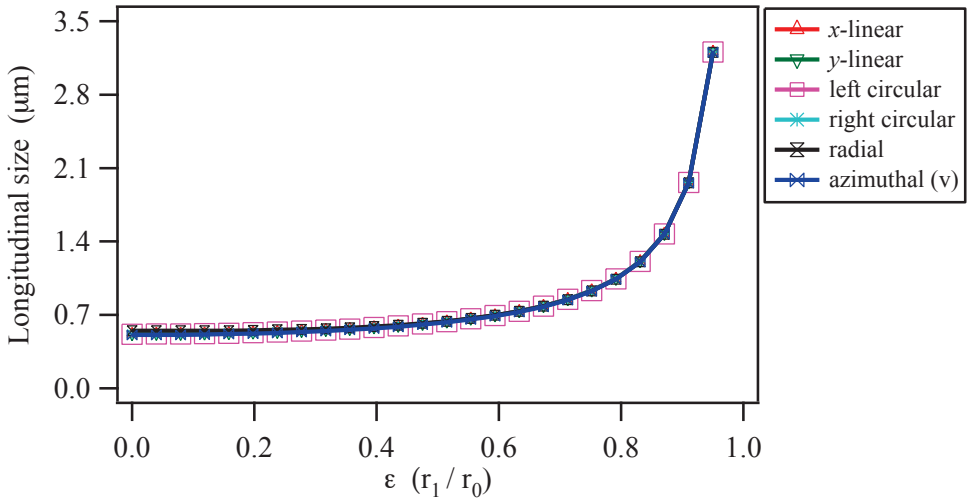

Figure 2.5: Effects of the ratio (ε) of r_1 and r_0 on the longitudinal size (along z_2-axis) of total intensity distribution of tightly focused different polarized beams. The simulated parameters are taken same as those in simulation parameters are same as those in Figure 2.3.

which size decreases from 214 nm ($\varepsilon = 0$) to 187 nm ($\varepsilon = 0.83$). When ε is larger than 0.83, the size tends to increase, for example at $\varepsilon = 0.95$, the spot size is 191 nm. As discussed in the previous chapter (Figure 1.9(c_1, d_1)), this is due to the fact that the size of the radial components (E_{x_2}, E_{y_2}), decreases when increasing ε. However, when ε increases, the portion of the longitudinal component (Figure 1.9(e_1)), which has a doughnut shape in the focal region, also increases. The variation of total intensity distribution is the consequence of the competition of the radial and longitudinal components in the focal region.

In the case of a radially polarized incident beam, the transverse size of the focusing spot decreases from 244 nm ($\varepsilon = 0$) to 150 nm ($\varepsilon = 0.95$), corresponding to a reduction up to 39%. The reason is that, in contrast to the circularly polarized light, the longitudinal component of a radially polarized beam (Figure 1.19(d_1) in Chapter 1) has an Airy spot shape while the radial components (Figure 1.19(b_1, c_1) in Chapter 1) possesses a doughnut shape, and thus when ε increases, the portion of the longitudinal component increases and the total focal spot size is greatly decreased. Using a radially polarized incident beam combined with an amplitude mask to create a sub-diffraction limit focusing spot is considered as one of the most proper ways to obtain high resolution focusing spots [27, 42, 44].

With the combination of an azimuthally polarized incident beam and a vortex phase plate (blue line in Figure 2.3), the obtained smallest lateral size is 143 nm (for $\varepsilon = 0.95$). It is interesting to see that, its size is smaller than the one obtained from a radially polarized light. Figure 2.4 shows the intensity distribution of azimuthally polarized beam at $(x_2 z_2)-$plane in the focal region. It is clear that, when combining amplitude and vortex masks, the field distribution in the focal region is narrowed along the transverse direction, meanwhile, along the optical axis, it possesses a enhanced field distribution.

Since, a smaller size is obtained than when using a radial polarization, as frequently reported in the literature, the combination of an azimuthal polarized beam with an annular mask can be a very good method for the creation of sub-diffraction focal spots.

The calculated longitudinal size of the focusing spot from different polarized beams are shown in Figure 2.5. When increasing the ratio ε, the longitudinal size from different polarized beams have the same behavior. In all cases, the FWHM of the longitudinal size is increased from 0.5 μm to 3.2 μm. It is due to the fact that, when introducing an amplitude mask, the modulation of laser beam along its radial direction is always the same.

We should consider all these factors (lateral, longitudinal size and shape of focal spot) and draw a conclusion that, circularly, radially and azimuthally polarized beam combined with an amplitude mask are able to create a long narrow focusing spot in the focal region. In particular, in the case of an azimuthally polarized beam combined with a vortex mask, the generated focusing spot has the smallest size along transverse direction.

Besides, the generation of a dark channel-like field, which is very important for many applications, is also an interesting task.

2.2.2 Generation of a long dark-channel field in the focal region

As discussed in the previous chapter, there are two ways to obtain a transverse doughnut focusing spot. The first one is the use of a vortex phase mask and the other one is enabled by employing an azimuthally polarized incident beam. For the sake of understanding the behaviors of different polarized beams modulated by vortex

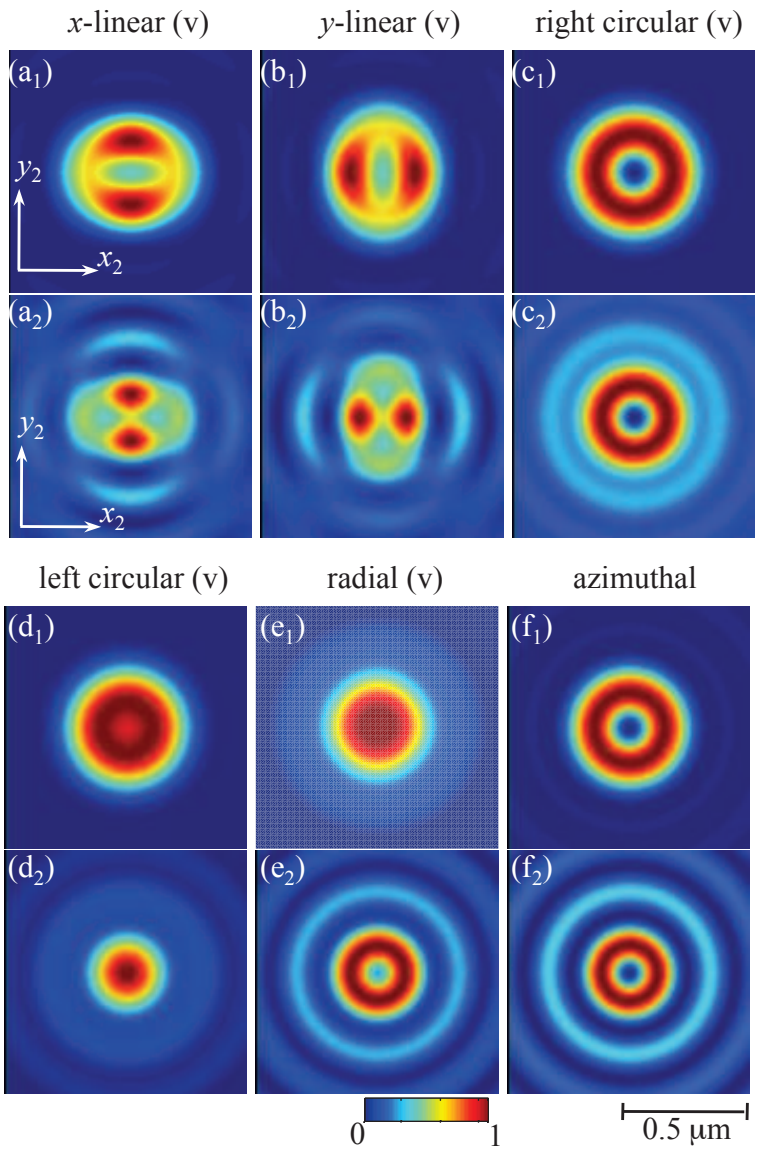

Figure 2.6: Calculated intensity distribution of focusing spot of the different polarized incident beams combined with vortex phase plate and amplitude mask. [(a_1)-(f_1)] The intensity distribution of focusing spot in the absence of amplitude mask ($\varepsilon = 0$). [(a_2)-(f_2)] The intensity distribution of focusing spot with presence of the amplitude mask ($\varepsilon = 0.95$). The numerical calculation parameters are: $\lambda = 532$ nm, NA $= 1.4$, $n = 1.515$.

mask and amplitude mask, we have investigated here six kinds of polarizations.

As shown in Figures 2.6(a_1-f_1), in the absence of an amplitude mask ($\varepsilon = 0$), under modulation by a vortex mask, different polarized beams induce different in-

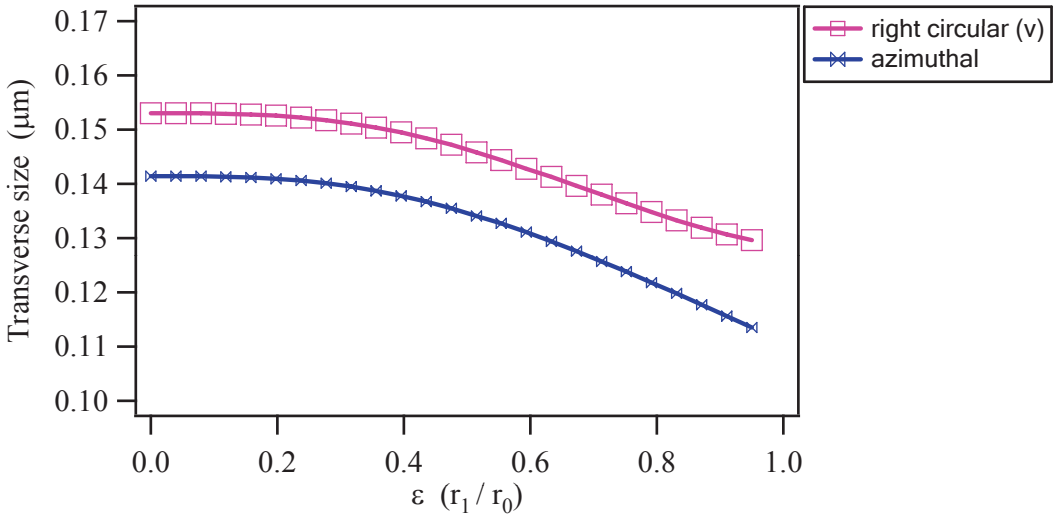

Figure 2.7: Variation of the transverse doughnut size (along x_2-axis) of the tightly focused right circular (v) and azimuthally polarized beams. The computed parameters are same as those in the Figure 2.6.

tensity distributions in the focal region. In the case of a linearly polarized beam (Figure 2.6(a_1, b_1)) combined with a vortex mask, a doughnut shape appears but the intensity at the doughnut center is not totally vanished. With a left-circularly polarized incident beam (Figure 2.6(d_1)), because the orientation of beam polarization is not matched with the vortex beam phase delay direction ($0 \rightarrow 2\pi$), a large focusing spot appears in the focal region. Here, we note that, if the vortex phase plate is designed as $2\pi \rightarrow 0$, the left circularly polarized beam results in a doughnut shape which is same as for the right circular does (Figure 2.6(c_1)). In the case of a radially polarized incident beam (Figure 2.6(e_1)), there is no doughnut shape in the focal region.

Figure 2.6(a_2-f_2) show the intensity distribution at the focusing region obtained for different polarized incident beams, which are modulated by an amplitude mask ($\varepsilon = 0.95$). It shows clearly that doughnut spots from right circular (v) Figure 2.6(c_2) and azimuthal polarization Figure 2.6(f_2) are smaller than those obtained in the absence of the amplitude mask (Figure 2.6(c_1, f_1)). Note that Figure 2.6(c_2) shows a doughnut profile, but the intensity at the center is not totally vanished , it still possesses 32% of total intensity.

Hence, for generation of a doughnut focusing shape, the use of right circularly (v) and azimuthally polarized beams are proper choices. Figure 2.7 shows that, when

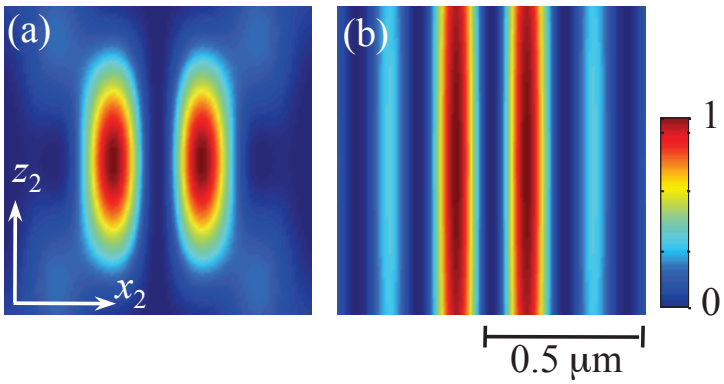

Figure 2.8: Generation of a long dark channel by azimuthally polarized beam combined with amplitude mask. (a) Without amplitude mask. (b) With amplitude mask, $\varepsilon = 0.95$, simulation parameters are taken same as those in Figure 2.6.

increasing of ε, in both cases, right circular (v)(pink line) and azimuthal polarization (blue line), the size of the doughnut is getting smaller. The spot size obtained from azimuthal polarization has a minimum size of 114 nm ($\varepsilon = 0.95$), which is much smaller than the the one obtained from a circular polarization (130 nm).

Figure 2.8 shows the intensity distribution of an azimuthally polarized beam at the $(x_2z_2)-$plane in the focal region. It is clear that when introducing an amplitude mask ($\varepsilon = 0.95$), the EM field distribution is strongly narrowed in transverse direction and elongated along its longitudinal direction. This focusing spot is often called an optical long dark channel.

As plotted in Figure 2.9, the FWHM of the dark channel along the z_2-axis (length of dark channel), is increased dramatically from 0.54 μm to 3.2 μm when ε increases from 0 to 0.95.

As a conclusion, the generation of long dark channel-like fields in the focal region, can be achieved either by using a right circularly polarized incident beam combined with a vortex phase plate or by using an azimuthally polarized incident beam. In both cases, in the presence of amplitude mask, the longitudinal sizes of the dark channel can be up to 3.2 μm. As compared to the lateral size of dark channel obtained from a right circularly polarized light (v) (130 nm), the one from an azimuthally polarized incident beam has a smaller diameter (114 nm).

In contrast to a long focusing spot, it may be possible to generate a flattop shape, which is also very interesting for many applications, such as optical printing, optical data processing [45] and micro-lithography [46]. In the next section we will present

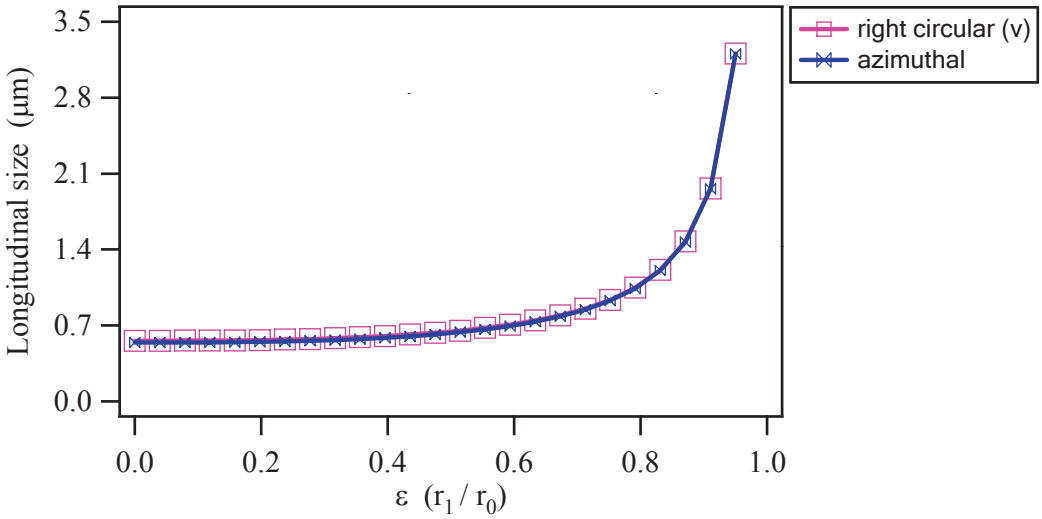

Figure 2.9: Variation of the longitudinal size of dark channel (along z_2-axis) as a function of the amplitude mask size. The numerical calculation parameters are taken as those used in the Figure 2.6.

a new method for generating a flattop focusing spot.

2.3 Creation of the transversal flattop field distribution in the focal region

2.3.1 Review of the generation of flattop field from cylindrical vector beam

As discussed in the previous chapter, under a tight focusing condition, the cylindrical vector beam displays very interesting behavior in the focal region. For example, the radially polarized incoming light induces an Airy spot with a dominant longitudinal component (Figure 2.10(a)). The azimuthally polarized incident beam creates a doughnut spot (Figure 2.10(e)) in the focal region. As shown in the top row of Figure 2.10, the polarization states of the incident beam can be represented by the θ_0 angle, which is defined as the angle between the local polarization direction and the radial direction of laser beam. Hence, the radial polarization is indicated by $\theta_0 = 0°$ while the azimuthal polarization is represented by $\theta_0 = 90°$.

As shown in Figures 2.10(a-e), when increasing θ_0 from 0° to 90°, the relevant

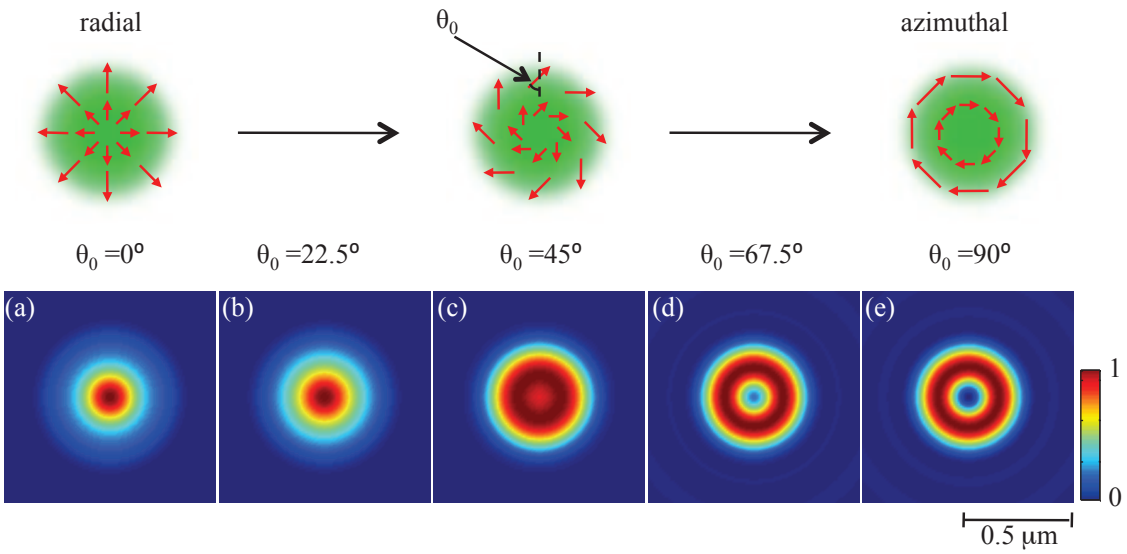

Figure 2.10: Variation of focusing spot shape regarding the incident beam polarizations. θ_0 is the angle between the local polarization direction and its radial direction. $\lambda = 532$ nm, NA $= 1.4$, $n = 1.515$.

focusing spot shape is converted from an Airy spot (a) to a doughnut shape (e). With a proper θ_0 angle, a focusing spot with flattop shape may appear.

Figure 2.11 shows the variation of different field components as a function of the θ_0 angle. Numerical calculation parameters are: NA $= 1.4$, $n = 1.515$, $\lambda = 532$ nm. As shown in the figure, at $\theta = 39.6°$ (black line), a flattop shape intensity profile appears in the focal region. The size of flattop spot (FWHM) is around 423 nm, which is two times larger than the size of a standard focusing spot (210 nm) (Figure 1.18). This flattop shape due to the fact that, the increasing of the angle θ_0, the contribution of the longitudinal component (blue line) decreases while the contribution of transversal components (red line), having a doughnut shape, increases. At $\theta_0 = 39.6°$, due to the equivalent distribution of these components, the total intensity displays a flattop shape. This results (flattop at $\theta_0 = 39.6°$) is differ from that reported by Zhan *et al.* [47] (flattop at $\theta_0 = 24°$). In their case, they use a lower NA OL (NA $= 0.8$, $n = 1.0$), then, the variation of different field components are accordingly different.

In this work, we studied how to control the contribution of the different components in order to generate a flattop shape with larger size. In the next subsection, we will present a novel method for the generation of a very large flattop shape focusing

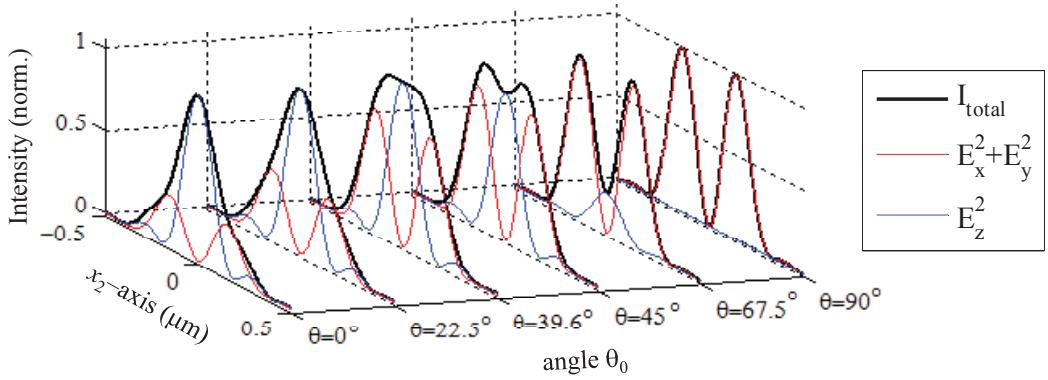

Figure 2.11: The variation of different field components of focusing spot as a function of θ_0. Numerical calculation parameters are: NA = 1.4, $n = 1.515$, $\lambda = 532$ nm.

spot.

2.3.2 The generation of flattop focusing spot by a hybrid polarized beam

Here, we employed again radially (Figure 2.12(a)) and azimuthally polarized (Figure 2.12(b)) incident beams to generate a flattop field distribution in the focal region. Instead of changing the local polarization angle θ_0 as in the previous section, here, we use a "hybrid" polarized incident beam (Figure 2.12(c)).

The laser beam is defined as follows: the light from the center of beam (radius r_1) is azimuthally polarized and the one from outer part $(r_0 - r_1)$ is radially polarized. ε is the ratio of r_1 and r_0. When $\varepsilon = 0$, the incoming beam is fully radially polarized while $\varepsilon = 1$, the incoming beam is azimuthally polarized. It is obvious that, using a proper ε $(0 \leq \varepsilon \leq 1)$, there should exist an hybrid polarization states, which can induce a flattop field distribution in the focal region. In fact, the azimuthally polarized light induces a doughnut spot with any size of aperture, but the radially polarized beam induces a doughnut shape in the focal region when the aperture is particular small. Hence, the inner part of this "hybrid" polarized beam is azimuthally polarized while the outer part is radially polarized. The combination of these two polarizations allows thus obtaining a flattop focusing spot.

The variation of the intensity distribution of the focusing spot as a function of

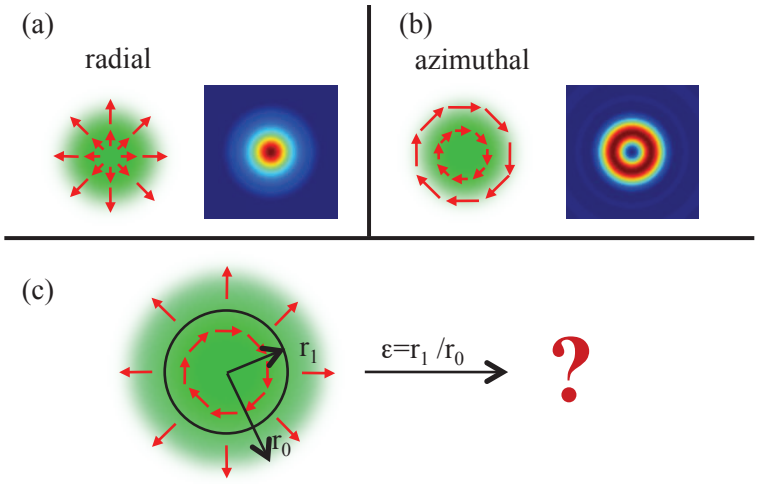

Figure 2.12: Schematic diagrams of different polarized beams. (a) Radially polarized beam and corresponding focusing spot. (b) Azimuthally polarized beam and corresponding focusing spot. (c) Beam polarization with consisting of the azimuthal (inner) and the radial (outer) polarizations . r_0, r_1 are radii of the full OL aperture and inner part, respectively.

the ratio ε is shown in Figure 2.13. It shows clearly that, when increasing ε, the intensity distribution around the focal point is enhanced ($\varepsilon = 0.7$). For $\varepsilon = 0.82$, a focusing spot with largest flattop appears in the focal region. When the ratio is up to $\varepsilon = 0.9$, the intensity distribution at the center of the focusing spot is significantly decreased and turns into a doughnut shape at $\varepsilon = 1$.

This can be explained by examining the field distribution of different components, as shown in Figure 2.14. As shown in Figure 2.14, when increasing ε, the portion of radial component (red line), which has doughnut shape, increases. At $\varepsilon = 0.82$, the radial component (red) has an equivalent intensity with the longitudinal component (blue line). This behavior is almost has same as that discussed in the previous section (Figure 2.11). However, in this case, due to the smaller aperture ($r_1 = 0.82r_0$) of the azimuthally polarized beam, the doughnut component at $\varepsilon = 0.82$ (red line in Figure 2.14) is larger than the one presented in Figure 2.11 (red line at $\theta_0 = 39.6$), and thus it displays a much larger flattop intensity distribution in the focal region. The size (FWHM) of this focusing spot is up to 580 nm. As compared to that obtained in the previous section (Figure 2.10) (423 nm), the size of the flattop is increased by 137%. Here we note that, at the top part of the intensity profile (red line, $\varepsilon = 0.82$), there is a small 'fluctuation'. However, it can be considered as

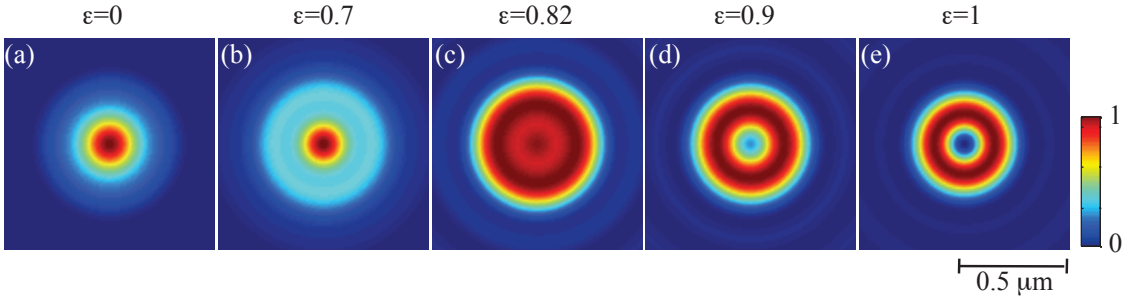

Figure 2.13: Variation of focusing spot shape regarding the ratio (ε) of r_1 and r_0. The polarization states of incident beam is shown in Figure 2.12 (c), $\lambda = 532$ nm, NA = 1.4, n =1.515.

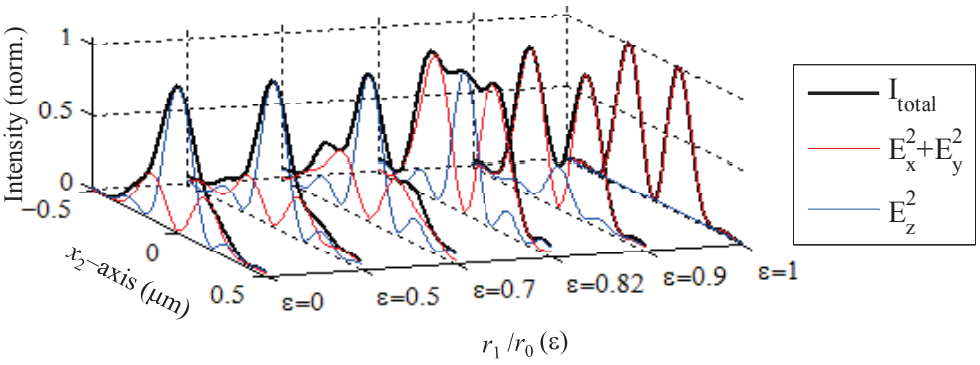

Figure 2.14: Variation of different components of focusing spot as a function of ε. NA=1.4, $n = 1.515$, $\lambda = 532$ nm. The focusing spot with flattop shape appears at about $\varepsilon = 0.82$.

negligible since it is only 7% of the peak intensity.

As a summary of this section, we have proposed several methods to generate a long needle, a long dark channel and a flattop shape intensity distribution in the focal region. The methods for the generation of these particular intensity distributions are based on the fine control of the phase,amplitude, and polarization of the incident beam. In practice, we are able to generate these particular intensity distributions, because of the availability of high resolution optical masks, such as spatial light modulator and liquid crystal theta cells.

Besides shaping of the intensity distribution of EM field in the focal region, in recent years, polarization distribution or polarization shaping of EM field in the

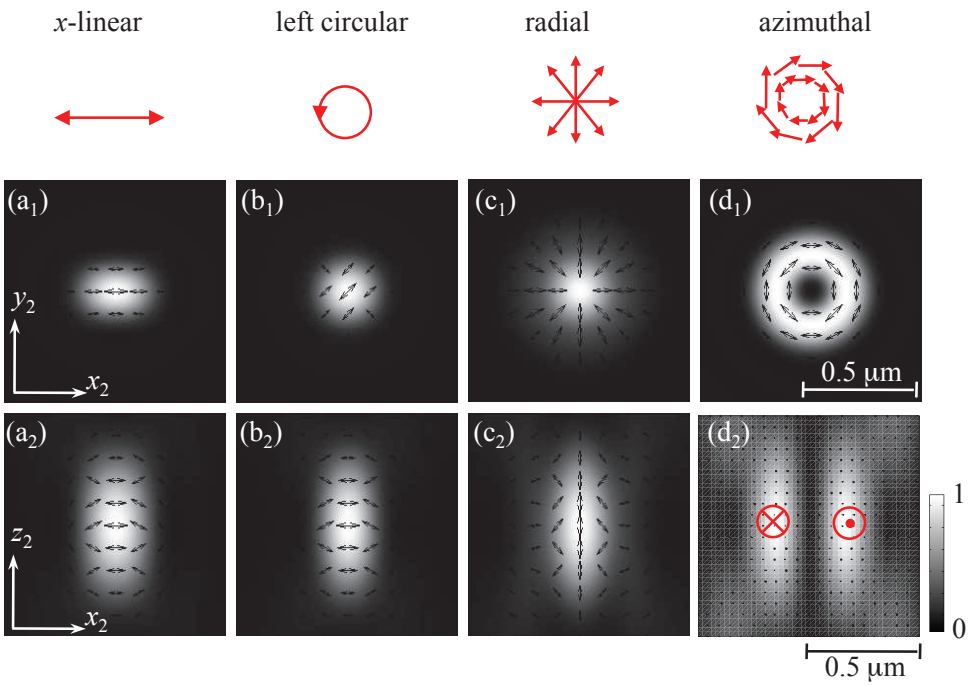

Figure 2.15: Polarization distribution of different polarized tightly focused beams. (a) $x-$linearly polarized. (b) Left circularly polarized. (c) Radially polarized. (d) Azimuthally polarized. Subscripts 1, 2 indicate the intensity distribution at $(x_2y_2)-$, $(x_2z_2)-$planes, respectively.

focal region becomes an increasing demand for many applications, such as dipole excitation and single-molecule detection or polarization sensitive optical data storage. In the next section, we will present the study of polarization distribution of tight focused beam in the focal region.

2.4 Control of the polarization distribution of a tightly focused beam in the focal region

2.4.1 Polarization distribution of tightly focused different polarized incident beams

Under tight focusing conditions (NA $>$ 0.7) [19], due to the significant converged light beam, a new field component appears in the focal region. For instance, in the case of a radially polarized incident beam, a significant portion of the longitudinal

component emerges in the focal region. According to different polarized incident beams, the complex field distributions in the focal region are also different. In this work, we present the polarization distribution in the focal region for four kinds of polarized incident beams. The schemes of these input beam polarizations are shown on the top part of Figure 2.15. For numerical calculations, we assume that the incident beam has uniform intensity profile and the wavelength, $\lambda = 532$ nm.

Numerical calculation results are shown in Figure 2.15. The arrows in the graphs indicate the projection of the 3D field distribution, which is related to its background intensity distribution plane. The length of the arrows represent the strength of EM field vector. It is clear that, with different polarized incident beams, the polarization distribution near focal region are quite different.

With a $x-$linearly polarized incident beam (Figure 2.15($a_{1,2}$)), at $(x_2z_2)-$plane, the field is mainly $x-$linearly polarized. However, at the $(x_2z_2)-$plane, the polarization direction of light located around the optical axis, is significantly tuned and tends to align along the optical axis. This behaviour is caused from the emerged longitudinal component under tight focusing conditions.

In the case of a circularly polarized incident beam (Figure 2.15(b_1)), due to the equivalent polarization strength of the $x-$ ($p_x = i/\sqrt{2}$) and $y-$components ($p_y = i/\sqrt{2}$) (Table 1.3 in Chaper 1), at $(x_2y_2)-$plane, the polarization direction shows a 45° angle with respect to the x_2- or y_2-axis. At $(x_2z_2)-$plane (Figure 2.15(b_2)), due to the significant portion of the emerging z_2-component, which has doughnut shape, the EM field shows a similar polarization distribution as in the case of a linearly polarized light (Figure 2.15(a_2)).

In the case of a radially polarized incident beam (Figure 2.15(c_1)), there is a axial symmetrical polarization distribution at $(x_2y_2)-$plane. It is interesting to see that the field distribution in the focal region is polarized along the optical axis (Figure 2.15(c_2)), which is very important for the application in the field of particle acceleration [48].

In contrast to the radial polarization case, with an azimuthally polarized incident beam (Figure 2.15(d)), at $(x_2y_2)-$plane, the polarization is rationally around optical axis in the focal region. At $(x_2z_2)-$plane, it shows that there is no longitudinal component, the field is purely transversely polarized in the focal region. This pure-transversal field distribution is a high demand for energy-efficient microscopic applications in harmonic generation [40, 41].

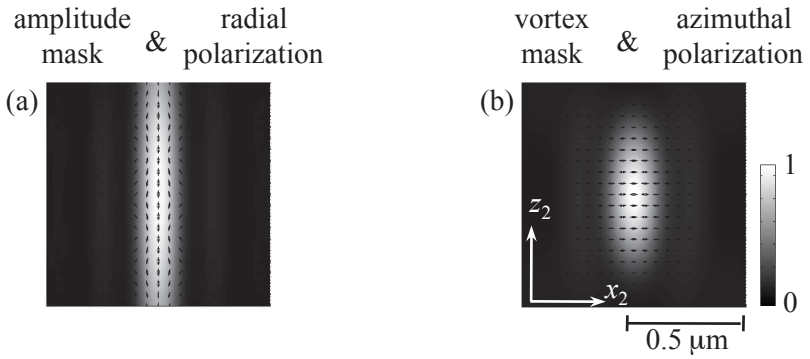

Figure 2.16: Control of the polarization distribution in the focal region. (a) Longitudinal-component dominated focusing spot (amplitude mask: $\varepsilon = 0.95$). (b) Radial component dominated focusing spot. The arrows indicate the polarization direction, and its length is related to the field strength. The simulations are realized with NA = 1.4, $n = 1.515$. $\lambda = 532$ nm.

2.4.2 Control of the polarization distribution in the focal region

In this subsection, we study the generation of the longitudinal field or of the transversal dominating field in the focal region.

The longitudinal field component in the focal region is often enhanced in the following conditions:

- ▶ a high NA OL, because a higher NA lens refers to a larger open angle α. When α increases, rays strongly converges and the portion of longitudinal component accordingly increases.
- ▶ a radially polarized incoming light (Figure 2.15(c_2)).
- ▶ introducing an amplitude mask in front of objective aperture.

Thus, in order to maximize the longitudinal component distribution in the focal region, we propose to use a high NA OL (NA = 1.4, $n = 1.515$) combined with an amplitude mask ($\varepsilon = 0.95$) to tightly focus a radially polarized beam. Indeed, as shown in Figure 2.16(a), when introducing an amplitude mask ($\varepsilon = 0.95$), the longitudinal component is greatly enhanced.

For the generation of a transverse dominating field in the focal region, an azimuthally polarized incident beam is an ideal choice, because there is no longitudinal component appears when it is focused into the focal region. Therefore, an az-

imuthally polarized incident beam often induces a doughnut focusing spot near focal region. For generating an Airy spot with a purely transverse polarized field, a vortex phase mask, which modulates the phase of the incoming beam axial rotationally from 0 to 2π, can alternate the destructive interference (doughnut distribution) to a constructive case to perform an Airy spot. In figure 2.16(b), the polarization distribution shows that the azimuthally polarized incoming light combined with a vortex phase mask allows inducing an Airy spot shape, which exhibits a pure-transverse field component.

Conclusion of chapter 2

In summary, in this chapter, we have studied different methods to optimize the intensity and polarization distributions of the EM field in the focal region. First, we have demonstrated several ways to generate a long needle-like, a long dark channel-like and a flattop focusing spot, which are highly desired in many disciplines, such as microscope imaging, optical lithography, optical tweezers and so on. Then we analysed the polarization distribution in the focal region of different polarized incident beams. We introduced methods for the generation of longitudinal or transversal components dominating fields in the focal region, which are important for polarization sensitive applications, such as particle acceleration [40,41], optical data storage [49], etc. The proposed methods mainly focused on the fine control of the main parameters of incident beam: polarization, phase and amplitude distribution. The field distribution can be further optimized by using particular beam mode such as Bessel-Gaussian, Laguerre-Gaussian beams and also by using high order optical masks such as one-dark ring [50] or binary masks [27].

Chapter 3

Super-resolution microscope for nano-imaging and nano-fabrication

3.1 Review of stimulated emission depletion microscopy

In 1994, stimulated emission depletion (STED) fluorescence microscopy, which breaks down the well-known diffraction barrier, was first proposed by Stefan Hell *et al.* [2]. Its resolving power along lateral direction is greatly enhanced and towards nanoscale. As shown in Figure 3.1(a), in a standard STED microscopy configuration, there are two light sources, one is called excitation beam (green light) and the other is called STED beam (red line). The excitation beam, which is either a continuous or pulsed laser, is tightly focused into the focal region to illuminate an underlying specimen labeled by a fluorescent dye. As in a conventional confocal laser scanning microscopy, the excitation beam induces a diffraction-limited focusing spot, which is around half of wavelength of the excitation beam (Figure 3.1(b_2)). The materials that are covered by this diffraction-limited area are possible to absorb photons and subsequently emit photons by spontaneous emission.

By introducing the STED beam ('switched on'), which induces a doughnut focusing spot in the focal region under the assistance of a vortex mask (Figure 3.1(b_1)), the excited electrons from the area of the doughnut spot region turn to emit photons by stimulated emission instead of spontaneous emission. Hence, according to the different spectral behaviors of stimulated and spontaneous emissions, the fluo-

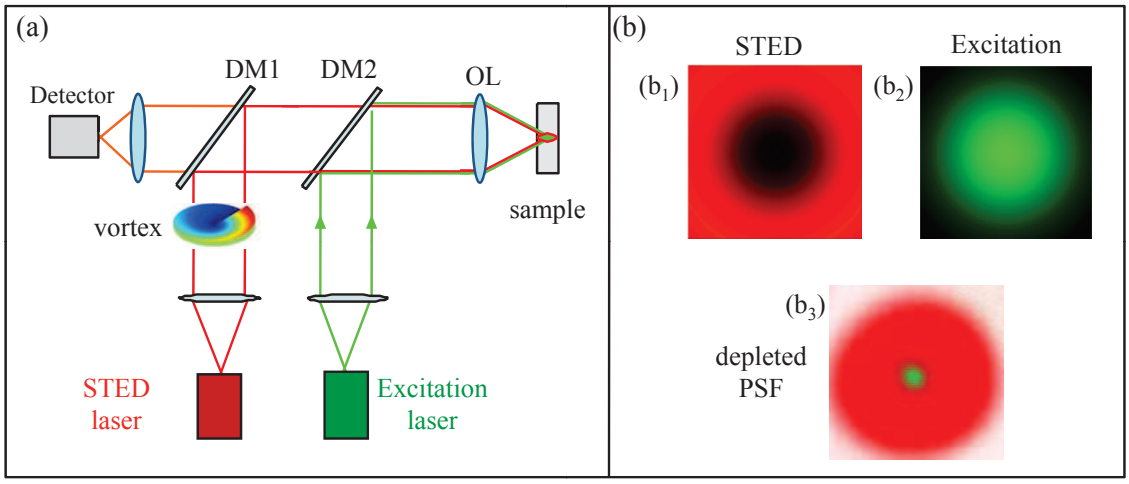

Figure 3.1: (a) Schema of the STED microscopy. (b) Intensity distribution of STED beam (b_1) excitation beam (b_2), and depleted effective PSF (b_3) in the focal region. DM1, DM2: dichroic mirrors, OL: objective lens.

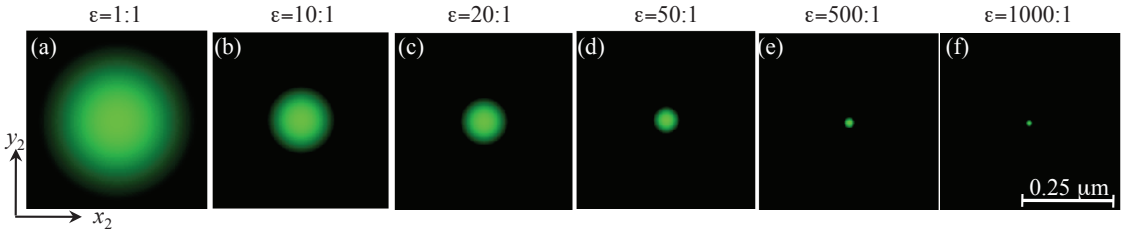

Figure 3.2: Variation of depleted focusing spot size regarding the ratio of I_{sat} and I_{STED}. The numerical calculation parameters are: $\lambda_{ex} = 532$ nm, $\lambda_{\text{STED}} = 760$ nm, NA $= 1.4$, $n = 1.515$.

rescence signal, which emerges only from the nonoverlapped center of the focusing spot (green spot in Figure 3.1(b_3)), will be selectively collected. Due to the nonlinear depletion caused by STED beam, this effective area is much smaller than the diffraction limit.

The key parameter of the STED technique is the existence of a saturated absorption threshold for fluorescence materials. Hence, by increasing STED beam intensity, which can be much higher than the fluorescence saturated level, the effective doughnut size can be narrowed down to nano-scale, and thus the resolving power of STED microscopy is greatly enhanced. The mathematics representation of

the lateral resolution of STED microscopy is given as [51]:

$$d = \frac{\lambda}{2n \sin\alpha \sqrt{1 + I_{\mathrm{STED}}/I_{\mathrm{sat}}}}, \tag{3.1}$$

where λ is wavelength of the excitation beam, α is the maximum open angle of the OL, n is the refractive index of the immersion medium. As shown in Figure 3.2, when increasing the ratio ε, which is defined as the ratio of STED beam intensity I_{STED} and the saturation level I_{sat}, the effective "PSF" size is dramatically decreased to nanometer scale. Up to now, according to the reported experimental results [52], a lateral resolution of STED microscopy of around 2.4 nm can be achieved. From the theoretical point of view (Eq. (3.1)), there is no limitation for STED microscopy if we can increase I_{STED}. Thus, when introducing a second light source (STED beam), it is possible to perform a microscopy resolution up to nanoscale. However, due to the lack of confinement along the longitudinal direction, the axial resolution of STED microscope is the same as for conventional laser scanning confocal microscopy, which is about several hundreds nanometers. In the next section, we will introduce methods for generating 3D doughnut focusing spots for a 3D super-resolution STED microscopy.

3.2 3D super-resolution microscopy

In order to deplete the fluorescence emission along transversal as well as along optical axis to achieve 3D super-resolving capability, beside the STED beam, which induces transversal doughnut (Figure 3.3(a)), Stefan Hell *et al.* [16] proposed to introduce a second STED beam. Before entering the objective pupil, this laser beam is pre-modulated ($0/\pi-$phase mask), and thus the field distribution in the focal region possesses an axial doughnut shape (Figure 3.3(b)). Due to the non-correlation of those light sources (two STED beams), the total intensity of the transversal and axial doughnut fields, has a perfect 3D doughnut profile in the focal region. Similarly to the 2D STED does, by increasing the intensities of these two STED beams, super-resolution along all axes can be achieved. In practice, the use of three laser beams, which are needed to be super-overlapped in the focal region, needs a complex and expensive optical system. In the next part, we presents a handy method for the generation of a 3D doughnut field distribution in the focal region.

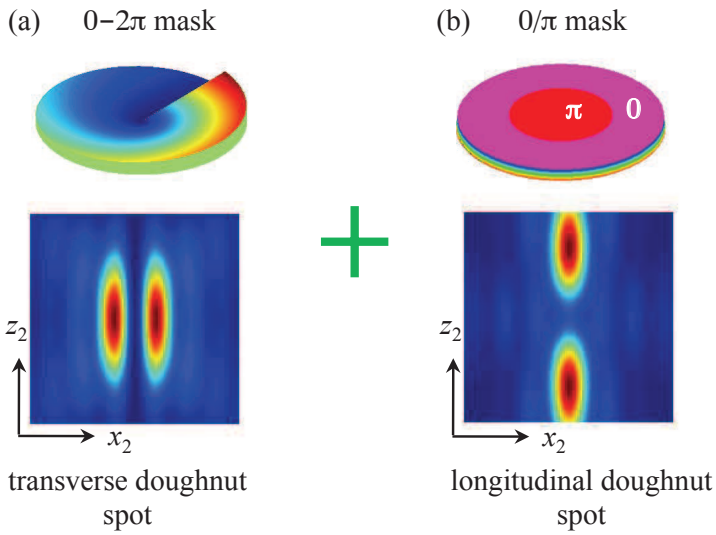

Figure 3.3: Generation of 3D doughnut shaped intensity distribution in the focal region of the OL by a combination of a vortex and a $0/\pi-$phase mask.

3.3 Generation of a 3D doughnut field distribution in the focal region

The radially polarized beam with a center-blocked profile (using an amplitude mask) has been studied in the last chapter. In this case, a long needle-like field with a longitudinal component is dominant. This means that the contribution of center part of the radially polarized beam is neglected. However, when considering the contribution of the center part only, a focusing spot with a doughnut shape can be obtained. Therefore, we propose to use this radial polarization combined to a mask to generate a 3D doughnut focusing spot. The geometry of lens focusing is shown in Figure 3.4. The incoming light is modulated by a well defined one-dark ring amplitude mask. The inner and outer radii of the dark ring are indicated as r_1 and r_2, respectively, and r_0 is the radius of objective aperture (Figure 3.4(a)). The ring is described by the factors $\varepsilon_1 = r_1/r_0$ and $\varepsilon_2 = r_2/r_0$. As shown in Figure 3.4(b), the side view of focusing system, due to the introduced dark-ring mask, only the light passing through the inner (Σ_1) and the outer part (Σ_2) of aperture contributes to the field distribution in the focal region.

The calculated intensity distribution of light rays from regions Σ_1, Σ_2 and the full aperture combined with dark ring are shown in Figure 3.5. The radially polarized

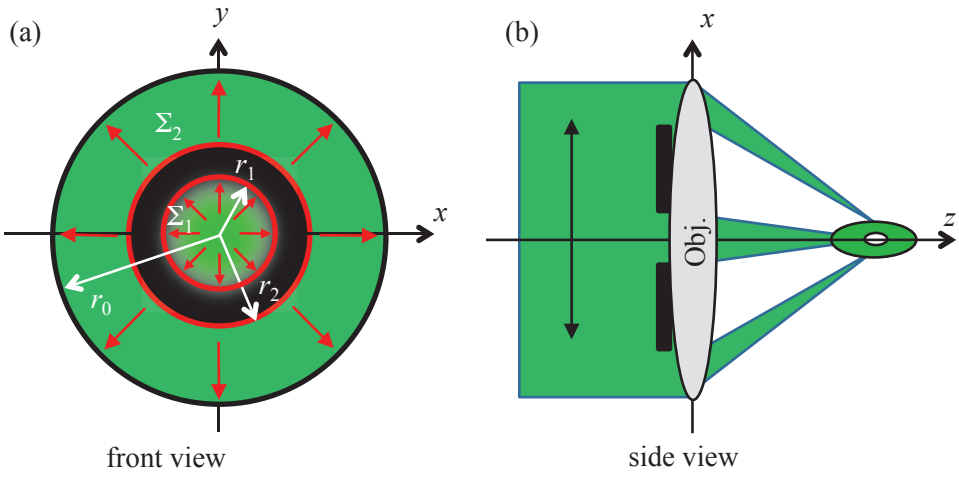

Figure 3.4: The schematics of a coded objective aperture for generating 3D doughnut intensity distribution in the focal region. (a) front view, (b) side view.

incident beam is tightly focused by an OL with NA = 1.4, $n = 1.515$. As shown in Figure 3.5($a_{1,2}$), when only the center part (Σ_1, $\varepsilon_1 = 0.5$) of the light beam is allowed to propagate through the objective aperture, the intensity distribution shows a doughnut shape in the focal region. As discussed in Chapter 2, it is due to the fact that, when the aperture is small ($r_1 = 0.5r_0$), the transversal components (E_{x_2}, E_{y_2}), which have doughnut shapes, are dominant in the focal region. The weak intensity in the center of doughnut spot is caused by the longitudinal component, which has an Airy spot-like shape. As shown in Figure 3.5($b_{1,2}$), the intensity distribution in the focal region induced from an annular aperture Σ_2 ($\varepsilon_2 = 0.97$), is quite different from the one induced from Σ_1. The EM field is mainly distributed along the optical axis, due to the dominating longitudinal component in the focal region. This behavior has been studied in detail in the Chapter 2. The intensity distribution induced from the dark-ring shaped aperture is presented in Figure 3.5($c_{1,2}$). It is clear that a doughnut focusing distribution along both transversal and longitudinal directions (c_2) is created. It can be explained by the coherent correlation of light rays from Σ_1 and Σ_2. The field distribution in the focal region is the interference of the light rays coming from the Σ_1 and Σ_2 regions. In fact, as compared to the strong transversal component from Σ_1, the transversal component from Σ_2 is negligible, hence, the transverse doughnut shape from area Σ_1 is not significantly changed along the optical axis (c_2). However, at the center of this transverse doughnut, due

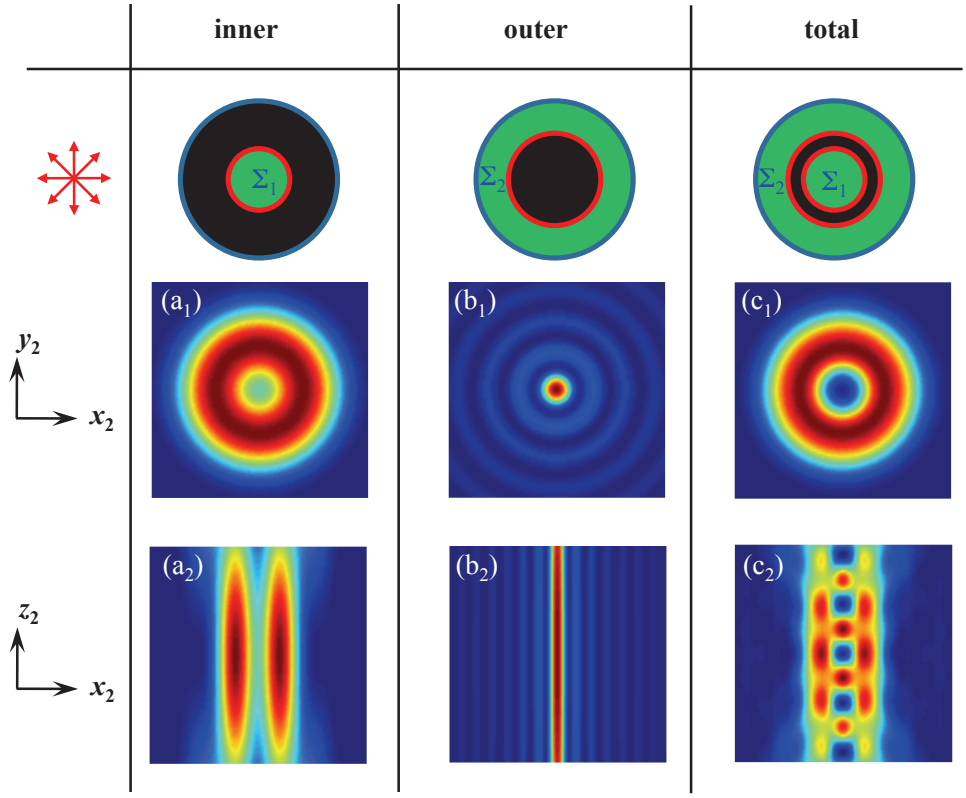

Figure 3.5: Calculated intensity distribution of the tightly focused radially polarized beam. [(a)-(c)] Intensity distribution of focusing spot of the light beams from the region Σ_1, Σ_2 and both Σ_1 and Σ_2, respectively. Subscripts 1, 2 indicate the intensity distribution at (x_2y_2) and $(x_2z_2)-$planes. $\varepsilon_1 = 0.5$, $\varepsilon_2 = 0.97$. $\lambda = 532$ nm, NA $= 1.4$, $n = 1.515$.

to the comparable intensity of the longitudinal components from Σ_1 and Σ_2, their interference induces a longitudinal doughnut along the optical axis. Thus, a 3D doughnut is formed in the focal region.

Figure 3.6 shows in more detail the intensity profiles of a 3D doughnut distribution at different intensity levels in the focal region. The intensity distribution is normalized at the peak intensity of the focusing spot. At the center of the focusing spot, the blue shell, which has only 10% of maximum intensity, has the perfectly isotropic shape, and its outer part, the green shell possesses a greater intensity (20%).

The intensity distributions of the focusing spot along the x_2-, y_2-, z_2-axes are shown in Figure 3.7. The graphs shown on the left are the field distributions of a tightly focused radially polarized beam in the absence of the one-dark ring amplitude

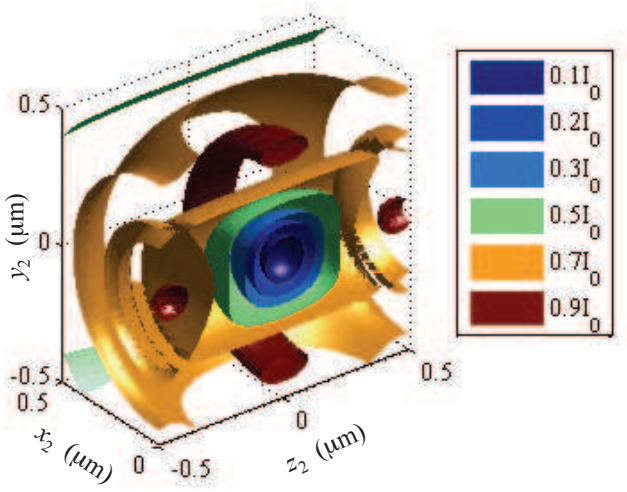

Figure 3.6: Isoploted Intensity profile of 3D doughnut focusing spot at different level intensity. The intensity distribution is normalized at the peak intensity of focusing spot.

mask. The transversal size of this Airy spot is 344 nm and the longitudinal one is around 758 nm. In the presence of a dark-ring amplitude mask ($\varepsilon_1 = 0.5, \varepsilon_2 = 0.97$) (Figure 3.7($a_2$-$c_2$)), the field distribution of the STED beam is converted to the doughnut shape and the dark spt possesses almost the same size ($\approx$ 400 nm) along all three axes.

As compared to the previous method, in which two light sources and two optical masks are required, the presented method for obtaining a 3D doughnut spot of the STED beam is very convenient. Only one light beam combined with one-dark ring is able to generate a 3D isotropic doughnut intensity distribution in the focal region. In practice, it will greatly simplify the optical microscope configuration.

This 3D doughnut focusing spot has many important applications, especially for 3D super-resolution microscopy. We have theoretically studied one of most important applications, 3D STED microscopy. The numerical calculation results of effective"PSF" size are shown in Figure 3.8. The parameters used in the numerical calculation are : $\lambda_{ex} = 532$ nm, $\lambda_{\mathrm{STED}} = 760$ nm. Light beams are tightly focused by a high NA OL (NA = 1.4, $n = 1.515$). In contrast to 2D STED microscopy, we shows clearly here that, when increasing the intensity of the STED beam, the effective "PSF" size is decreased along both transversal and longitudinal directions. At $I_{\mathrm{sat}}/I_{\mathrm{STED}} = 1/11$, the focusing spot has a perfect isotropic distribution and its

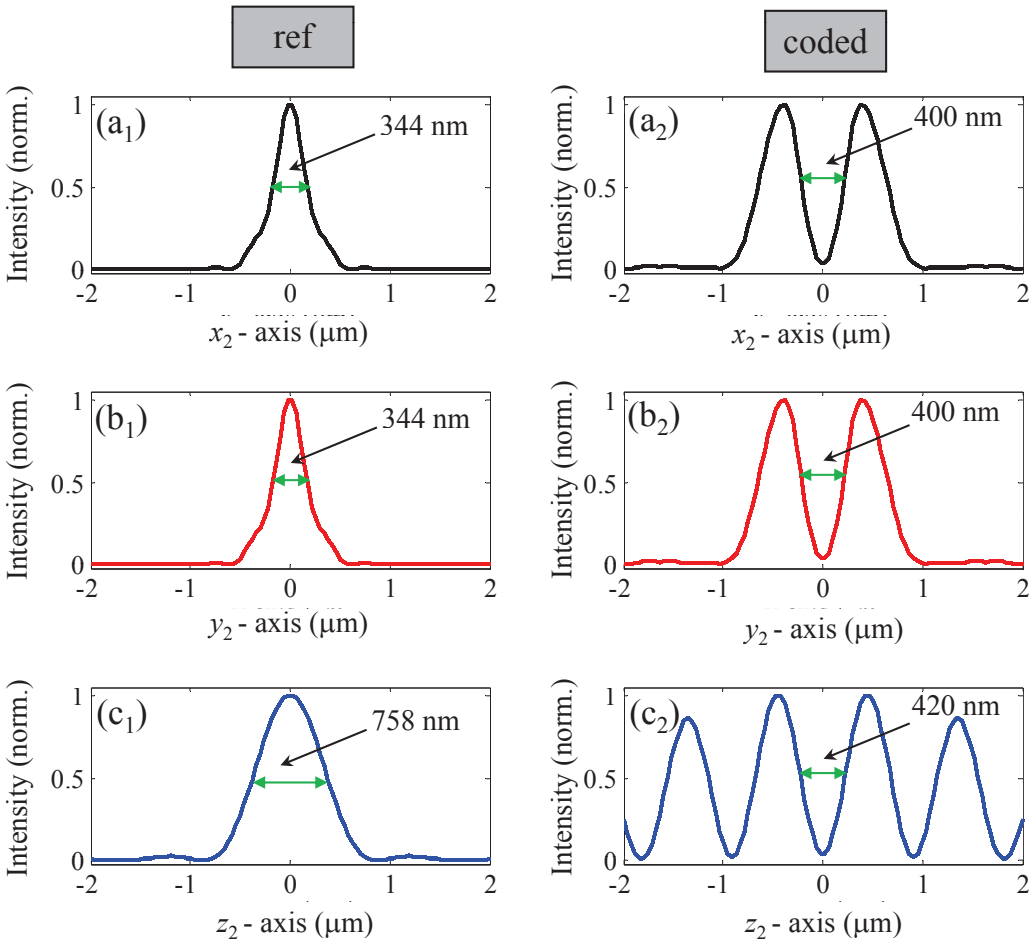

Figure 3.7: Intensity distribution of total intensity along x_2-, y_2-, z_2-axes. ref: intensity distribution of radially polarized beam focused by maskless OL. Size of the focusing spot is measured at FWHM of each peak intensity. The simulation parameters are taken same as those in the Figure 3.5.

size is only $\lambda_{ex}/10$.

As presented, the working principle of super-resolution STED microscopy is based on the switchable "on" and "off" states of the fluorescent molecule to achieve a super-resolution imaging. In practice, in the field of bio-imaging, by labeling the specimen with fluorescence dyes or quantum dots, the morphology of the object of interest can be obtained with a super high resolution [53]. However, in the field of optical lithography, instead of acquiring the emitted photons, the fabrication of structure is based on the polymerization or depolymerization properties of the photosensitive material. The photosensitive material is polymerized upon irradiated by a

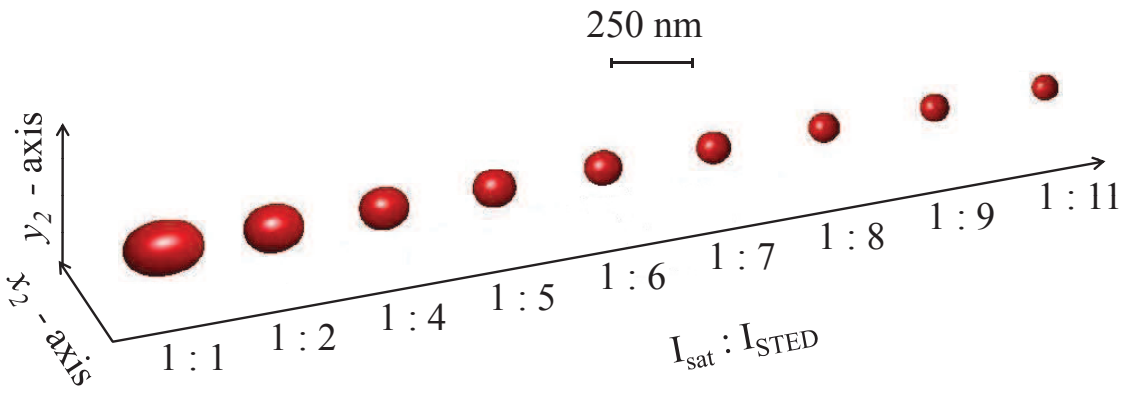

Figure 3.8: Variation of effective "PSF" size regarding the ratio of saturation intensity (I_{sat}) and STED beam intensity (I_{STED}).

proper light source. Hence, the STED microscopy cannot be an appropriate method for a super-resolution optical lithography, except if the material possesses "on" and "off" states [54]. In the next section, we will present a concept of "nano-pointer" for application of super-resolution optical lithography.

3.4 Nano-pointer for super-resolution fabrication

In recent years, it has been frequently reported that nano-structured devices have many fascinating functionalities, such as a negative refractive index from artificial metamaterials [55], control of light flow by photonic structures [56] (*i.e.*, photonic crystal, waveguide), as well as high capacity optical data storage [49]. Small nanoscale structures can be achieved by using electron-beam lithography. However, the experimental procedure is quite complex, and the experimental setup is expensive. Using optical microscopy to pattern a micro-structure in photo-sensitive materials is a less expensive and handy method. However, due to diffraction nature of light, the smallest feature size that can be fabricated is often restricted at a half of the wavelength of employed the light beam. Several optimistic methods have been to improve the fabrication resolution in optical lithography. Min Gu *et al.* fabricated a high capacity disk (up to 3.0 Tbytes) by using a radially polarized light beam and operated with a two-photon absorption mechanism [57]. Scott *et al.* reported the fabrication of a sub-diffraction structure (100 nm) by using the photoinitiation and photoinhibition properties of a photosensitive material [58]. Similar to STED

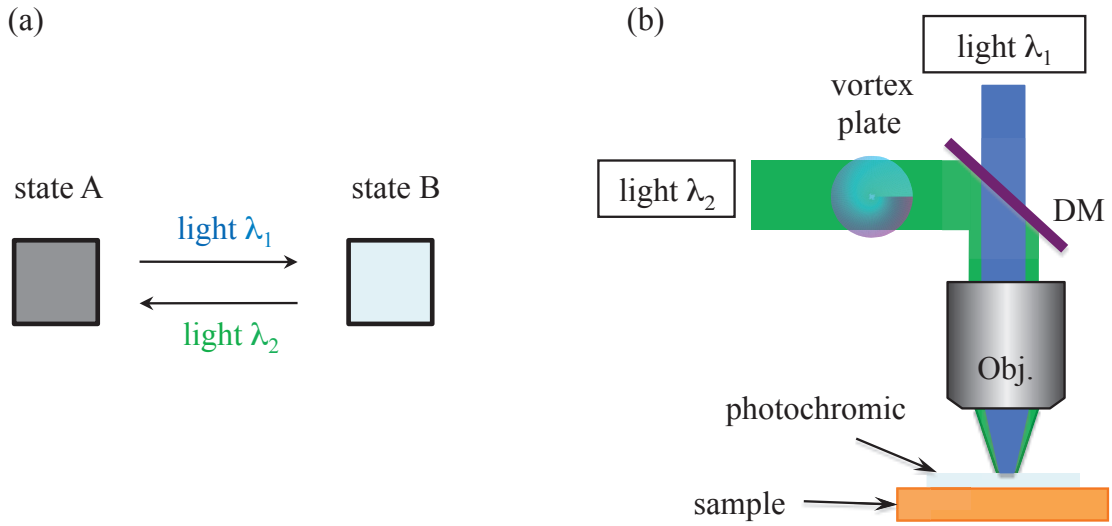

Figure 3.9: (a) Illustration of the transition of the absorption states of photochromic material. The photochromic material at state A, it possesses a strong absorption at λ_1 while at state B, it is transparent at λ_1. (b) Schematic drawing of the concept of AMOL for supper-resolution fabrication. A thin photochromic layer is deposited on the target sample. Beam 1 (λ_1), which possesses an Airy spot shape in focal region, is the writing beam. Beam 2, which induces a doughnut spot in the focal region, is the 'erasing' beam. DM: dichroic mirror.

microscopy, in this method, the writing beam is tightly focused into a photosensitive material and subsequently a second beam, which has doughnut shape distribution in the focal region, is introduced to inhibit the polymerization of the resist. Hence, because of the inhibition, the photosensitive material, which located in center of doughnut, is polymerized. This method was further improved by Min Gu *et al.* by using a highly photosensitive resin, which has fast curing speed [59].

Besides, the absorbance modulation optical lithography (AMOL) [13, 60, 61] is also a fascinating method for optical fabrication. This method is based on the optical properties of a photochromic material. As shown in Figure 3.9(a), the absorbance of the photochromic material has two states A , B. At state A, it shows a strong absorption to light λ_1 while at state B, it is almost transparent to light λ_1. When the photochromic material is illuminated by λ_1, the absorption of the photochromic layer converts from state A to state B. It will be converted back to its initial state A from B upon irradiation by a light λ_2.

The schematic drawing of AMOL is shown in Figure 3.9(b). It consists of two

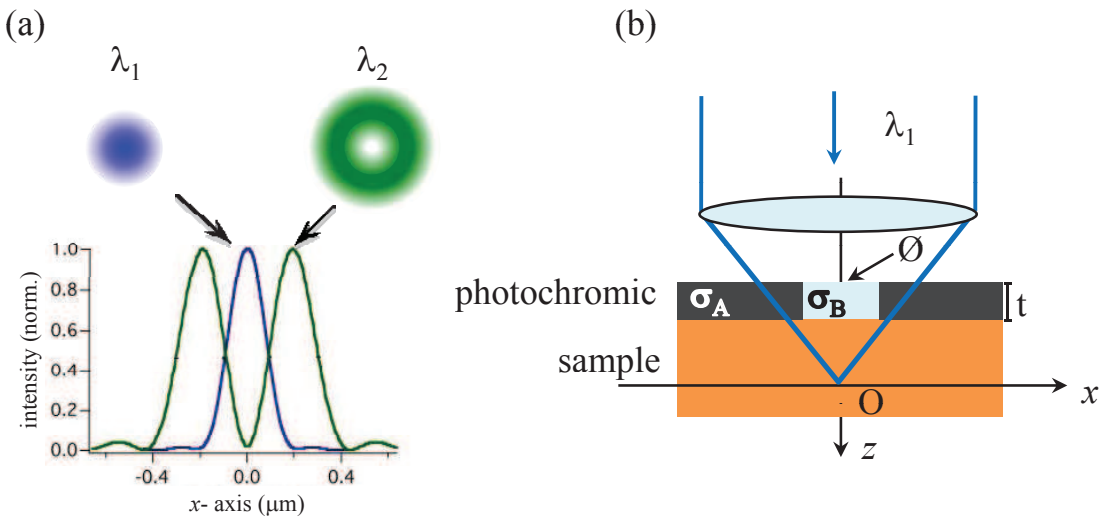

Figure 3.10: (a) Numerical calculation of intensity distributions along transversal direction in the focal region of light beam 1 (λ_1, blue curve) and light beam 2 (λ_2, green curve). (b) Propagation of light beam 1 (λ_1) through the photochromic layer. The absorbance of photochromic layer is modulated according to the doughnut focusing spot of light beam λ_2. σ_A, σ_B represent the absorption coefficients of state A, B at wavelength λ_1, respectively. t : thickness of photochromic layer. $\varnothing$: diameter of the area, where the photochromic layer is transparent ($\sigma_B \approx 0$) to the light beam 1 (λ_1).

light sources. One is the writing beam λ_1, which induces an Airy spot in the focal region (blue curve in Figure 3.10(a)). The other one is the "erasing" beam λ_2 , which has a doughnut shaped field distribution in the focal region (green curve in Figure 3.10(a)). A thin layer of photochromic material is deposited on the target sample (*i.e.*, photoresist).

The details of focal region are schematically illustrated in Figure 3.10(b). Due to the presence of a doughnut spot of a light beam at λ_2, the absorbance of the photochromic layer shows an inhomogeneous distribution in the focal region. The area, which is under λ_2 illumination, has a strong absorption to the writing beam λ_1, while the area located in the center of the doughnut beam is transparent to the writing beam λ_1. Due to this absorbing layer, the field distribution in the focal region is strongly modulated. The quantitative characterization of this focusing spot depends on several parameters: the diameter of doughnut size ($\varnothing$), the thickness of the photochromic layer (t), the absorption coefficient σ_A. Here, we assume that $\sigma_B = 0$.

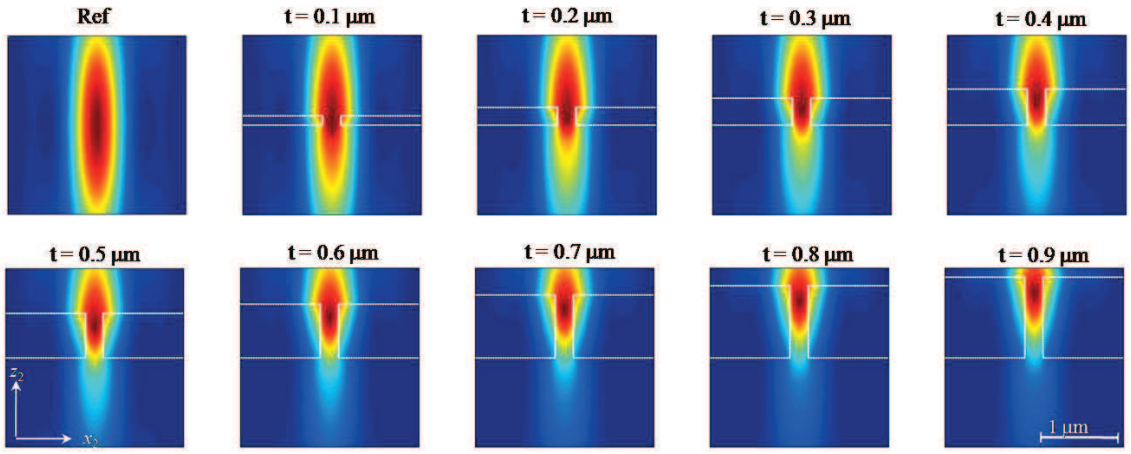

Figure 3.11: Calculated intensity distribution in the focal region as a function of the thickness (t) of photochromic layer. The simulation parameters are: NA = 0.6, $n = 1.0$, $\varnothing = 200$ nm, $\sigma_{\mathrm{A}} = 1 \times 10^6$ $[l/(\mathrm{mol} \cdot \mathrm{cm})]$.

To best of our knowledge, the vectorial Debye theory taking into account material absorption has not been studied yet. Here, we present for the first time numerical calculation results obtained by using a modified vectorial Debye theory. The detail of the derivation of the mathematical formula will be discussed in the Chapter 5. In this section, we mainly focus on the theoretical study of the influence of those parameters and we aim to generate a nanofocusing spot ("nano-pointer"), which has a small size and reasonable high intensity for a super-resolution optical fabrication application.

In numerical calculations, we assumed that there is no reflection occurring from the interface of the photochromic layer and the photoresist.

In the case of a low absorption, $\sigma_{\mathrm{A}} = 1 \times 10^6$ $[l/(\mathrm{mol} \cdot \mathrm{cm})]$, the intensity distribution in the focal region as a function of the thickness (t) of photochromic layer is shown in Figure 3.11. The interior area of white lines in the figures indicates the region, where the photochromic material at the state A. The notation 'Ref' represents the intensity distribution in the absence of any absorbing layer. The numerical calculation parameters are: NA = 0.6, $n = 1$, the diameter of doughnut spot $\varnothing = 200$ nm, $\lambda_1 = 532$ nm.

It is clear that, when increasing the thickness of the photochromic layer from 0 to 1 μm, the field distribution in the focal region is strongly modulated. The EM field attenuates dramatically along the optical axis and the transverse direction is

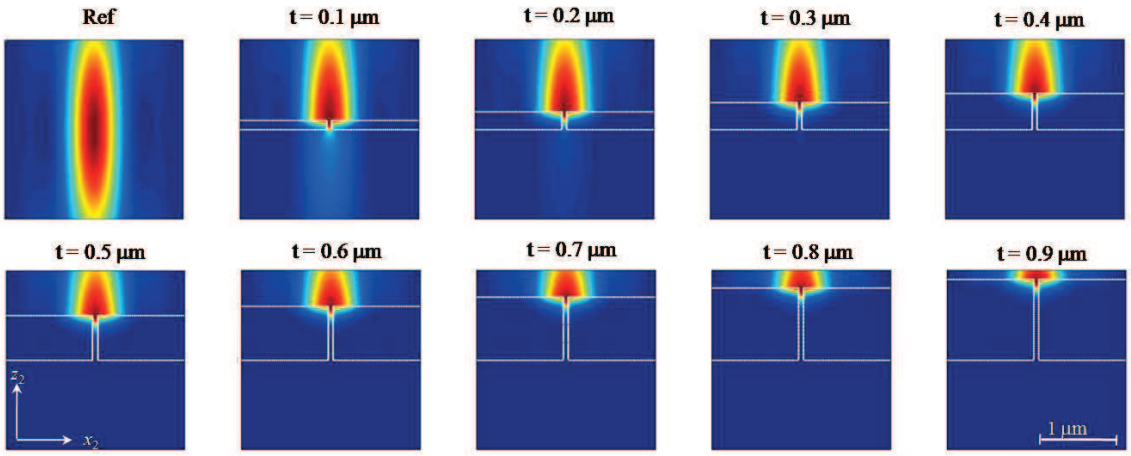

Figure 3.12: Calculated intensity distribution in the focal region as a function of the thickness (t) of photochromic layer. The simulation parameters are: NA = 0.6, $n = 1.0$, $\varnothing = 60$ nm, $\sigma_{\mathrm{A}} = 6.8 \times 10^6$ $[l/(\mathrm{mol} \cdot \mathrm{cm})]$.

also significantly reduced. However, because the absorption coefficient σ_{A} is not high enough, and with a broad doughnut spot ($\varnothing = 200$ nm), the confinement along the transversal direction is not enhanced very much. In an optimum case, the size of the focusing spot at the target sample position is around 230 nm (t = 0.9 μm).

Figure 3.12 shows the numerical calculation of the intensity distribution of the focusing spot with a high absorption (σ_{A} $(6.8 \times 10^6$ $[l/(\mathrm{mol} \cdot \mathrm{cm})])$ and a small doughnut size ($\varnothing = 60$ nm). It is clear that, when light arrives at the surface of the underlying target material, the focusing spot size is significantly reduced. However, as compared to the reference PSF, in the presence of an absorbing layer, the intensity of focusing spot is dramatically decreased. It is totally stopped by the photochromic layer when its thickness is larger than 0.5 μm. In the case of optical imaging and optical fabrication, the size of the focusing spot and its intensity are both particularly important. If the intensity of light is relatively small, *e.g.,* under the polymerization threshold of photoresist, the desired structure can not be realized.

With a highly absorbing layer (σ_{A} $(6.8 \times 10^6$ $[l/(\mathrm{mol} \cdot \mathrm{cm})])$, we have investigated the effect of the doughnut beam size, $\varnothing$, on the intensity distribution of focusing spot. The numerical calculation results are shown in Figure 3.13. The red bar indicates the calculated FWHM of the transverse size of focusing spot (measured at the surface of the sample). The blue bar indicates the peak intensity of the focusing spot, which is normalized to the reference case (no photochromic layer) (Ref PSF).

The studied doughnut spot size, ∅, ranges from 20 nm to 100 nm. It is clear that, when ∅ is less than 50 nm (Figure 3.13(a, b)), in a thick absorbing layer regime (t>0.5 μm), the focusing spot size is less than $\lambda/10$. However, in those ranges, the intensity is decreased to only 1% of the Ref PSF. Such a high energy loss is not be suitable for applications such as two-photon absorption polymerization. However, it may be a good tool for low one-photon absorption (LOPA) microscopy [62, 63], since this method does not require a high intensity excitation beam (see chapter 5). When ∅ is relatively large (Figure 3.13(e)), the focal size is no longer confined into the nanoscale (> 100 nm). The optimistic case for both focal size and intensity efficiency appears at Figure 3.13(c). It shows that, at a thickness t = 0.1μm (green dotted circle), the size of the focusing spot is only 87 nm and the focal intensity preserves more than 70% of total intensity. This "nano-pointer", which has small size and high intensity, can be used for many applications, such as super-resolution fabrication of photonic structure, nanodevices, etc.

Conclusion of chapter 3

In summary, in this chapter, we have presented the working principles of different 2D and 3D super-resolution optical microscopes, which are useful for optical imaging and optical fabrication applications. We have reviewed the 2D and 3D STED microscopy in detail. Furthermore, we proposed a new method for generation of a 3D doughnut focusing spot for the 3D STED microscopy. This method can greatly simplify the current complex 3D super-resolution microscope configuration, since only one light source, which is modulated by a one-dark ring amplitude mask, is able to generate a 3D doughnut focusing spot. Then, according to the optical properties of a photochromic material, we theoretically proposed a "nano-pointer " system, which allows to generate a focusing spot of 87 nm-size.

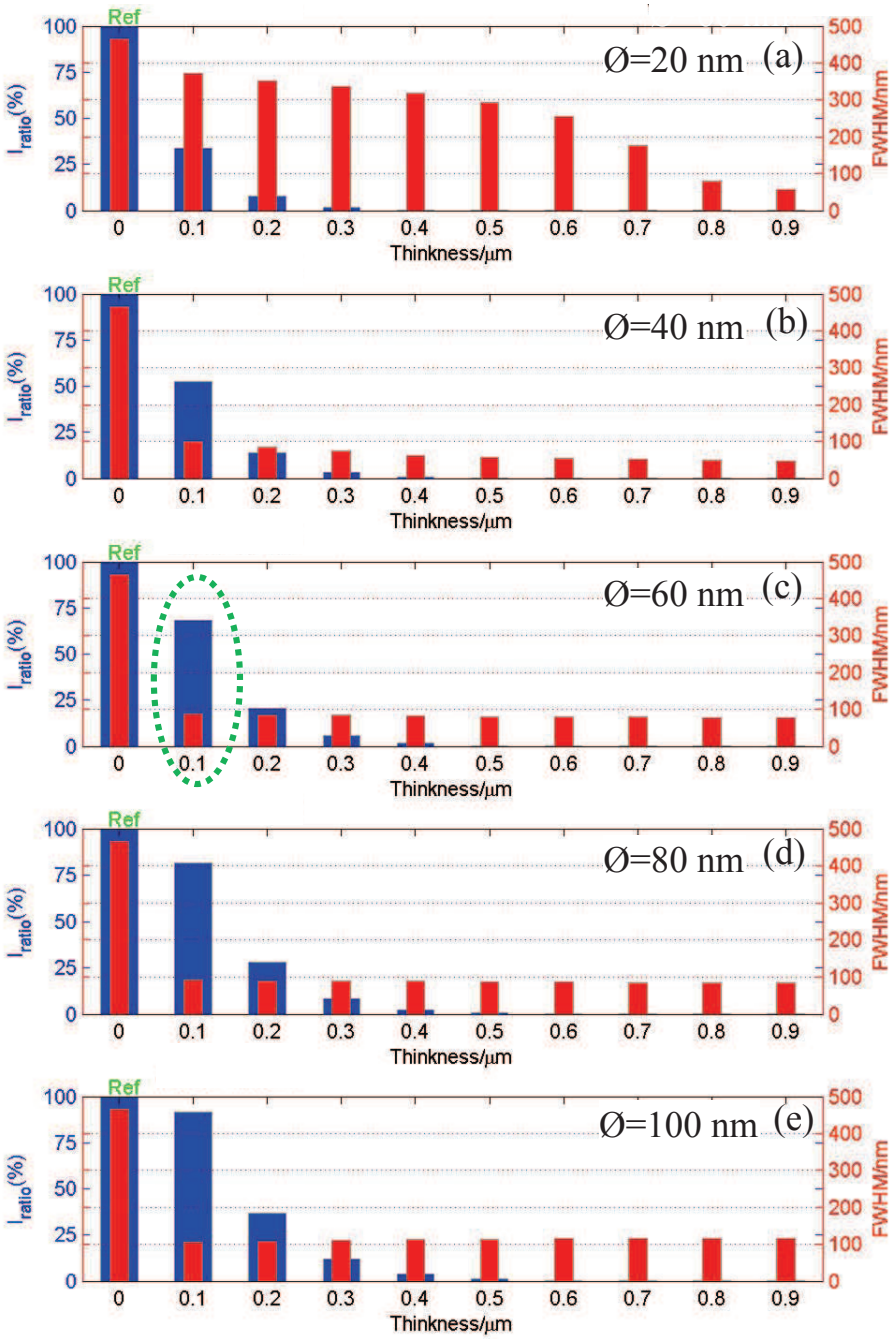

Figure 3.13: Calculated FWHM of transverse focusing spot size (blue bar) and the ratio (red bar) of peak intensity of nano-pointer and the peak intensity of reference beam as a function of film thickness and the size of STED beam (⌀). The numerical calculation parameters are taken same as those in the Figure 3.12. The blue dotted circled area is considered as a optimal result of nano-pointer, where the FWHM = 87 nm and it preserves 70% of total intensity of reference beam. The simulation parameters are: NA = 0.6, $n = 1.0$, $\sigma_{\mathrm{A}} = 6.8 \times 10^6$ $[l/(\mathrm{mol} \cdot \mathrm{cm})]$.

Chapter 4

Measurement of the PSF of high NA OLs

4.1 Introduction

In the past decades, thanks to the great improvement of optical characterization devices, such as interferometers, charge couple device (CCD), high accuracy translation stages and also with the assistance of fast computers for large data analysis, several fascinating experimental methods have been proposed to characterize the focusing behavior of the electromagnetic field distribution in the vicinity of the focal region. According to the different goals, different experimental methods are used. By using a CCD camera, Karman *et al.* [64] are the first ones who presented the direct measurement of the 3D intensity distribution of focusing spot of a low NA lens (NA < 0.01). The intensity distribution obtained under paraxial focusing condition shows a good agreement with the scalar diffraction theory. Wilson *et al.* and Török *et al.* successfully mapped the amplitude and phase distribution of point spread function by using the optical interferometer technique [65–67]. Introducing nanoparticles as probe beads to map and reconstruct the field distribution in the focal region from collected fluorescence light is a very handy method. Song *et al.* [68, 69] investigated the size effect of nanoparticles for PSF measurement. The studied NPs sizes are in the range of 100 nm to 1000 nm. Using the deconvolution method, they derived the PSF distribution. Brown *et al.* introduced further details of the experimental procedure for collecting and analyzing of PSF [70].

However, in all these methods, the influence of the vectorial properties of light has

not been detected, such as the asymmetric focusing behavior of a linearly polarized incoming light, doughnut shape distribution from an azimuthally polarized beam. As theoretically studied in Chapter 1, the reason is that, the effect of vector properties of light becomes significant only under tightly focusing conditions (NA > 0.7) [19]. In Karman's experiment [64], due to the employed NA of OL is less than 0.01, which is impossible to observe the influence of the vector property of light. In Song's case [68, 69], owing to the big size of the used bead (> 100 nm), it is impossible to distinguish a small difference in a tiny focal region. Nowadays, due to high resolution demand, or to perform a highly compressed energy flow of light, high NA OLs are often employed [1, 4, 11, 71, 72]. Hence, characterization of vector properties of light induced from a high NA OL become particularly important. But it is difficult to measure precisely a focusing spot at the sub-micrometer scale. In recent years, there are numerous attempts for observing the focusing behaviors of light beam under tight focusing condition. Using a tapered fiber probe [73] with a tip aperture diameter between 50 and 100 nm, it is possible to map the asymmetric EM distribution of a tightly focused beam with good spatial resolution. However, the probe tip displays unequal sensitivity to different components of the EM field, which might affect the reconstructed shape of focusing spot. The "Knife-edge" method [74] is considered as a fantastic method to quantitatively characterize the intensity distribution of a tightly focused beam. In this method, a photodiode, partially covered by a sharp edge alloy, transversely scans along the symmetric axis of the focusing spot. Light is diffracted by the sharp edge and is acquired by the photodiode, allowing to reconstruct the intensity distribution of the focusing spot. However, the "Knife edge" method is polarization sensitive [75] and the scanning direction should be realized along the symmetric axis of the focusing spot.

The goal of this chapter is to characterize the field distribution in the focal region of high NA OLs, by using a simple home-made high resolution confocal microscope and introducing a gold nanoparticle as a probe bead. We have investigated the general behavior of the lens system, such as the influence of NA, aberration effect and also the vectorial properties under tight focusing conditions. The chapter is organized as follows: experimental setup and sample preparation procedure are presented in the Section 2. The dependency of field distribution of the focal spot on the NA of OL is experimentally demonstrated in section 3. The degraded image quality caused from refractive index mismatch will be discussed in the Section 4.

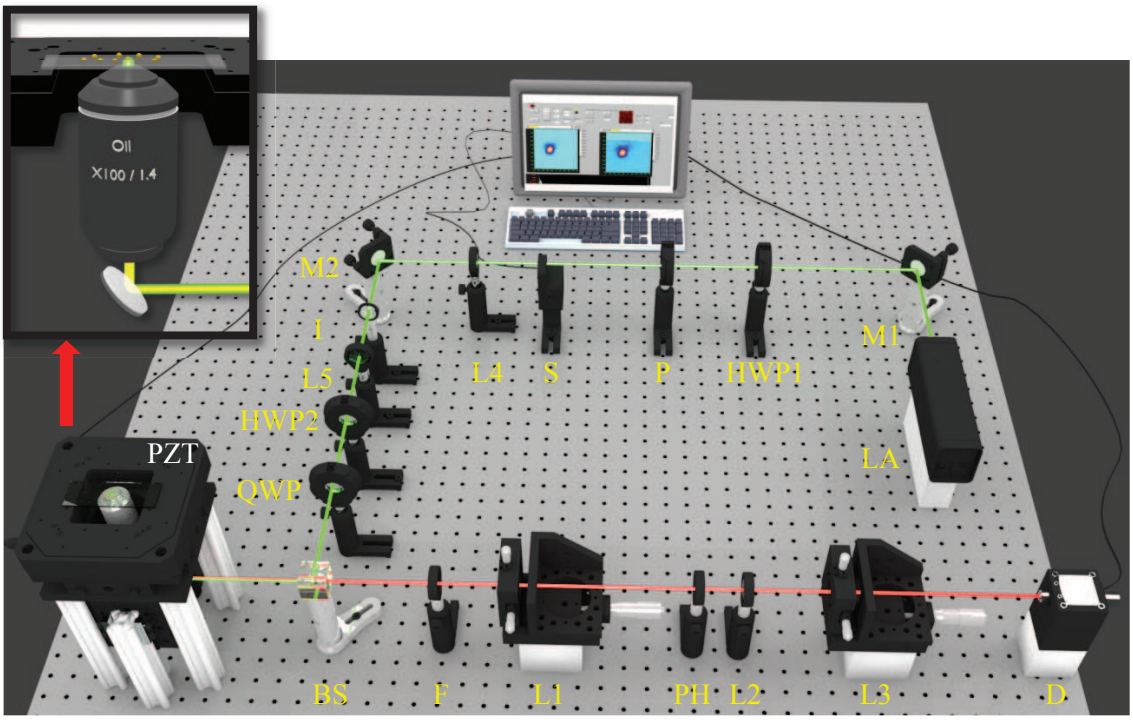

Figure 4.1: Schematic drawing of experimental setup used to realize optical imaging and fabrication. L1-L5: lenses; PZT: piezo translation stage; BS: beam splitter; F: 580 long-pass filter; PH: pinhole (100 μm) D: photodiode; HWP: half wave plate; QWP: quarter wave plate; I: iris; M1-M2: mirrors; S: shutter; P: polarizer; LA: laser source;

Under tight focusing condition, the pronounced effects of the vector properties of the incident beam on the focusing spot shape is demonstrated in the section 5 and the work of this chapter will be summarized in the last section.

4.2 Experimental setup and sample preparation

4.2.1 Laser scanning confocal microscope

Since its invention in 1957 [1, 76], the confocal microscope has being widely used in many fields, such as in life science [76], material science [77]. A standard laser scanning confocal microscope (LSCM) consists of three parts:

(*i*) an excitation source, for one-photon absorption LSCM, a monochromatic low cost continuous wave laser is often employed.

(*ii*) a high NA objective is used for focusing the light and also for collecting the reflection or fluorescence signals. In order to move the focusing spot inside the sample, a high accuracy translation stage is needed to drive the sample in three dimensions;

(*iii*) a confocal detection system, which consists of a highly sensitive detector (*i.e.*, photodiode) and a small pinhole (diameter < 100 μm), to eliminate the signal out of the focusing domain.

In order to experimentally demonstrate the focusing behavior of a tightly focused beam and to fabricate photonic structures (see Chapter 5), we have built a home-made confocal microscope. The schematic drawing of the LSCM is shown in Figure 4.1. The optical setup is installed on an optical isolation table to prevent from displacement caused from external environment.

The configuration of our setup is described as follows :

For the excitation part, a continuous laser (Oxxius) emitting at 532 nm is employed. Polariser (P) and a half-wave plate (HWP1) are employed to control the power of laser beam from 1 μW to 100 mW. Lenses L4 ($f = 150$ mm) and L5 ($f = 300$ mm) are introduced to enlarge the beam diameter and to ensure that the laser beam, which has an uniform intensity profile, is able to fully cover the objective aperture. The Iris (I) installed between L4 and L5 lenses are used to clean the laser beam profile. The polarization state of the excitation laser beam is controlled by introducing half-wave plate (HWP2) and/or a quarter-wave plate (QWP).

For the scanning section, a high accuracy positioning 3D piezo translation stage (100 μm $\times 100$ μm $\times 100$ μm) from Physik Instrumente (PI) is used to precisely drive the sample. In the experiment, we choose two kinds of OLs to perform a tightly focused field, the first one is an air OL (NA = 0.9), the other is an oil immersion OL (NA = 1.4, $n = 1.515$, CFI Plan Apochromat). Both OLs are able to tightly focus the incoming light and simultaneously to collect the signal emitted from the sample.

In the confocal detection block, the background noise induced from the incident light source, which is reflected or scattered from the substrate, is stopped by a 580 nm long-pass filter (F). The focal lenses L1 ($f = 100$ mm) and L2 ($f = 100$ mm) and a pinhole (PH) with a diameter size of 100 μm are employed to eliminate

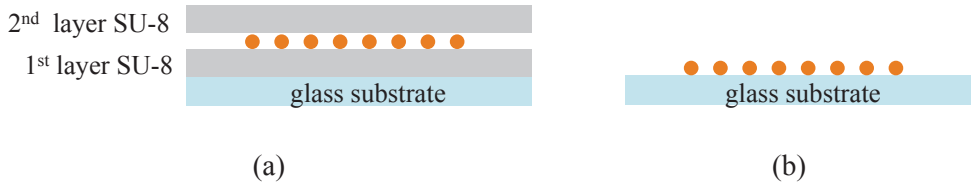

Figure 4.2: Illustration of two kinds of samples. (a) gold NPs are sandwiched between two SU-8 layers (for oil immersion OL). (b) gold NPs are directly deposited on glass substrate (for air immersion OL).

the noise coming from the out of focus region. Then, the signal is focused into a high sensitive silicon avalanche photodiode (D) by a focal lens (f = 50 mm).

The control of PZT and the reconstruction of the focusing spot from the acquired signal are carried out by a personal coded script written in Labview software.

4.2.2 Sample preparation

In our experiment, for the consideration of a "point-like" object, a small gold spherical nanoparticle with a diameter of 50 nm is used as a probe bead to realize the 3D mapping of the intensity distribution in the focusing region. In principle, the use of nanoparticle with a size smaller than 50 nm is good for serving as a "point like" source. However, in practice, very small nanoparticles are dim and bleach rapidly [68].

According to the different OLs used in this work, two kinds of samples are prepared:

(*i*) Sample preparation for oil immersion OL

As shown in Figure 4.2(a), to avoid possible aberrations caused by refractive index mismatch interfaces, gold particles are sandwiched between two SU-8 layers. The advantage of using SU-8 is that its refractive index is very close to the refractive index of the glass substrate. Besides, as compared to the fluorescence signal of gold NPs, the fluorescence emission of SU-8 is very weak, and can be considered as noise. The preparation of samples can be described as follows :

(a) SU-8 (2000.5) is spin-coated on a cleaned thin glass substrate (thickness = 125 μm). The coating parameters are: speed v = 2000 rpm, acceleration a = 300 rpm/s, coating time t = 30 s. A homogeneous thin SU-8 film with an approximate thickness of 500 nm is obtained. Then, the thin film is subse-

quently exposed in UV a box (1 min) to be fully polymerized.

(b) The aqueous solution containing gold NPs is dropped (single drop) on the thin film and spin-coated at a lower speed (v = 500 rpm) to ensure that a significant portion of single NPs stays on the SU-8 surface (SU-8 is relatively hydrophobic). The sample is then placed on a hot plate for 5 minutes at 100°C to remove the water solvent.

(c) Similar to the first step (a), a second SU-8 thin film is deposited on the top of gold NPs followed by a soft-bake and UV exposure steps. So that, gold NPs are well sandwiched between two solid SU-8 thin films.

(*ii*) Sample preparation for air-immersion OL

For the OL immersed in air, as compared to the previous case, the preparation procedure of sample is greatly simplified. Moreover, because the OL possesses a long working distance (WD = 2.1 mm), a glass substrate with thickness = 1 mm is used as sample holder. After removing the impurities from the surface of the thick substrate, an aqueous solution of gold NPs is spin-coated on it (Figure 4.2). Since gold NPs are "sandwiched" between glass and air, this sample will be used to study the refractive index mismatch problem (Section 4).

In order to avoid any impurity caused from external environment, the preparation of samples take place in a clean room environment. With these prepared samples, we have experimentally demonstrated many important behaviors of tightly focused beams.

4.3 Intensity distribution of focusing spot of different NA OLs

As theoretically studied in the Chapter 2, the focusing spot size is strongly affected by the NA of the used OL. Here, we propose a very convenient method to efficiently characterize the effect of NA of OL on the intensity distribution of the focusing spot.

In our experiment, we have employed only one OL (NA = 1.4, n = 1.515) with a large aperture diameter d = 1 cm. Then an iris, which has a flexible aperture, is introduced to modulate the incident beam size. Hence, due to the modulated beam size, the incoming light only partially covers the center part of the OL, and thus the

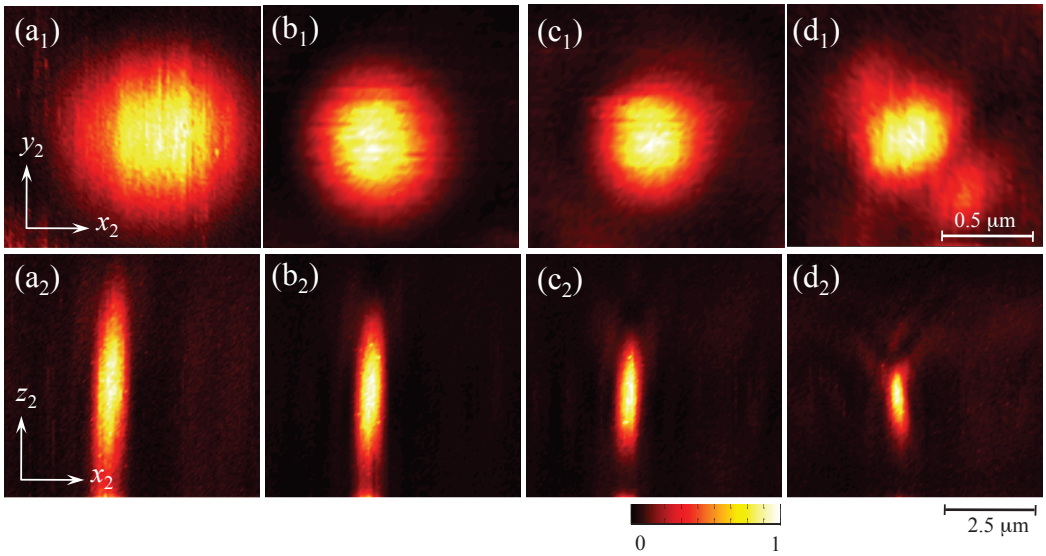

Figure 4.3: Variation of focusing spot size regarding the diameter of incident beam size. [(a)-(d)] Diameter of laser beam d: 5 mm, 6 mm, 8 mm, 10 mm, respectively. The diameter of objective aperture is 10 mm. Subscripts 1, 2 indicate the intensity distribution at $(x_2y_2)-$, $(x_2z_2)-$plane in the vicinity of focal point.

effective numerical aperture of OL (NA_{eff}) is controlled. The iris is introduced just in front of the BS to avoid the degradation of signal collecting, and the center of the iris aperture is perfectly aligned with the center of the OL aperture.

By changing iris aperture size, we have measured the intensity distribution of the focusing spot from different beams diameters, ranging from 0.5 cm to 1.0 cm with an increasing step of 0.1 cm. Form the incident beam diameter, we can calculate the effective NAs of the used OL, as shown in Table 4.1.

d (cm)	0.5	0.6	0.7	0.8	0.9	1.0
NA_{eff}	0.7	0.84	0.98	1.12	1.26	1.4

Table 4.1: The calculated effective NAs of OL corresponding to diameters (d) of incident laser beam.

Here, we focus on the characterization of the focusing behavior of OLs with high NAs (NA > 0.7), and thus we show only the results of the aperture with a minimum diameter d $= 0.5$ cm.

The experimental results obtained by a circularly polarized incident beam with

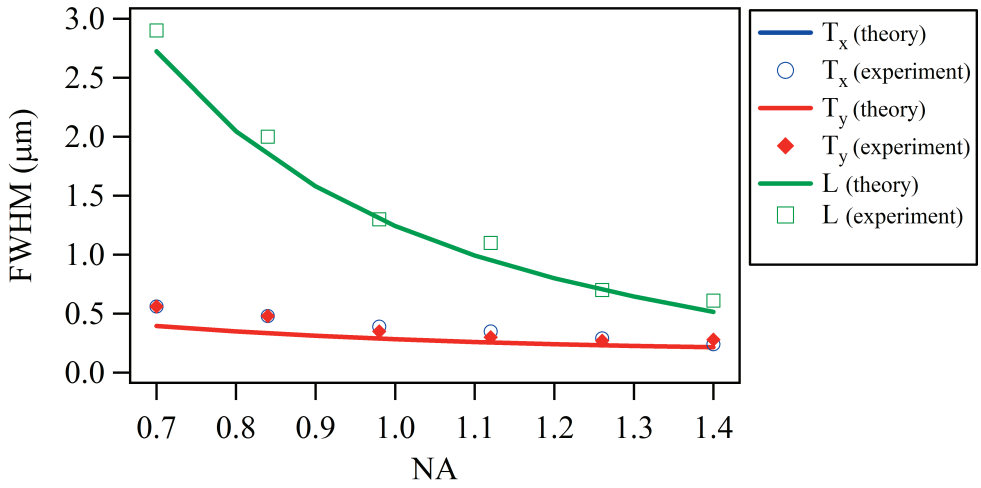

Figure 4.4: Comparison of the experimentally and theoretically obtained focusing spot size. L: longitudinal size of focusing spot; T_x, T_y: transverses size along x_2-, y_2-axes, respectively. Simulation parameters: $\lambda = 532$ nm, $n = 1.515$. circular polarized uniform beam.

different beam sizes are shown in Figure 4.3. It shows clearly that, at $(x_2y_2)-$plane, when NA_{eff} increases from 0.7 to 1.4, the focusing spot size decreases from 560 nm to 280 nm. At $(x_2z_2)-$plane, the longitudinal size of focusing spot is dramatically decreased when increasing the NA_{eff}.

The measured FWHM of the intensity distribution of the focusing spot along the transverse and longitudinal directions are shown in Figure 4.4. It is clear that the transverse size along x_2-axis (blue circle "○") and y_2-axis (red Diamond "♦") are almost same at for each NA_{eff}, and this size is decreased from 0.56 μm to 0.28 μm when NA_{eff} increases. This results is in good agreement with the behavior of a circularly polarized beam under tight focusing conditions (the blue and red line plotted in Figure 4.4). Similarly, the longitudinal size decreases from 3 μm to 0.71 μm, which evidently shows the strong dependency of the focusing spot size on NA of OL.

Thus, introducing an iris with a flexible aperture, it is very easy to investigate the influence of NA on the intensity distribution of the focusing spot. However, as shown in Figure 4.4, the experimentally derived curve is slightly different from theoretical results. It is due to the fact that under a tightly focusing condition, the image quality is often affected by many factors, such as imperfect beam profile, the confocal system and the aberration introduced from misaligned optical propagation.

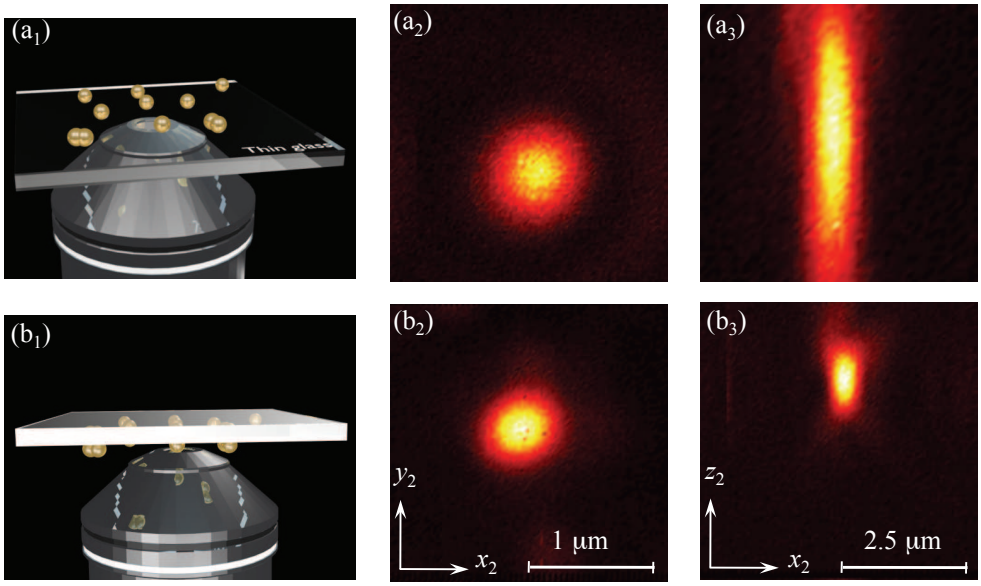

Figure 4.5: Experimental measurement of spherical aberration caused by refractive index mismatched interface. (a_1-b_1) Schematic diagrams of positioning of probe bead (Au NPs) above and bellow of thin glass substrate, respectively. [(a_2), (b_2)], [(a_3), (a_3)] are measured intensity distribution of focusing spot at $(x_2y_2)-$ and $(x_2z_2)-$planes. $\lambda = 532$ nm, NA $= 0.9$, $n = 1$.

In the next section, we will discuss about aberration, which is an usual problem met in many fields, such as life science, astronomy, etc.

4.4 Experimental observation of the intensity distribution of the tightly focused beam in the presence of refractive index mismatch

As theoretically studied in Chapter 1, in the presence of a refractive index mismatch, the quality of the focusing spot is critically degraded. In this section, in order to experimentally investigate the influence of this phenomenon, we employ an long working distance (WD = 2.1 mm) air-immersion OL (NA = 0.9) to study the field distribution in the presence of refractive index mismatch from air/glass interface. The sample preparation for this OL has been introduced in the previous section.

As schematically shown in Figure 4.5(a_1, b_1), there are two types of configura-

tions for sample positioning :

- **(*i*)** The upper one is designed for a refractive index mismatch case, in which the surface deposited with gold NPs is set-up. In this case, when light is focused through the glass air interface, the aberration occurs.

- **(*ii*)** The lower one (Figure 4.5 (b_1)) is designed for the case in which refractive index mismatch (reference) is absent The surface deposited with gold NPs is faced to the objective aperture. Due to the absence of dielectric interface in between the probe beads and the OL, there is no aberration effect.

The second configuration is not suitable for an oil immersion OL, since between gold and OL, AN oil medium has to be introduced. When the scanning process starts, gold NPs can not remain finely attached stably on the glass substrate due to the driving force from oil medium.

The intensity distribution of the focusing spot are shown in Figure 4.5 ($a_{2,3}$ and $b_{2,3}$). It shows clearly that the intensity distributions of the focusing spot with and without aberration are very different. At $(x_2y_2)-$plane, as compared to results derived from an homogeneous medium (Figure 4.5(b_2)), the focusing spot size is enlarged. At $(x_2z_2)-$plane, the longitudinal size is significantly increased, up to 3 times more than the one obtained from a homogeneous medium (Figure 4.5(b_3)). This observed large elongation behavior along the longitudinal direction is in good agreement with the theoretical prediction discussed in Chapter 1.

In optical systems, there are two categories of aberration [78, 79]. Here, the spherical aberration is caused from refractive index mismatched media and it belongs to the first category, in which the distorted wavefront distributes symmetrically around the optical axis. However, in practice, due to the misalignment or imperfectness of lens, the focusing quality is also degraded from the aberration, induced from a distorted wavefront that distributes asymmetrically around optical axis (second category), such as coma and astigmatism.

Figure 4.6(a) shows the intensity distribution at $(x_2z_2)-$plane in the focal region presenting coma aberration. This intensity distribution is derived under a purposely modulated beam propagation with an angle of 2° with respect to the optical axis. The experimental result shows a very good agreement with theoretical calculations.

In practice, aberrations induce low quality focusing spots resulting in blurred images in bio-imaging field and also in optical fabrication. To compensate this

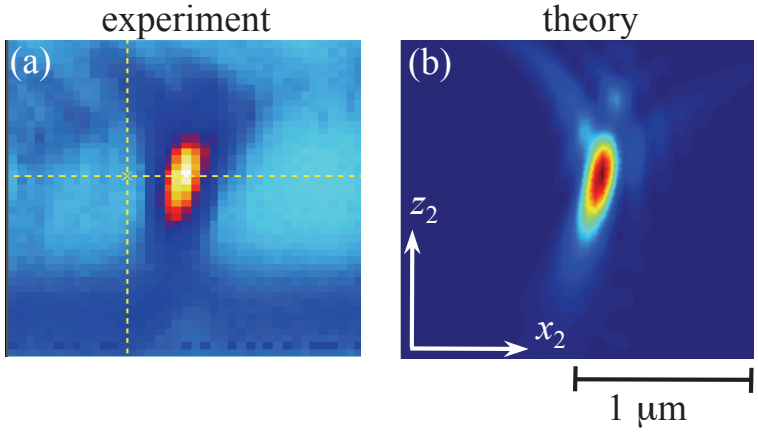

Figure 4.6: Experimental demonstration of aberration phenomenon caused from second category of aberration, Coma.

drawback, nowadays, in optical system, a wavefront sensor is often introduced to examine the wavefront. Besides, with the help of a deformable mirror, the wavefront deformation can be corrected and the quality of focusing spot is greatly enhanced.

In spite of this great optimization of the aberration effect, the field distribution in the focal region is also strongly affected by the vector properties of light (see Chapter 1). In the next section, we will experimentally study the influence of the incident beam polarization on the intensity distribution in the focal region.

4.5 Effects of incident beam polarization on the intensity distribution of a tightly focused spot

As discussed in Chapter 1, by using the vectorial Debye theory, under tight focusing condition (NA = 1.4), we have predicted the influence of the incident polarization on the formation of the field distribution in the focal region. However, in practice, quantitative characterization of focusing spot, which lies in sub-micrometer scale, is quite challenging. As compared to the previously mentioned complex methods [73–75], by using relatively small gold NPs and a high NA OL, in which the vector properties of light are significant, we are able to reconstruct the distinguishable field distribution of a tight focusing spot from different polarized incident beams.

In this section, we will firstly present the experimental measurement of a tightly

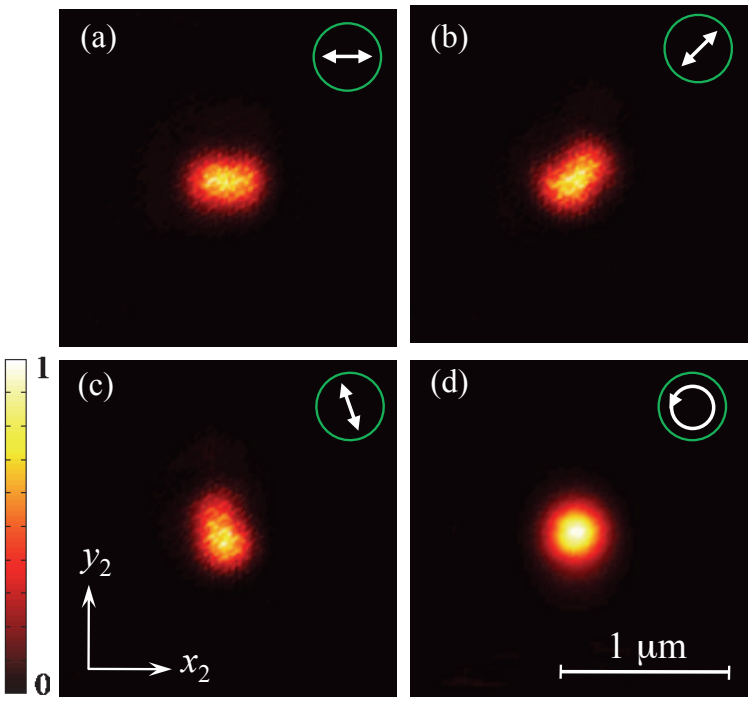

Figure 4.7: Experimental observation of the dependence of the focusing spot shape on the polarization of the incident beam. Input beam polarization (green circle) of each image: linear polarization at 0° (a), at 45° (b), at 110° (c), and circular polarization (d), respectively.

focusing spot from linear and circularly polarized light. In the second part of this section, we will discuss about the field distribution in the focal region obtained from radially and azimuthally polarized incident beams.

4.5.1 Measurement of a tight focusing spot from linearly and circularly polarized incident beams

As introduced earlier in this chapter, the experimental setup was shown in Figure 4.1. The control of the excitation beam polarization is realized by using phase plates (QWP, HWP2). Initially, the laser beam is linearly polarized along the x-axis. Its direction (linear polarization) is then controlled by rotating the half-wave plate (HWP2), as illustrated in Figure 4.1. To produce a circular polarization, a quarter-wave plate (QWP) is introduced behind the HWP2, the incident linear polarization (after HWP2) being oriented at 45° with respect to the neutral (fast or slow) axis

of the QWP. Depending on the aim of the work, either a HWP2 or both HWP2 and QWP plates can be used.

First, in absence of the QWP plate, we scanned laterally the focusing spot with a linearly polarized incident beam and measured the fluorescence image of a single gold nanoparticle. Figure 4.7(a) shows that the shape of focusing spot is elongated in the same direction as that of the input beam polarization (here along the x direction). By changing the polarization direction, we observed that the asymmetric distribution property changed accordingly. Figures 4.7(b) and 4.7(c) show fluorescence images of the same gold nanoparticle excited with a linear beam polarization at 45° and at 110°, respectively. The rotation of the focusing spot shape confirms that its asymmetric property is due to the polarization of input beam, which is consistent with the theoretical prediction presented in Chapter 1. Furthermore, by introducing the QWP plate with an appropriate orientation with respect to the direction of the linear polarization to result in a circular polarization, we obtained a fluorescence image with a perfectly symmetric focusing shape, as shown in Figure. 4.7(d). This results confirms also the theoretical prediction as shown in Figure. 1.17(a).

To quantitatively evaluate the shape and size of the focusing spot obtained with the linear and circular polarizations, we extracted the data from Figure. 4.7 for two orthogonal axes, according to the minimal and maximal sizes of the focusing spot. Figure 4.8 shows a comparison between theoretical and experimental results. In the case of a x-linear polarized incident beam (Figure.4.8(a)), the calculated full width half maximum (FWHM) of the total intensity distribution along the y-axis (FWHM = 240 nm) is only 70.5% of that along x-axis (FWHM = 340 nm). This ratio is in good agreement with the numerical calculation result (71.4%) shown in Figure. 4.8(b). In the case of a circular polarization, the focusing spot is symmetric and the spot has the same shape along both axes, as shown in Figure. 4.8(c), which is also in agreement with the theoretical curves shown in Figure. 4.8(d). Nevertheless, as compared to the theory, the experimentally measured focusing spot (FWHM=280 nm) is larger of about 40 nm for both axis and for both polarizations cases. This difference can be explained by the fact that, in practice, we have used a gold nanosphere as a probe bead with a diameter of 50 nm (it still cannot be an ideal point-like object). Thus, the experimental intensity profile is a convolution of an ideal (theoretical) focusing spot and the gold nanosphere size. Experimental data can be further optimized by applying the image deconvolution method [80] to

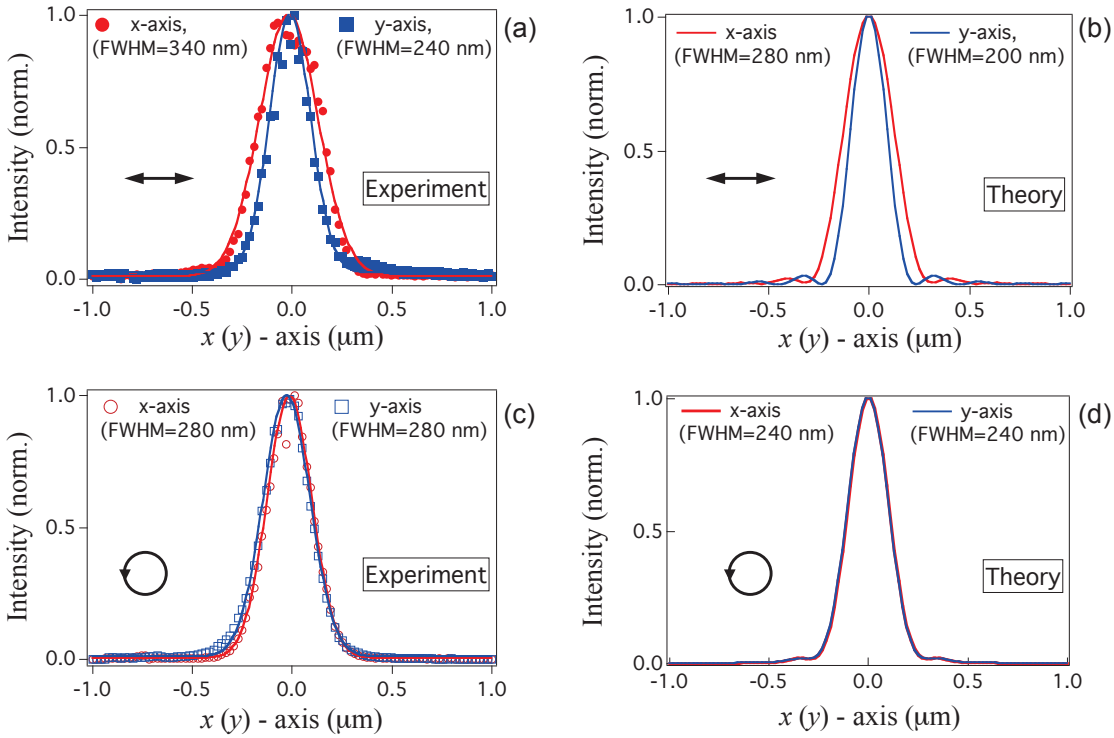

Figure 4.8: Comparison of experimental (a, c) and theoretical (b, d) results of the focusing spot profile, along the x_2-axis (red color) and y_2-axis (blue color) for linear (a, b) and circular (c, d) polarizations. The experimental curves are extracted from the images plotted in Figures 4.7 (a) and 4.7 (d). The theoretical curves are derived from Figures 1.15 (a) and 1.17(a) (Chapter 1). The size (FWHM) of the focusing spot, calculated along each axis, is indicated in each figure.

fit the theoretical calculation. However, it is not necessary in our case, since the polarization dependence of the focusing spot is clearly evidenced.

4.5.2 Measurement of focusing spot of radially and azimuthally polarized cylindrical vector beams

Experimental characterization of cylindrical vector beams becomes particularly important, in the context of their various potential. these polarizations offer interesting properties as theoretically discussed in Chapter 1, such as a longitudinal component dominating field, resulting in a doughnut focusing distribution in the focal region.

In this subsection, we present the measurement of the intensity distribution of the focusing spot induced from radially and azimuthally polarized input beams. Based

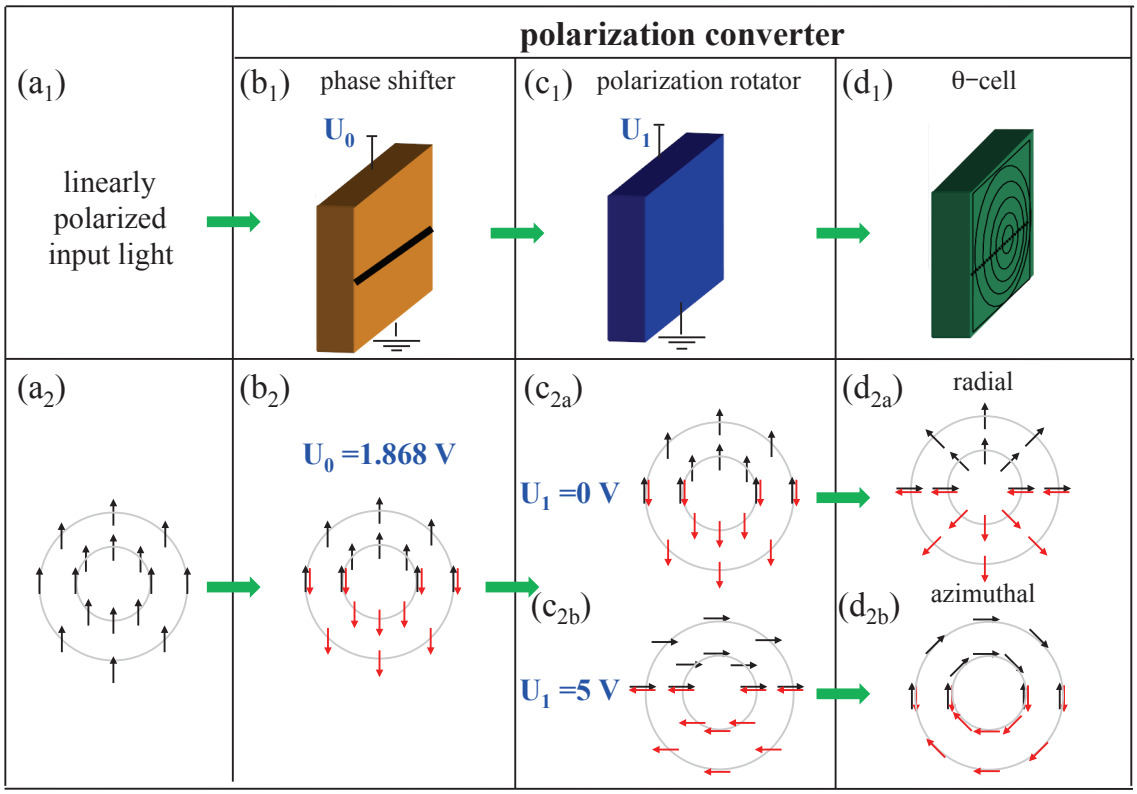

Figure 4.9: Illustration of the working principle of polarization converter.

on the previously described experimental setup (Figure 4.1), we transform the linear polarization to radial or azimuthal polarizations by replacing the quarter wave plate by a polarization converter (ARCoptix). The working principle of the polarisation converter is shown in Figure 4.9. The complete package of the polarization converter consists of a phase shifter (b_1) that allows to compensate the $\pi-$phase step between the upper and the lower halves of the laser beam, a polarization rotator (c_1) to rotate the input polarization by 90° and a $\theta-$cell (d_1), which is made of an array of small liquid crystal units with different orientations. As depicted in (b_2), the lower half of beam phase is $\pi-$phase retarded ($U_0 = 1.868$V for $\lambda = 532$ nm) with respect to the upper part of beam. If there is no applied voltage on the polarization rotator (c_1), the polarization of the laser beam keeps its initial direction (vertical) after exiting the polarization rotator. Then, the linear polarization (c_{2a}) is transformed to a radial polarization (d_{2a}) state after the light beam propagates through the $\theta-$cell. In the presence of a voltage $U_1 = 5$V, the extraordinary refractive index of the

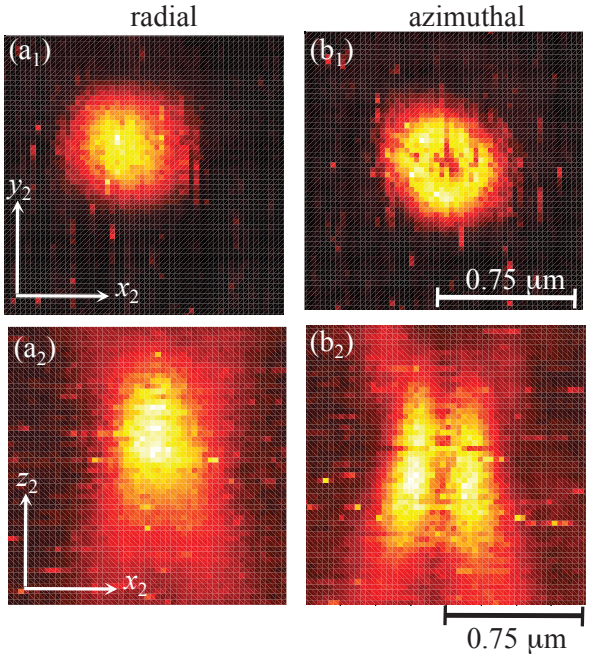

Figure 4.10: Experimental derived intensity distribution of different polarized incident beam: radial polarization (a), azimuthal polarization (b).

polarization rotator is changed and thus the laser beam polarization is converted to the horizontal direction (c_{2b}). At the end, with the modulation from $\theta-$cell, an azimuthal polarization (d_{2b}) is obtained.

The focusing spots formed from the radially and azimuthally polarized input beams are measured and shown in Figure 4.10. As compared to the previously discussed circular polarization case (Figure 4.7(d)), here, with a radially polarized incident beam, the transverse size of focusing spot is quite big (0.48 μm), which is in good agreement with the theoretical prediction (Figure 1.19(a_1)). At $(x_2z_2)-$plane, the longitudinal size is not elongated (size = 0.85 μm) but shows a broaden shape, with the same profile as predicted by the relevant theoretical calculation (Figure1.19(a_2)). As shown in Figure 4.10(b), in the case of an azimuthal polarization, at $(x_2y_2)-$plane (b_1), a clear doughnut distribution appears, and the FWHM of the dark hole size is only 0.14 μm. At $(x_2z_2)-$plane, a zero intensity appears all along the optical axis, in a good agreement with the theoretical prediction (Figure 1.21). As discussed in Chapter 2, the doughnut shape obtained from an azimuthally polarized beam is much smaller than that obtained from a right circularly polarized light modulated by a vortex mask. Hence, in practice, such a small doughnut shape has many

important applications, such as for STED microscopy, optical trapping, etc.

Conclusion of chapter 4

In conclusion, in this chapter, we have used a simple but effective experimental method to characterize numerous important properties of tightly focused light in the focal region. In our experiment, a home-made confocal microscope constituted by a high NA OL was employed to scan the fluorescence image of single gold NPs (probe bead) to reconstruct the intensity distribution of focusing spot. As compared to other reported methods, such as knife-edge method or fiber probe scanning method, this experimental method has a greatly simplified configuration and is able to very effectively characterize the focusing behavior of tightly focused beams. The study of the variation of field distribution with different NAs of OLs showed that, the transverse and longitudinal size of focusing spot decrease dramatically when increasing the NA of OL. This behavior is in good agreement with the theoretical prediction studied earlier in Chapter 1. Hence, employing a high NA OL to tightly focus the light beam into a sub-micrometer scale is a most common and effective way. Therefore, under a tight focusing condition, the field distribution is strongly influenced by the phase and polarization of light. The degradated quality of the focusing spot caused from spherical aberration and coma has been experimentally analyzed and it had a good agreement with theoretical calculation. Furthermore, we experimentally verified the influence of four kinds of incident beam polarizations (linear, circular, radial and azimuthal) on the intensity distribution of the tight focusing spot.

The generation of different polarizations of incident beam is realized by employing phase plates (HWP2, QWP) and a polarization converter. We have successfully measured the asymmetric distribution behavior of a linearly polarized incident beam, the symmetric focusing spot of a circularly polarized beam, focusing spot induced from a radially polarized beam and also the doughnut field distribution from an azimuthally polarized beam. Experimental results are in good agreement with numerical calculation results as derived from vectorial Debye theory.

The understanding of the intensity distribution behavior of the focusing spot of a high NA OL is of great important for applications. For instance, the low quality focusing caused from aberration, the unwanted asymmetric focusing shape,

can be presciently corrected, or thanks to its unique properties such as doughnut focusing spot, super-resolution methods can be implemented. Nevertheless, in practice, the focusing spot quality also depends on the studied material, for example, in bio-imaging. the scattering and absorption effects often influence the focusing properties. With respect to the experimental conditions, we will present in detail in the next chapter the absorption effect of the studied material on the intensity distribution of a tight focusing spot.

Chapter 5

LOPA microscopy for 3D imaging and fabrication

5.1 Introduction

In practice, in applications based optical microscopy, such as optical fabrication and bio-imaging, the studied material often displays absorption and scattering properties. Depending on the optical properties of the studied material and of the excitation light source, the field distribution near focal region can be modulated. In some domains, it is a drawback. For example, in conventional fluorescence imaging microscopy, the excitation light is attenuated along its propagation axis due to the strong absorption of the sample. In optical lithography, such as in the direct laser writing method, due to the low penetration depth caused from absorption, the fabricated structure is restricted to the surface of the substrate. Hence, considering the experimental condition, under tight focusing conditions, the effect of material properties on the intensity distribution of focusing spot is relatively important. However, to the best of our knowledge, the influence of material absorption on the intensity distribution and on the focused beam shape of a propagating optical wave has not been systematically investigated yet.

In this Chapter, based on the vectorial Debye theory proposed by Wolf [20], we further establish a new mathematics representation, in which the absorption effect of the material is taken into account when a light beam propagates through an absorbing medium. By using the new evaluation form of vectorial Debye theory, we quantitatively carry out the influence of absorption coefficient of the studied material

and the penetration depth of light beam on the formation of a tight focusing spot. Furthermore, we propose a new concept of optical microscopy, which is entitled "Low one-photon absorption microscopy" (LOPA) for 3D optical imaging and 3D optical fabrication. LOPA 3D microscopy concept is experimentally verified by using a simple experimental method. Since, LOPA microscopy is based on the one-photon absorption mechanism, as compared to the commonly used two-photon absorption microscopy, it has greatly simplified the optical configuration with reduced costs. By using this very handy 3D tool, we further study its application for 3D nano-fabrication.

The organization of this chapter is as follows: a novel form of the vector Debye theory considering of material absorption effects is presented in Section 2. The concept of 3D LOPA microscopy is proposed and experimentally verified in Section 3. The fabrication of 3D sub-micrometer structures by LOPA microscopy is presented in Section 4, and our findings of this chapter are summarized in the last Section.

5.2 Numerical calculation of the EM field distribution of a tight focused beam in an absorbing medium

As discussed in Chapter 1, the mathematical representation of the electromagnetic field distribution in the focal region of an OL has been proposed by Wolf in 1950s [20]. Thereafter, this representation has evolved to different forms in order to adapt itself to different experimental conditions, such as focusing of a light beam in refractive index mismatched media [34, 35], focusing of different polarized incident beams [24] or of different beam modes [27], focusing of a light beam through a mask [50], etc. However, the effect of material absorption is often neglected.

As depicted in Figure 5.1, the excitation light is focused into an absorbing medium, represented by the absorption coefficient σ, which varies as a function of the excitation wavelength. In this circumstance, the influence of absorption effects has to be taken into account when the diffracted light rays encounter a highly absorbing material after exiting the pupil of a OL. Based on the previously introduced vectorial Debye theory (Eq. (1.7) in Chapter 1), the formula representing the EM field distribution in the focal region using Cartesian coordinates (x_2, y_2, z_2) is

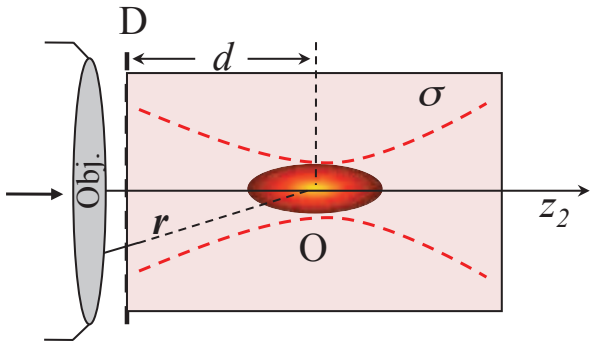

Figure 5.1: Schematic diagrams of propagating of tightly focused beam in absorbing medium. D is the interface between air (or oil) and absorbing material; d is the distance from the focal point of the OL and interface, D; O is the geometrical focal point. r is a distance from an arbitrary point at interface D and the focal point; z_2 is the optical axis of the OL; σ absorption coefficient of medium.

given by:

$$\mathbf{E}(x_2, y_2, z_2) = -\frac{i\mathrm{C}_0}{\lambda}\int_0^{\alpha}\int_0^{2\pi} \sin\theta \mathrm{A}(\theta,\varphi)\mathrm{B}(\theta,\varphi)\mathbf{P}(\theta,\varphi)\mathrm{A}_2(\theta,\varphi) \times \exp[ikn(z_2\cos\theta + x_2\sin\theta\cos\varphi + y_2\sin\theta\sin\varphi)]\mathrm{d}\theta\mathrm{d}\varphi, \quad (5.1)$$

where the novel added term $\mathrm{A}_2(\theta,\varphi)$ represents the contribution of the material absorption. According to the Beer-Lambert law [81], it can be expressed as $\mathrm{A}_2(\theta,\phi) = \exp(-\sigma \mathrm{Cr})$, where σ is the absorption coefficient of the material at excitation wavelength (λ), C is the molar concentration of the material, and r is the optical path of the diffracted light ray in the material, which is defined as the distance from an arbitrary point of the interface, D, to its corresponding image plane coordinate [63], as shown in Figure 5.1. In spherical coordinates, it is expressed as :

$$r = \sqrt{(\frac{d}{\cos\theta}\sin\theta\cos\varphi - x_2)^2 + (\frac{d}{\cos\theta}\sin\theta\sin\varphi - y_2)^2 + (d - z_2)^2}. \quad (5.2)$$

For simplicity, in Eq. (5.1), it is assumed that there is no refractive index mismatch problem arising at any interface, which may exist between the exit pupil of the OL and the focal plane.

According to this new mathematics representation, we choose two absorption coefficients, which represent a high absorption and a ultra-low absorption regime, to

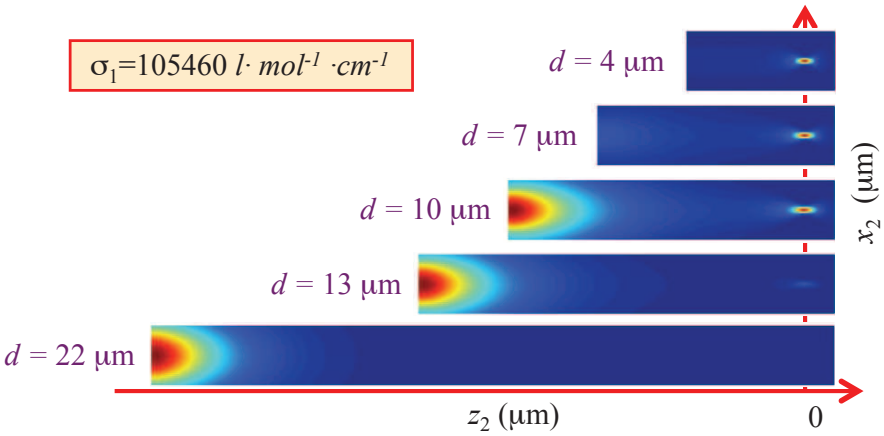

Figure 5.2: Effect of depth, d, on the propagation of tight focused beam in high absorbing medium. The simulation is realized with Rhodamine 6G (Rh6G) having $\sigma_1 = 105460\ l/(\text{mol} \cdot \text{cm})$ at $\lambda = 532$ nm, and NA $= 1.4$, $n = 1.515$.

numerically calculate the influence of absorption with different penetration depths (d) on the intensity distribution of a tightly focused beam in the focal region.

The numerical calculation results of the intensity distribution in a high absorption regime is shown in Figure 5.2. Here, the simulation parameters are: $\sigma = 105460\ l/(\text{mol} \cdot \text{cm})$, NA $= 1.4$, $n = 1.515$, the wavelength of incident beam is $\lambda = 532$ nm. The different penetration depths (d) are chosen as 4 μm, 7 μm, 10 μm, 13 μm, 22 μm. This figure shows clearly that, with a lower penetration depth (e.g. $d = 4$ μm), there is no critical modulation of the intensity distribution of focusing spot. It means that light can propagate into the focusing region and a tight focusing spot is obtained. However, when increasing the penetration depth, a significant portion of light is stopped at the surface and, in the focal region, the focusing spot intensity decreases dramatically. When d is up to 22 μm, light intensity totally vanishes in the focal region.

In contrast to a high absorbing material, at a ultra-low absorption range ($\sigma = 800\ l/(\text{mol} \cdot \text{cm})$), the incident beam is able to be tightly focused into the focal region without any significant distortion caused by the material, even with a long penetration depth of 22 μm, as shown in Figure 5.3.

The study of the material absorption effect on the formation of a tight focusing spot is very important for the quantitative characterization of the actual focusing spot distribution in the material or biological sample. In practice, the penetration

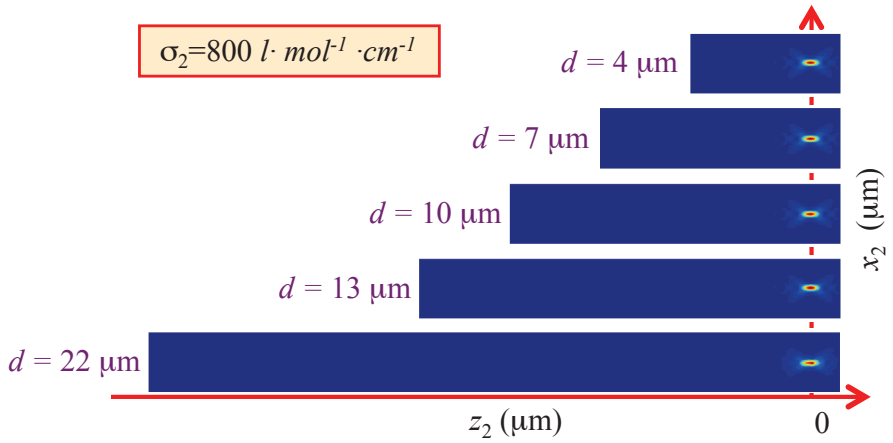

Figure 5.3: Effects of depth, d, on the propagating of tight focused beam in ultra low absorbing medium. $\sigma_2 = 800\ l/(\text{mol} \cdot \text{cm})$. $\lambda = 532$ nm. Rest of simulating parameters are taken same as in the Figure 5.2.

depth in optical microscopy is often reduced, due to absorption of the studied material. This critical drawback in 3D bio-imaging and 3D optical fabrication. The use of multi-photon absorption, such as two-photon or three-photon absorption microscopy, is a possible way to deal with a 3D goal, However, in order to induce two-photon absorption, a high intensity source, normally a picosecond or femtosecond pulsed laser is necessary, with high cost and high photo-damage to the sample. In the next section, we will present in detail of the concept of the low one-photon absorption (LOPA) microscopy.

5.3 Introduction of the concept of the LOPA microscope

5.3.1 2D and 3D optical microscopy

Basically, in optical microscope, the focusing spot size and penetration depth are the key factors to optimize the performances of an optical microscope. On one hand, optical microscope resolution has a crucial limitation due to the diffraction of excitation light. According to the Rayleigh criteria, the minimum resolving distance of two objects is defined as $0.61\lambda/\text{NA}$, where λ is the wavelength of incident light. To overcome this diffraction limit, several remarkable methods, in particular

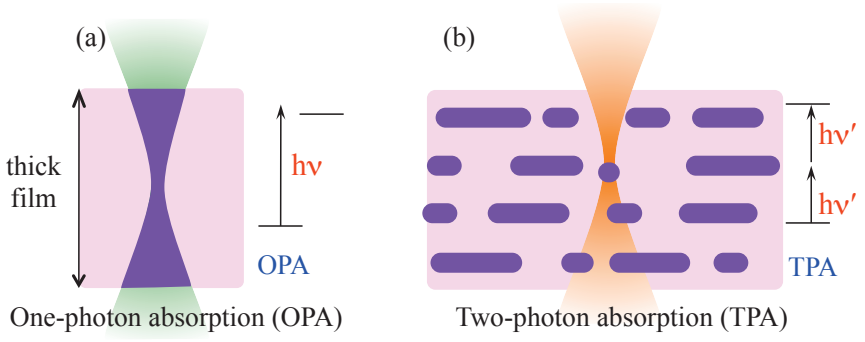

Figure 5.4: Illustration of absorption mechanism of of material : (a) one-photon absorption (OPA) and (b) two-photon absorption.

Stimulated emission depletion (STED) microscopy, have been demonstrated [2,82]. On the other hand, the penetration depth (or axial sectioning capability) of optical microscope strongly depends on the excitation mechanism, *i.e.*, depends on the light source employed in the optical system and on the material under study. Eventually, as shown in Figure 5.4, there are two categories of excitation methods, namely one-photon absorption (OPA) [1] and multi-photon absorption microscopies [83,84]. Normally, for thin film targets, OPA is a most appreciated method, because of its simplicity and high efficiency. Indeed, this method consists of using a low cost and continuous laser whose wavelength is centered in the high absorption wavelength range of the studied material. However, because of the strong absorption effect, light is dramatically attenuated from the input surface and OPA is not compatible with a deeper tissue penetration. This method is therefore impossible for thick film materials, or for 3D optical addressing. The TPA (or multi-photon absorption) technique (Figure 5.4 (b)) was then proposed, which presents a better axial resolution. In this case, two low energy photons are simultaneously absorbed, inducing an optical transition from the ground state to the excited state of the material, equivalent to the case of linear absorption (OPA). Because of the nonlinearity process, the TPA absorption rate is quadratically dependent on the excitation intensity [85], and happens with very high excitation intensity only. In practice, it can be done by using a pulsed laser, picosecond or femtosecond, that is furthermore focused into a submicrometer spot, where the intensity is a million times higher than that obtained out of the focus region. Hence, 3D imaging or fabrication can be achievable [11,83] with a high axial resolution. However, since this TPA requires a pulsed femtosecond or picosecond laser, it is rather expensive and complicated.

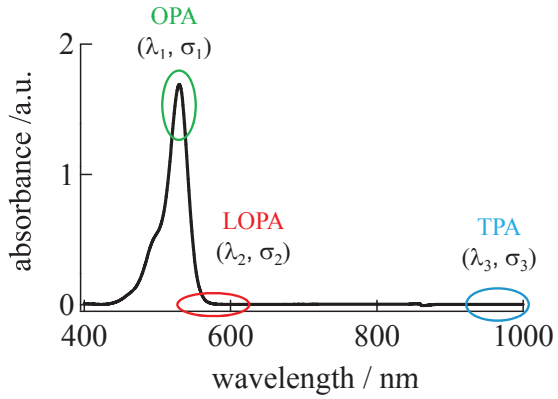

Figure 5.5: Experimental measured absorption spectrum of Rh6G. The green, red and skyblue colored circle represent the OPA, LOPA and TPA regions, respectively.

Wavelength (nm)	400	532	580	633	1064
K $[l/(\text{mol} \cdot \text{cm})]$	820	126090	480	240	0
I (mW/cm^2)	0.14	3.98	0.4	3.98	91.5

Table 5.1: The absorption coefficient (K) of Rh6G measured at different wavelengths, and the average intensity (I) of various excitation light sources, measured in front of the OL. The light source at 1064 nm is a pulsed nanosecond laser.

In contrast to OPA and TPA, LOPA microscopy combines the respective advantages of both OPA and TPA methods. The concept of LOPA is that, instead of employing a wavelength in a strong one-photon absorption regime, we propose to select a wavelength located in a low one-photon absorption range of studied material. Thanks to this low absorption, light can penetrate deeply inside the studied material, as TPA does. In principle, since the LOPA mechanism is still in the OPA category, a simple, continuous and low power laser is enough for LOPA microscopy. Furthermore, in order to obtain a highly resolved energy concentration of light in the focal region, a high NA OL is necessary. In the next subsection, the comparison of OPA, TPA and LOPA is discussed.

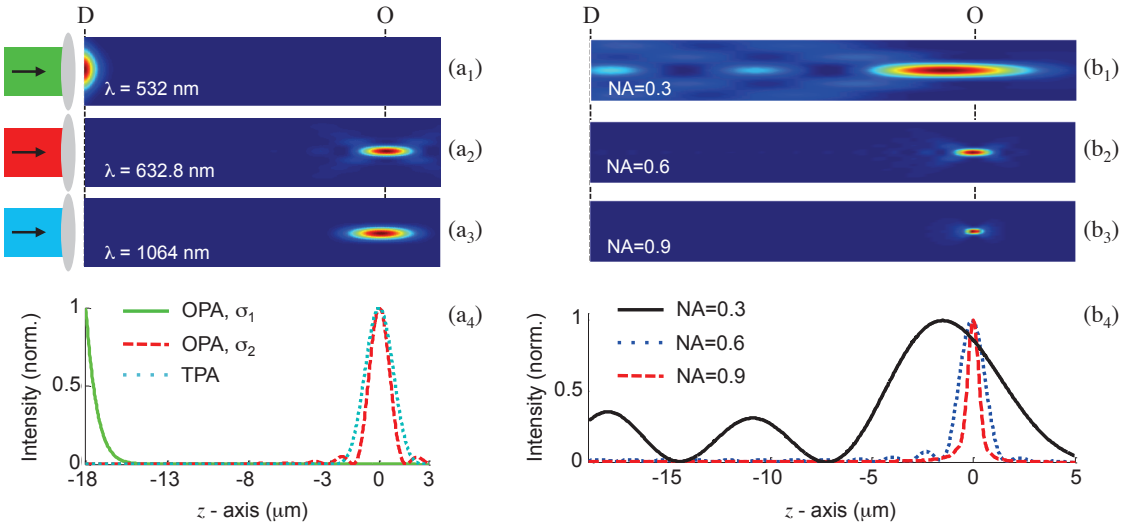

Figure 5.6: (a) numerical calculations of light propagation inside a Rhodamine 6G (Rh6G) solution, by using different wavelengths, 532 nm (a_1), 633 nm (a_2), 1064 nm (a_3), respectively. (a_4) intensity distributions along z-axis of light beams shown in (a_1)–(a_3), respectively. In this calculation: NA = 0.6, n = 1 (refractive index), and d = 18 μm. (b) propagation of light (λ = 633) inside a Rhodamine 6G (Rh6G) solution. (b_1) NA=0.3, (b_2) NA=0.6, (b_3) NA=0.9, respectively, d = 18 μm. (b_4) intensity distributions along z-axis of light beams shown in (b_1)–(b_3), respectively.

5.3.2 Comparison of OPA, TPA and LOPA

According to the experimentally measured absorption spectrum of Rhodamine 6G (Rh6G), shown in Figure 5.5, we choose three typical wavelengths to calculate the intensity distribution in the focal region, which represent three cases of interest : conventional OPA (532 nm), LOPA (633 nm) and TPA (1064 nm), respectively. The relevant absorption coefficients are shown in Table 5.1. The absorption interface (D) is arbitrarily assumed to be separated from the focal point O by a distance of 18 μm. As shown in Figure 5.6(a_1), because of the strong absorption of Rhodamine at 532 nm, the incoming light is totally attenuated at the interface D. This result explains why it is not possible to optically address 3D object with the conventional OPA method.

However, when using an excitation light source emitting at 1064 nm, *i. e.* in the blue circled region of Figure 5.5, the absorption coefficient is zero ($K_{1064\ nm} = 0$, excluding TPA coefficient). Light can penetrate deeply inside the material, resulting in a highly resolved 3D intensity distribution. Figure 5.6(a_3) shows the correspond-

ing numerical calculation result, which, in this case, was derived from the quadratic dependence of the EM field. The focusing spot size (full width at half maximum, FWHM) is quite large due to the use of a long wavelength. However, it is important to notice that, in practice, there exists a TPA intensity threshold above which two photons can be simultaneously absorbed. Therefore, by controlling the excitation light intensity, a small effective focal spot, below the diffraction limit, can be achieved with the TPA method.

We now consider the OPA case in which the linear absorption is very low (LOPA), as shown by the red circled area in Figure 5.5. At wavelength $\lambda = 633$ nm, the absorption coefficient is only 240 $l/(\text{mol} \cdot \text{cm})$, which is much smaller than that at 532 nm [126090 $l/(\text{mol} \cdot \text{cm})$], as shown in Table 5.1. Thanks to this very low linear absorption, simulation results show that light can penetrate deeply inside the absorbing material without significant attenuation. As shown in Figure 5.6(a_2), the light beam can be tightly confined at the focusing spot, which can then be moved freely inside the thick material, exactly as TPA does. Similar results have been also obtained with other excitation wavelengths, such as $\lambda = 400$ or 580 nm, with only a condition that their absorption coefficients should be very low, as indicated in Table 5.1. This LOPA presents a great advantage as compared with conventional OPA and TPA techniques. Furthermore, LOPA requires a shorter wavelength (400; 580; or 633 nm) as compared with TPA (1064 nm), the focusing spot size (FWHM) is therefore smaller. The diagram depicted in Figure 5.6(a_4) shows clearly the difference of the intensity distribution along the optical axis of three excitation mechanisms. We also note that there is no intensity threshold in the case of LOPA, because it is a linear absorption process. Therefore, LOPA requires a precise control of light dose in order to achieve high resolution optical addressing.

In order to make a clear difference of dose in LOPA case, it is demonstrated that the use of a high NA OL is a crucial condition. Figure 5.6(b) shows the intensity distribution of the focused beam, obtained with different OLs (with the same low absorption coefficient σ_2). It is clear that with an OL of low NA (NA = 0.3), the light beam is not strongly focused, which does not result in high contrast intensity distribution between the focal region and its surrounding. Therefore, the LOPA based microscopy using a low NA OL cannot be used for 3D optical addressing. However, in the case of tight focusing (NA = 0.6, 0.9), the light intensity at the focusing spot is a million time larger than that at out of focus, resulting in a highly

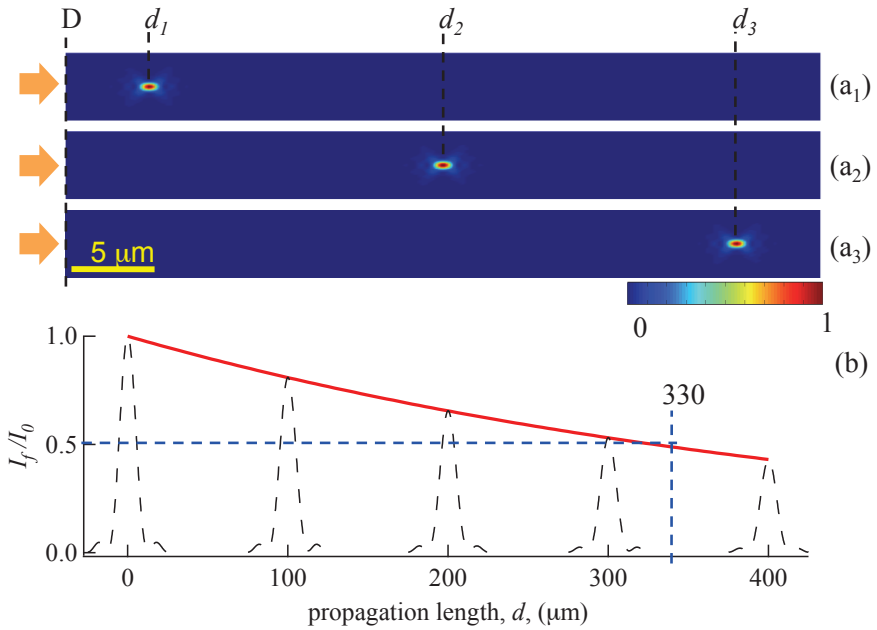

Figure 5.7: (a) Focusing the light into an ultralow absorption medium at different penetration depths: $d_1 = 5$ μm; $d_2 = 22.5$ μm; and $d_3 = 40$ μm. (b) Red curve: normalization of intensity (I_f/I_0) at the focusing spot as a function of the propagation length. I_f and I_0 are the intensities obtained with and without absorption medium, respectively. Dot curves: zoom on intensity profiles of the focusing spot along the optical axis, calculated at different d. The results are simulated with: $\sigma = 800$ [$l/(\text{mol} \cdot \text{cm})$]; $\lambda = 532$ nm; NA $= 1.4$ ($n = 1.515$).

resolved focusing spot [Figures. 5.6 (b$_2$,b$_3$)].

In summary, in order to realize LOPA based microscopy, two important conditions are required: i) ultra low absorption of the studied material at the chosen excitation wavelength, and ii) a high NA OL for tight focusing of the excitation light beam.

5.3.3 Characterization of the LOPA microscopy

The LOPA based microscopy is thus promising to realize 3D imaging and 3D fabrication, similarly to what could be realized by TPA microscopy. Indeed, by using the LOPA technique, fluorescence (for imaging) or photopolymerization (for fabrication) effects can be achieved efficiently within the focal spot volume only. By moving the focusing spot inside the material, as shown in Figure 5.7(a$_{1-3}$), we can realize 3D fluorescence imaging or fabrication of 3D structures.

Of course, absorption exists, even if the probability is very small. The penetration depth is therefore limited to a certain level. This effect exists also in the case of TPA, but it is more important for LOPA. Figure 5.7(b) represents the maximum intensity at the focusing spot as a function of the penetration length, d. For this calculation, we assumed an ultralow absorption coefficient, $\sigma = 800$ $[l/(\mathrm{mol} \cdot \mathrm{cm})]$, corresponding to the absorption of a negative photoresist SU-8 at $\lambda = 532$ nm [62]. We found that for a distance of 330 μm, the intensity decreases by a factor of two with respect to that obtained at the input of absorbing material (D interface). For many applications, this penetration depth of several hundreds micrometers is fully compatible with the working distance of microscope OL (about 200 μm for a conventional high NA OL), or with the scanning range of piezoelectric stage (typically, 100 μm for a high resolution).

For LOPA microscopy, we note that other weak effects exist, such as scattering, which also induces photons losses during light propagation inside a medium. However, these effects are negligible as compared with material absorption. Scattering effects, for example, are mainly considered in turbid media, by using a Monte Carlo simulation method [86] neglecting absorption.

In this section, we have theoretically studied the differences of the OPA, LOPA and TPA. We systematically characterize the detail of LOPA microscopy such as its penetration depth and the importance of using a NA OL. In the next section, we will use a simple method to experimentally verify the great advantages of the 3D LOPA microscope.

5.4 Experimental demonstration of the LOPA method

5.4.1 LOPA microscope with a coherent light source

The Rh6G dye molecules, which are commonly used to label protein in bio-imaging discipline [87], is homogeneously mixed in ethanol solution with a molar concentration of 1.43×10^{-4} mol/l. The absorption spectrum of the resulting solution is measured by a LAMBDA 950 UV/Vis/NIR Spectrometer and is shown in Figure 5.5. The absorption coefficients at different wavelengths are calculated using the Beer-Lambert law, and the corresponding results are shown in Table 5.1.

Figure 5.8 shows the 3D view of the experimental setup used to demonstrate the

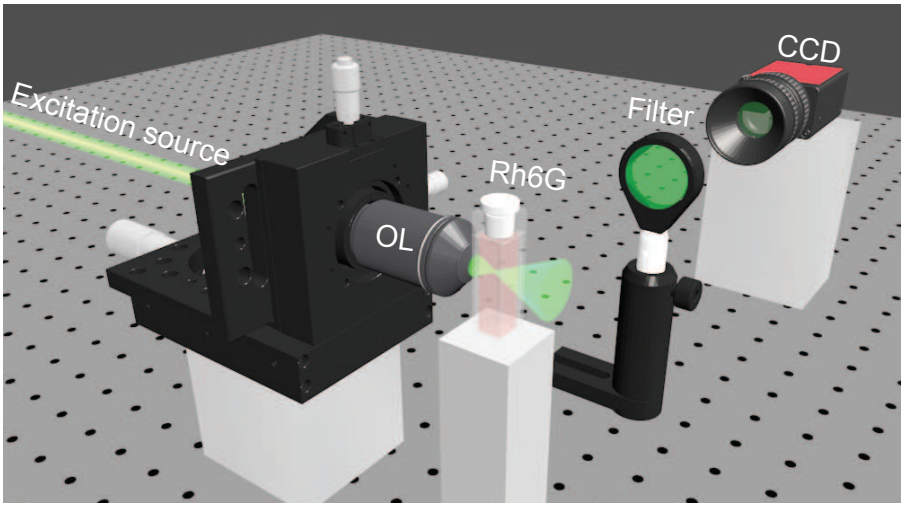

Figure 5.8: Experimental setup used to study the influence of material absorption on the light beam propagation. A long working distance OL (NA = 0.6), placed on a translation system, is used to focus a light beam coming from different light sources into a cuvette containing the Rh6G solution. A CCD camera combined with a band-pass filter allows to visualize along the z-axis the fluorescence signal of Rh6G, emitted from the region corresponding to the excitation beam propagation.

absorption effect and the concept of LOPA microscopy. A collimated light beam is focused, by a long working distance (WD) OL (NA = 0.6), into a cuvette containing the Rh6G solution. The OL is placed on a 3D translation stage that allows to move the focal spot freely inside the cuvette. A high sensitive CCD camera (Stingray F-125C 1/3'), connected to a computer, is placed laterally, with respect to the cuvette, to collect the fluorescence signal emitted from the excited area of the Rh6G solution. A band-pass filter is installed in front of the camera to filter out the scattering photons of excitation source. We note that a high OL with NA = 0.9 was also used for this experimental verification and it provided consistent results, but the WD of such OL is too short (< 1 mm) and it is difficult to show the effect.

To demonstrate experimentally the great interest of LOPA method, a continuous He-Ne laser emitting at 633 nm has been used to excite the Rh6G solution. In this case, the linear absorption exists everywhere along the propagation of the laser beam. However, due to the very low absorption efficiency, the effective number of photons which have been absorbed, and accordingly the emitted photons, is negligible at out of focusing region. In contrast, in the focal region, where the photons flux is huge, the effective number of absorbed photons become very important, resulting in a bright

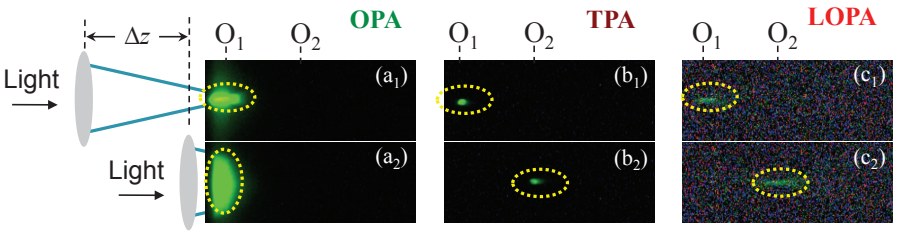

Figure 5.9: Fluorescence images of focused beams (see from side) obtained by focusing different excitation light sources: 532 nm (OPA); 1064 nm (TPA); and 633 nm (LOPA) into Rh6G solution. The focusing spot (OL: NA = 0.6, WD = 2.1 mm) is moved from the coming interface [O_1: (a_1), (b_1), (c_1)] to inside solution [O_2: (a_2), (b_2), (c_2)]. The fluorescence spots (corresponding to focusing spots) move at will inside the material in case of LOPA (633 nm) and TPA (1064 nm), while the excitation light is totally absorbed at near entrance in the case of OPA (532 nm).

fluorescence emission spot, as shown in Figure 5.9(c_1), 5.9(c_2). Since the absorption is very weak, the excitation spot or the fluorescence emission spot remains the same everywhere inside the cuvette, similar to the result obtained with TPA technique. The LOPA microscopy therefore allows to optically address 3D object as desired. The advantage of LOPA, as compared with TPA method, is that it requires only few milliwatts (2 mW in this work) from a simple and low cost continuous laser. It is worth to note that the fluorescence emission spot obtained by LOPA method [Figure 5.9(c)] is a little bit larger than that obtained by TPA [Figure 5.9(b)]. This can be explained by the fact that there exists a certain absorption threshold for TPA intensity, but not for LOPA. Figure 5.10 shows the intensity distribution along the z-axis of the focusing spot realized with λ_{LOPA} = 633 nm (Figure 5.10(a)) and λ_{TPA} = 1064 nm (Figure 5.10(b)), respectively. We assumed that the threshold of TPA is equal to $0.5I_{max}$, above which the fluorescence can be observed. However, because of no particular threshold in LOPA case, a low intensity (equivalent to an iso intensity of $0.2I_{max}$, for example) enables fluorescence emission, whose spot size is even larger than that obtained by TPA. Due to this drawback, a precise control of dosage is highly demanded when using LOPA method. Tight focusing by the use of an oil immersion OL demonstrated that the 3D resolution of LOPA is equivalent to that of TPA method [62].

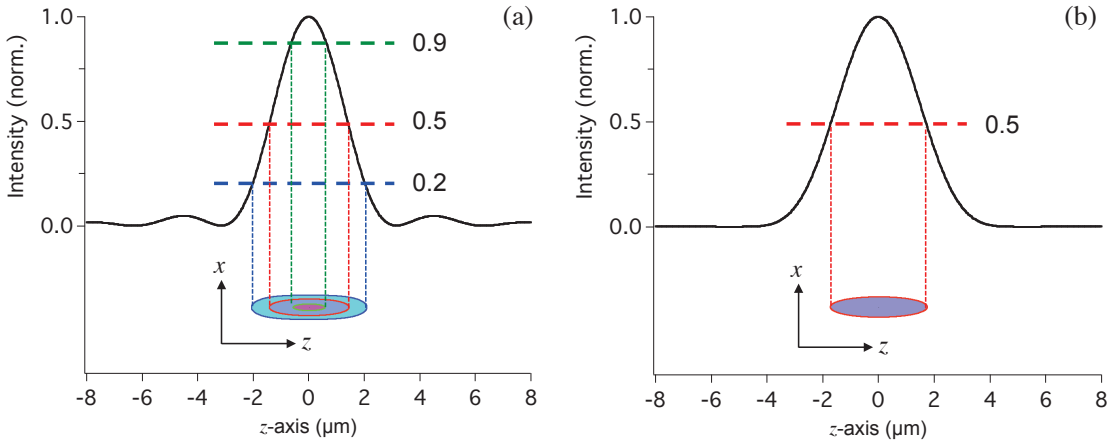

Figure 5.10: Numerical calculations of intensity distribution (top) along the longitudinal direction (z_2-axis) and contour plot (bottom) of the focusing spot in xz-plane. (a) LOPA regime, simulated with $\lambda_{\mathrm{LOPA}} = 633$ nm. Contour plots are calculated at different iso intensities: 0.2, 0.5, and 0.9, respectively. (b) TPA regime, simulated with $\lambda_{\mathrm{TPA}} = 1064$ nm. In this case, the side lobes disappear because of quadratic dependence of the intensity distribution. All simulations are done with NA = 0.6, and $n = 1$.

5.4.2 LOPA microscopy with incoherent light source

As mentioned above, the requirement of the LOPA method is a light source with low absorption effect when propagating inside the material. We have experimentally demonstrated that it is possible to use an incoherent light source (low power and continuous emission) to realize LOPA applications. In this experiment, we have used two band-pass filters to select two wavelengths, at 400 nm and 580 nm, of a white light source. These wavelengths are located in the ultra low absorption region of Rh6G material. The corresponding absorption coefficients and the light intensities are shown in Table 5.1. The emission patterns shown in Figure 5.11(a, b) are very similar to what obtained by a coherent excitation at $\lambda_{\mathrm{LOPA}} = 633$ nm. This result is very interesting for 3D imaging and 3D fabrication because of its simplicity and low cost. In particular, the use of a shorter wavelength (400 nm) allows to significantly reduce the focusing spot size, which is often limited by the diffraction.

Compared to the TPA method, LOPA based microscopy presents great advantages because of its very simple experimental setup employing a continuous laser or even an incoherent light operating at low power regime. The LOPA microscopy is not only for 3D imaging, but also for 3D optical fabrication. In the next section,

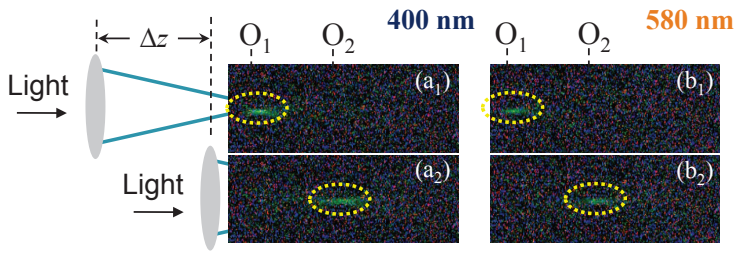

Figure 5.11: Fluorescence images of focused beams (see from side) obtained by focusing incoherent excitation light sources at low absorption regions: 400 nm (a), 580 nm (b), respectively, into Rh6G solution. The focusing spot (OL: NA = 0.6, WD (working distance) = 2.1 mm) is moved from the coming interface [O_1: (a_1), (b_1)] to inside solution [O_2: (a_2), (b_2)]. The fluorescence spots (corresponding to focusing spots) move as desired inside solution, similar to the results obtained by using a coherent excitation light shown in Figure 5.9.

fabrication of sub-micrometer will be presented.

5.5 Fabrication of sub-micrometer structure by LOPA microscope

5.5.1 Direct laser writing technique

In resent years, polymer based nano- or micro structures have been widely used in many fields, due to their inexpensive and fascinating functionalities [56, 88]. For manufacturing these structures, several experimental methods can be used, such as UV lithography [89], holography [90], direct laser writing (DLW) [62, 91], and electron-beam (e-beam) lithography [92], etc. Among of them, DLW is one of the most frequently used techniques, since it is easy accessible and is capable to pattern an arbitrary structure.

As schematically shown in Figure 5.12, a standard DLW technique consists of three parts: a focused laser beam, a photosensitive material (*e. g.* photoresist) and a nano-positioning 3D translation stage (PZT). The focused beam, which is obtained from high a NA OL, is used to locally expose the underlying photoresist. The "writing" process, either at the surface layer or deeply inside the sample, is realized by PZT, which is able to freely drive the photoresist in 3D respecting to the position of high intensity focusing spot. Then, according to the employed photoresist types

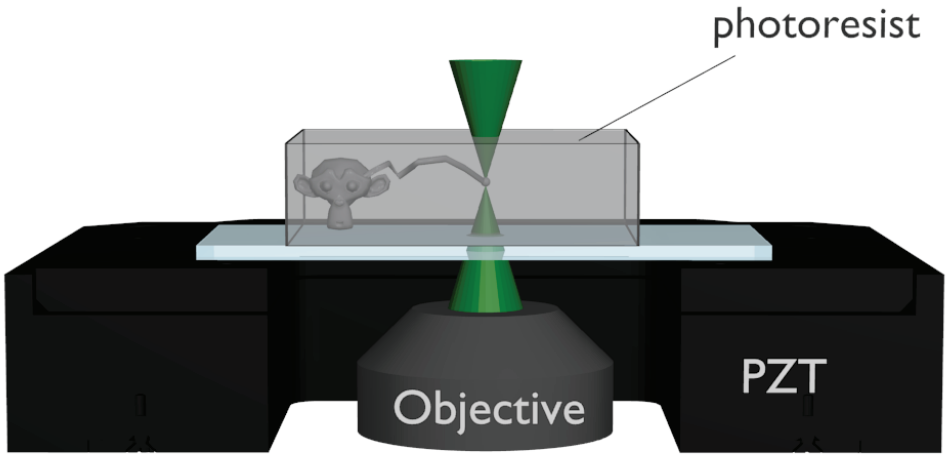

Figure 5.12: Schematic illustration of direct laser writing (DLW) technique. PZT: piezoelectric translation stage.

(negative or positive), developed in an appropriate solution, the written structure or its inverse form is obtained. It is due to the fact that, in writing process, the photoresist from the exposed area will be polymerized (negative) or depolymerized (positive), and thus in contrast to the unexposed region, in the relevant developer, the solubility of this area has a dramatic change.

Normally, for 1D, 2D desired structures, based on conventional OPA mechanism, a continuous laser source operating at a wavelength located within the high absorption band (in ultraviolet range) of thin film is employed as an excitation source. It can efficiently deal with arbitrary low dimensional structure, such as waveguide, fiber Bragg grating. For high spatial resolution 3D fabrication, fs− or ns−pulsed laser is employed as excitation source to induce high axial sectioning TPA polymerization voxel deep inside material. As discussed in last Section, since, the LOPA microscope, which possesses both advantages of conventional OPA and TPA, is a fantastic method for the fabrication of an arbitrary 3D sub-micrometer structures. In the next section, we will introduce the fabrication of 3D structure enabled by LOPA DLW technique.

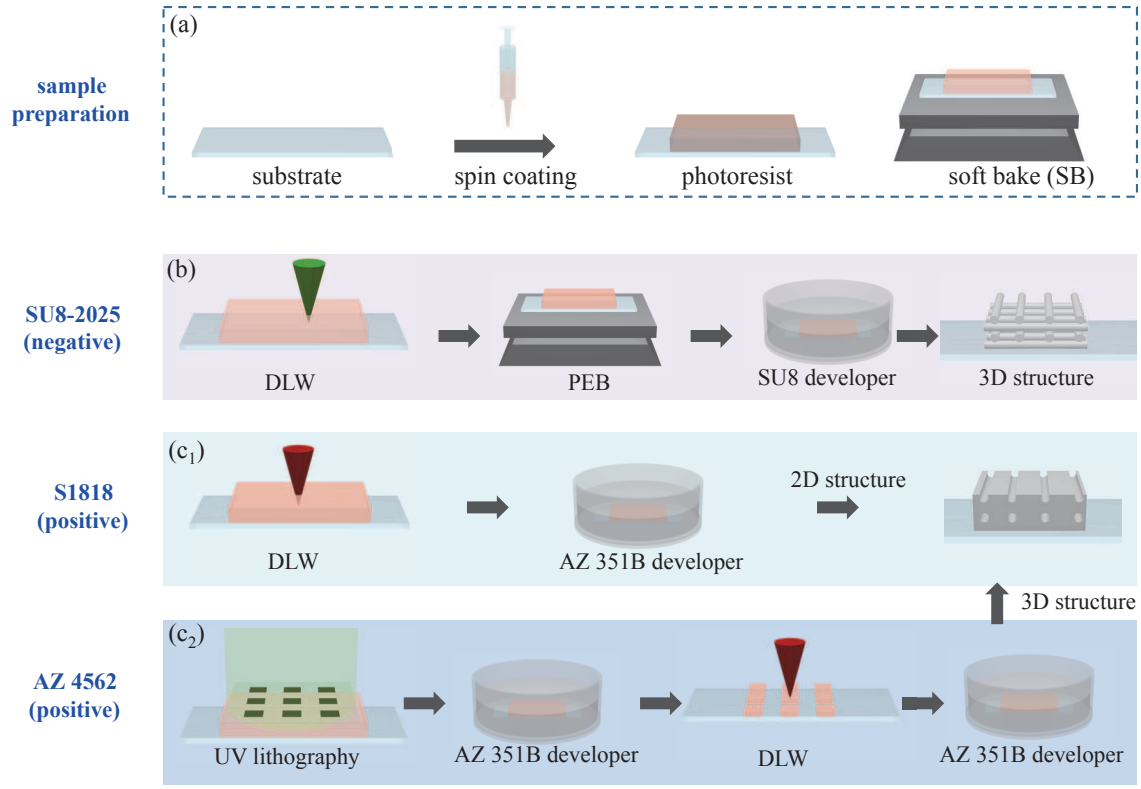

Figure 5.13: (a) Sample preparation procedure. [(b, c_1, c_2)] show the fabrication procedures of 2D and 3D sub-micrometer structures based on the photosensitive material SU-8, S1818, and AZ4562, respectively.

5.5.2 Sample preparation and fabrication procedure

We choose there kinds of photoresists to fabricate 2D and 3D sub-micrometer structures, which are SU8-2025 (negative) from Micro-Chem corporation, S1818 (positive) from Shipley Microposit, and AZ4562 (positive) from MicroChemicals.

5.5.2.1 Sample preparation

The sample preparation procedure is schematically shown in Figure 5.13 (a). A thin glass substrate (125 μm) is chosen as a host of photoresist after removing inorganic and organic impurities. Then, drops of photoresist are homogeneously deposited on the substrate via a spin coating machine. Subsequently, the glass substrate with deposited photoresist is soft baked on a hot plate to remove the resist solvent. According to the properties of photoresist and desired thickness, different coating procedures and parameters are applied. The preparation parameters of SU-8, S1818

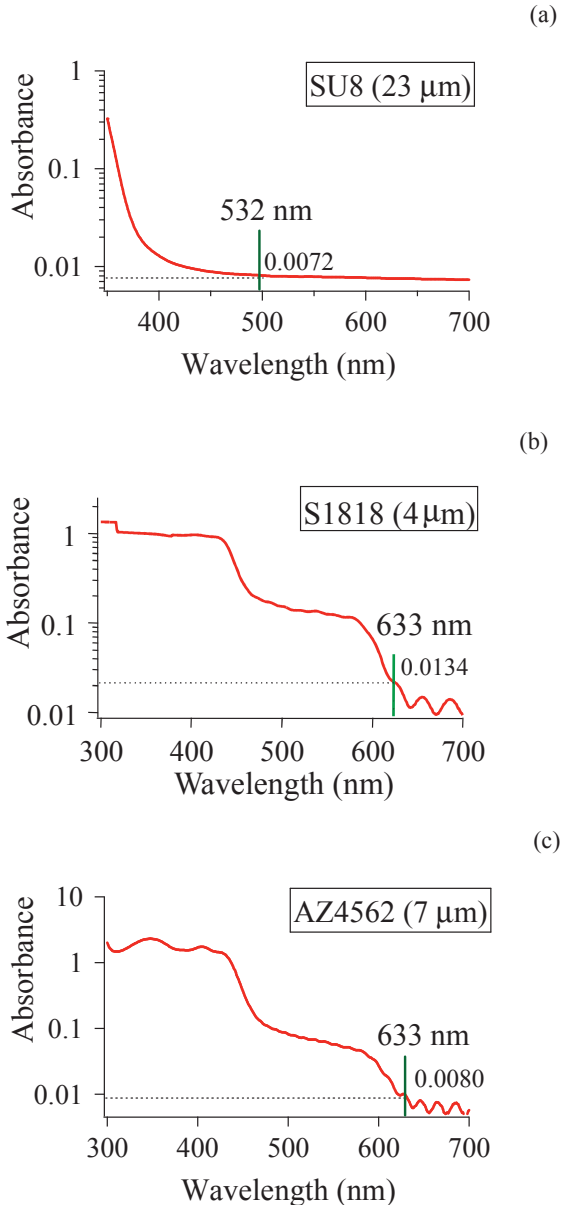

Figure 5.14: Absorption spectrums of SU-8 (a), S1818 (b), and AZ4562 (c), plotted in log scale.

and AZ4562 are shown in the Table 5.2.

5.5.2.2 Experimental procedures of LOPA DLW method

In order to adapt the LOPA principle, as compared to conventional OPA configuration, there are two issues need to be considered. The first one is the selection

photoresist	SC: S/A/T (rpm/(rpm/s)/s)	T_{SB} (min)	Thickness (μm)	Developer (min)	T_{PEB} at 95°C (min)
SU-8 2025	2500/300/30	3/15 (65/95°C)	25	15	15
S1818	2000/300/30	1 (115°C)	2	3	not required
AZ4562	2000/300/3*	1 (115°C)	18	1	not required

Table 5.2: The deposition parameters of photoresist layer on a glass substrate and its relevant developing parameters. SC : spin coating. S : spin speed (rpm); A : acceleration (rpm/s); T : duration time (s). T_{SB} : the time duration for soft baking (SB); T_{PEB} : time duration of post exposure baking (PEB) process. The asterisk (*) indicates that, after spin coating, the glass substrate have to stay over spin plate one minute before moving to hot plate.

of excitation light source, which has to be located in the LOPA region of target sample. In our experiment, according to the absorbance of studied materials (Figure 5.14): for SU-8 photoresist, we employed a laser beam operating at $\lambda = 532$ nm ($\sigma_{_{SU-8}} = 723$ m^{-1}); for S1818 and AZ4562, we used a light beam with a wavelength of $\lambda = 633$ nm ($\sigma_{_{S1818}} = 9200$ m^{-1}, $\sigma_{_{AZ4562}} = 2656$ m^{-1}). The second one is the use of an OL with a significant high NA to perform high contrast intensity distribution in the focal region. In our experiment, an oil immersion OL with NA = 1.4, ($n = 1.515$) is employed.

The experimental setup has been shown earlier in Figure 4.1 (see Chapter 4).

As illustrated in Figure 5.13, depends on used materials properties and the dimension of desired structures, the fabrication procedure of sub-micrometer structures are slightly different.

(SU-8): as shown in Figure 5.13(b), for the fabrication of a 3D structure based on SU-8, basically three steps are needed: writing a desired structure by DLW, thermal cross-linking of epoxy by post exposure bake (PEB), and development. The relevant parameters of PEB and developing time are shown in Table 5.2.

(S1818): as shown in Figure 5.13(c_1), for the fabrication of 2D arbitrary structures based on this positive photoresist S1818, which is not a chemically amplified resist, after exposure, a PEB step is required. It only needs two steps: DLW and development. (Figure 5.13(c_1)).

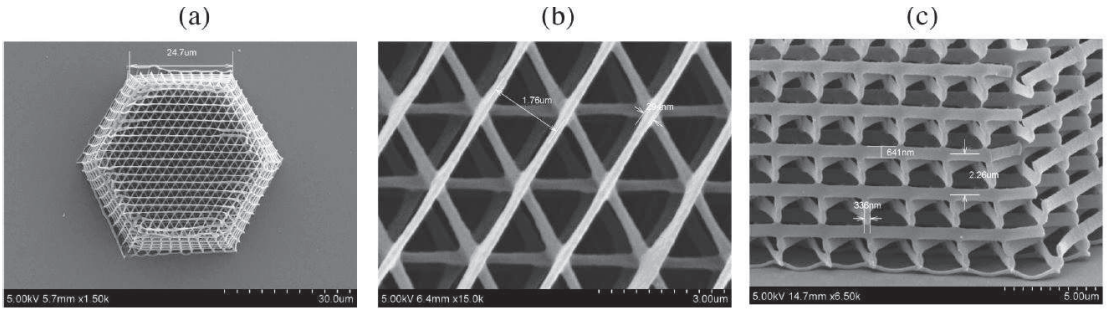

Figure 5.15: SEM image of a chiral structure fabricated with the following parameters: distance between rods = 2 μm; distance between layers = 0.75 μm; number of layers = 20; laser power = 2.8 mW. (a) View of the whole structure, (b) Zoom in on the top surface of the structure, and (c) Side view of the structure.

(AZ4562): as shown in Figure 5.13(c_2), compared to thin layers of S1818 (2 μm), the fabrication of 3D prototype structure is quite complex. It is due to the fact that, for positive photoresist, in order to obtain an isolated structure, a certain outside part of structure needs to be removed. In this case, by using the DLW method to remove outside part takes tedious time. Thus, in our experiment, we proposed to use UV lithography to primarily create a microscale base structure, and then by using LOPA DLW, the desired pattern inside this microscale structure is obtained.

By setting appropriate parameters of LOPA DLW, we have successfully fabricated 2D and 3D structures, which are in sub-micrometer scale.

5.5.3 Fabrication of 3D sub-micrometer structure by LOPA microscopy

By using LOPA DLW method, we can realize arbitrary 3D structure based on the SU-8 photoresist, for example, 3D chiral structures as shown in Figure 5.15. It shows clearly that the structures features are well separated, layer by layer in the horizontal and in vertical directions, feature sizes are about 300nm (horizontal) and 650 nm (vertical) as shown in Figure 5.15(c). For the fabrication of these structures, the focusing spot was scanned continuously with a scanning speed of about 1.34 μm/s. In order to clarify the OPA fabrication realized at this low absorption range, we have investigated the fabrication of A single voxel and measure its size as a function of the exposure time and the fluorescence intensity in SU-8 as a function of the

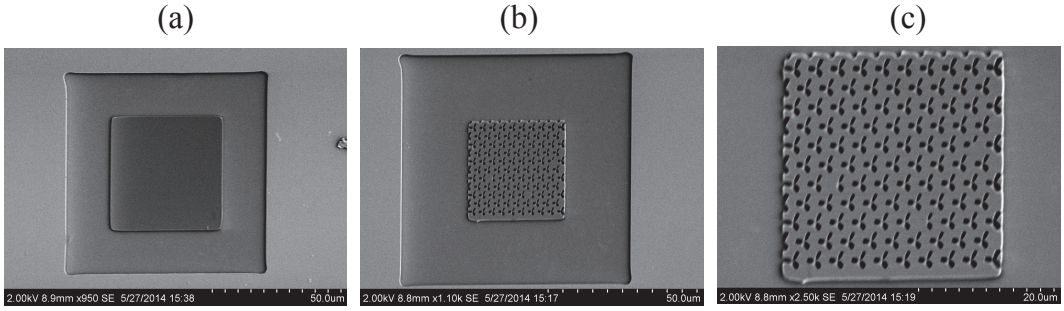

Figure 5.16: SEM images of fabricated 2D structures based on the positive photoresist. (a) First step of fabrication. Target area with removed outside part. (b) View of the whole fabricated 2D structure. (c) Zoom in of (a_2). The structures are obtained with the laser ($\lambda = 633$ nm) power = 110 μW.

excitation intensity [62]. Results show that the voxel size depends on the exposure dose rather than the intensity threshold as in TPA mechanism. The results from later investigation showed that the fluorescence intensity shows a linear dependence on the excitation intensity. Both results are strong evidence of the OPA mechanism. Further detail of these two tests can be referred to the paper [62].

The results that obtained by LOPA DLW method are similar as those derived from TPA DLW. But as compared to TPA DLW, here, only a continuous laser ($\lambda_{ex} = 532$ nm) with a very low power (2.5 mW) can be able to produce high spatial resolution arbitrary 3D structures.

LOPA DLW method is not only works for SU-8 negative photoresist, if the excitation wavelength of incident beam is carefully selected to LOPA condition, in principle it is able to fabricate any kinds of arbitrary 2D or 3D structures from numerous types of photoresist as TPA does. In the next subsection we will present the fabrication of 2D and 3D structures fabricated from positive photoresist.

5.5.4 Fabrication of 2D, 3D structures from a positive photoresist

Nowadays, due to the unique properties, such as sharp edge and with less dark erosion, the fabrication of nano- or micro-structures based on positive photoresist is taking more attention. In these resists, due to the depolymerization of the exposed area, which has much faster dissolution rate ($> 10^2$ times) than the unexposed area in an alkaline solution, after the developing process, the inverse of the written

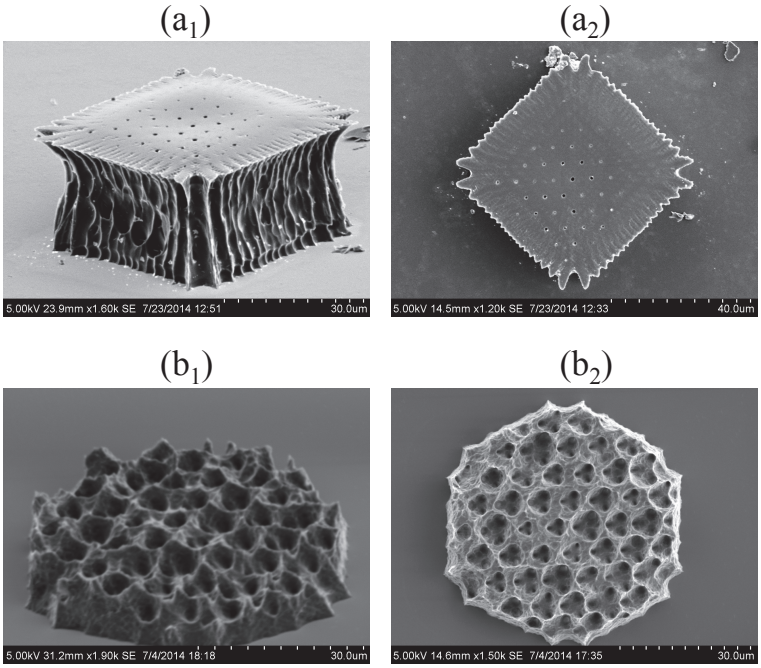

Figure 5.17: SEM images of fabricated 3D scaffold structures inside in cube (a) and hexagonal structures (b). [(a_1), (b_1)]: side view; [(a_2), (b_2)]: top view. The structures obtained with the laser power = 115 μW, λ_{ex} = 633 nm.

structure is obtained. One of the most important applications of positive photoresist is the fabrication of porous structures, which are subsequently filled with liquid crystals or electro-optic polymers to generate a tunable photonic crystal device [93].

By using the LOPA DLW method, the fabricated 2D structure from S1818 is shown in Figure 5.16. The used laser (λ = 633 nm) power is only 110 μW. In order to obtain an isolated structure from positive resist, the edge part of desired structure has to be removed. In this case, the thickness of the deposited S1818 resist is around 2 μm, which can be easily deal with DLW method (Figure 5.16) (a)). In Figure 5.16[(b), (c)], the complete fabricated structures shows clearly the well separated array of three-leaf pattern, in which the hole size is around 600 nm. The size of the hole can be further reduced by decreasing the intensity of excitation beam. This structure has many interesting applications, for example, it can be filled with gold to study plasmonic and nonlinear effect.

As shown in Figure 5.17, we tried to fabricate 3D scaffold structure in micro cuboid and hexagon shapes, which are obtained by UV lithography. Unfortunately, due to the often faced positive resist problem, related to the insoluble surface layer

[94], the developing process become complicated (Figure 5.17(a_1, a_2)). One more possible reason is that, as compared to the absorption of SU-8 at 532 nm (723 m^{-1}), in this case, the used AZ4652 resist at wavelength 633 nm, possesses not a significant low absorption (2656 m^{-1}). Hence, after a long fabrication process, the top laser is over exposed and developed out (Figure 5.17(b_1, b_2)). Since, it is only the matter of material effect instead of LOPA microscopy limitations, several solutions can be applied. For example, the insoluble layer can be avoided by implementing the fabrication process in an activated carbon filtration system [94]. Concerning the absorption spectrum of the studied material, we can choose an appropriate laser source, at which it has a significant low absorption. This will be our future work.

Conclusion of chapter 5

In conclusion, in this chapter, we have theoretically and experimentally investigated in detail the propagation of a tightly focused beam in an absorbing media and a novel method for 3D imaging and 3D fabrication, which based on low one-photon absorption (LOPA). The numerical calculation results of PSF, which takes into account the absorption of the material, shows that the intensity and focusing spot shape strongly depend on the absorption coefficient and the NA of the used OL. Indeed, on one hand, when the material presents very low linear absorption at a chosen excitation laser wavelength, the light intensity of a collimated light beam keeps almost unchanged through the propagation inside the material. On the other hand, by using a high NA OL, the light beam will be tightly focused, resulting in a very high intensity at the focusing spot. Combining low linear absorption effect and high NA OL, the sub-micrometric focusing spot keeps almost the same shape at any position inside the studied material. This combination allows to optically address 3D objects, equivalent to those achieved by using two-photon absorption technique. The theoretical calculations are experimentally verified by focusing a laser beam, with different excitation wavelengths, inside a Rhodamine 6G solution. The experimental results show a great enhancement of penetration depth, similar to what can be obtained by two-photon absorption microscopy, but this LOPA technique presents many advantages, since it requires only a simple setup and a low-cost and low power continuous laser. This LOPA based microscopy is very promising for submicrometric 3D imaging and 3D fabrication, as well as 3D data

storage.

Conclusion and Prospects

In summary, in this work, we have theoretically and experimentally studied in detail the point spread function under tight focusing conditions and its applications to optical imaging and nano-fabrication.

First, *based on vectorial Debye theory, we have theoretically predicted the field distribution in the focal region of high NA OLs. The numerical results showed that, when a light field is strongly confined into a sub-micrometer scale, the tiny focusing spot is affected by numerous parameters. We have systematically studied the influence of beam mode, polarization, phase distribution of incident beam on the polarization and intensity distributions of the focusing spot. The focal shift of the focusing spot caused by refractive index mismatch has also been presented. These basic studies of PSF are very important for optical microscopy applications.*

Second, *according to the increasing demands of particular field distributions in the focal region in many disciplines, we have studied the shaping of the intensity and polarization distributions of the EM field in the focal region. We proposed different methods to generate a long needle, long dark channel and flattop focusing spot. Moreover, we presented the polarization distribution in the focal region and introduced methods for the generation of longitudinally or pure-transversely polarized field distributions in the focal region. These generated focusing spots with particular polarization or intensity distributions are very important for many applications, such as particle acceleration, single molecule detection and optical data storage.*

Third, *we have presented the working principle of 2D and 3D super-resolution optical microscopy for imaging and optical fabrication. We studied the two dimen-*

sional STED microscopy and AMOL in detail and further investigated the generation of a super-resolution nano-pointer for optical fabrication application. Furthermore, according to the unique properties of radially polarized light, we have proposed a new method for the creation of 3D doughnut focusing spot for 3D STED microscopy. Compared to the conventional way to obtain 3D doughnut focusing spot, this method, in which only one laser beam combined with one-dark ring mask, can generate 3D doughnut spot, which greatly simplifies the experimental configuration and the cost.

Forth, *we have used a simple but effective experimental method to characterize the numerous important properties of tightly focused light in the focal region. The experimental configuration is that, a home-made confocal microscope constituted by a high NA OL was employed to scan the fluorescence image of single gold NPs (probe bead) to reconstruct the intensity distribution of the focusing spot. By using this experiment, we have experimentally demonstrated the influences of NA of OL, refractive index mismatch, on the intensity distributions of focusing spot. Furthermore, we have successfully demonstrated the influence of incident beam polarization on the shape of focusing spot.*

Fifth, *We investigated for the first time the intensity distribution of the point spread function (PSF), taking into account the absorption of material in which light propagates. Furthermore, we proposed a novel method for three-dimensional (3D) optical addressing based on low one-photon absorption (LOPA). LOPA microscopy is an very powerful technique to deal with 3D imaging and 3D fabrication. The derived results are similar to those obtained by two-photon absorption microscopy, but this LOPA technique presents many advantages, since it requires only a simple setup and a low-cost, low power continuous laser.*

In future prospects, for theoretical aspects, based on this thesis work, we will continue to investigate the generation of 3D isotropic Airy spots. Moreover, according to the potential PSF to calculate the inverse field distribution on the OL pupil is also an interesting work. For experimental aspects, using the LOPA method to fabricate 3D porous structure is one of our most interested works. Furthermore, using nano-structures to control light flow or for sensing applications are also our interests.

Appendix A: Matlab script for PSF calculation

Matlab example for simulation of intensity distribution of focusing spot at $(x_2 y_2)-$plane as a function of input beam polarization

```
%initialize Matlab environment
clear
close all
clc
tic;
set(0,'DefaultAxesFontName', 'Times New Roman')
set(0,'DefaultAxesFontSize', 11)
%set(0,'DefaultUnits','normalized');
set(0,'defaultuicontrolunits','normalized');
%%%%%%%%%%program  body %%%%%%%%%%%%%
% basic parameters
NA=1.4;                          % numerical aperture of objective lens
n=1.515;                         % refractive index of immersion medium
lambda=532e-9;                   % wavelength of light
alpha=asin(NA/n);                % maximum open angle of OL
k=2*pi*n/lambda;                 % wavenumber

% image plane in Cartesian coordinates
L_focal=0.5*1e-6;                          % observation scale
Nx=50;                           % discretization of image plane
Ny=50;                           % discretization of image plane
x2=linspace(-L_focal,L_focal,Nx);
y2=linspace(-L_focal,L_focal,Ny);
[X2,Y2]=meshgrid(x2,y2);
Z2=0;

% polarization case
% '1': x-linear, '2':y-linear, '3': left circular
% '4': right circular, '5': elliptical, '6': radial, '7': azimuthal
polar=1;
polarSTR=num2str(polar);
```

```
%normalization and steps of integral
Ex2=0;                              % Ex-component in focal
Ey2=0;                              % Ey-component in focal
Ez2=0;                              % Ez-component in focal
N_theta=50;
N_phi=50;
delta_theta=alpha/N_theta;
delta_phi=2*pi/N_phi;

% starting loop
for theta=eps:delta_theta:alpha
    for phi=eps:delta_phi:2*pi
        %convertion function of polarization from object plane to imaging
        %plane
        a=1+(cos(theta)-1)*(cos(phi))^2;
        b=(cos(theta)-1)*cos(phi)*sin(phi);
        c=-sin(theta)*cos(phi);
        d=1+(cos(theta)-1)*(sin(phi))^2;
        e=-sin(theta)*sin(phi);
        ff=cos(theta);
        V=[a b c;b d e;-c -e ff];
        %incident beam polarization cases
        px=[1,0,1/sqrt(2),1i/sqrt(2),2/sqrt(5),cos(phi),-sin(phi)];
        py=[0,1,1i/sqrt(2),1/sqrt(2),1i/sqrt(5),sin(phi),cos(phi)];
        pz=0;
        % selected incident beam polarization
        P=[px(1,polar);py(1,polar);pz];
        % polarization in focal region
        PP=V*P;

        % numerical calculation of field distribution in focal region
            Ex2=Ex2+1i*sin(theta)*sqrt(cos(theta)).*PP(1,1).*exp(1i*k*(Z2*cos(theta
                )+sin(theta).*(X2*cos(phi)+Y2*sin(phi))))*delta_theta*delta_phi;
            Ey2=Ey2+1i*sin(theta)*sqrt(cos(theta)).*PP(2,1).*exp(1i*k*(Z2*cos(theta
                )+sin(theta).*(X2*cos(phi)+Y2*sin(phi))))*delta_theta*delta_phi;
            Ez2=Ez2+1i*sin(theta)*sqrt(cos(theta)).*PP(3,1).*exp(1i*k*(Z2*cos(theta
                )+sin(theta).*(X2*cos(phi)+Y2*sin(phi))))*delta_theta*delta_phi;

    end
end

% intensity of different components and total field
Ix2=conj(Ex2).*(Ex2);
Iy2=conj(Ey2).*(Ey2);
Iz2=conj(Ez2).*(Ez2);
I1=Ix2+Iy2+Iz2;
%find maxumum
MM1=max(max(I1));

% plot data
figure (1)
hFig = figure(1);
```

```
81  set(gcf,'PaperPositionMode','auto')
82  set(hFig, 'Position', [300 300 300 300])
83  p=axes;
84  set(p,'Position',[0 0 1 1])
85  pcolor(X2*1e6,Y2*1e6,Ix2);
86  shading interp
87  title('PSF as a fuction of different polarization')
88  set(gca,'Xtick',[-L_focal 0 L_focal]);
89  set(gca,'Ytick',[-L_focal 0 L_focal]);
90  set(gca,'FontSize',12)
91  axis equal
92  axis tight
93  axis off
94  view(0,90);
95  hold off
96  colormap(hot)
97
98  % export figure & save data
99  dataname=['polar=',polarSTR];
100 PexportJpg(hfig,40,24,dataname);
101 saveas(h,[figurename1,'.fig']);
102 save([dataname,'.txt'], 'I1','-ascii');
103
104 toc % count execution time
105 load chirp % ringtone for program alert
106 sound(y,Fs)
107 % % % % % % % % %end program% % % % % % % % % % % % % %
```

Bibliography

[1] Tony Wilson. Confocal microscopy. *Academic Press: London, etc*, 426:1–64, 1990.

[2] Stefan W Hell and Jan Wichmann. Breaking the diffraction resolution limit by stimulated emission: stimulated-emission-depletion fluorescence microscopy. *Optics letters*, 19(11):780–782, 1994.

[3] Suliana Manley, Jennifer M Gillette, George H Patterson, Hari Shroff, Harald F Hess, Eric Betzig, and Jennifer Lippincott-Schwartz. High-density mapping of single-molecule trajectories with photoactivated localization microscopy. *Nature methods*, 5(2):155–157, 2008.

[4] D. A. Parthenopoulos and P. M. Rentzepis. Three-dimensional optical storage memory. *Science*, 245(4920):843–845, 1989.

[5] Bo Huang, Mark Bates, and Xiaowei Zhuang. Super resolution fluorescence microscopy. *Annual review of biochemistry*, 78:993, 2009.

[6] Hong-Bo Sun, Makoto Maeda, Kenji Takada, James WM Chon, Min Gu, and Satoshi Kawata. Experimental investigation of single voxels for laser nanofabrication via two-photon photopolymerization. *Applied physics letters*, 83(5):819–821, 2003.

[7] Vygantas Mizeikis, Kock Khuen Seet, Saulius Juodkazis, and Hiroaki Misawa. Three-dimensional woodpile photonic crystal templates for the infrared spectral range. *Optics letters*, 29(17):2061–2063, 2004.

[8] David G Grier. A revolution in optical manipulation. *Nature*, 424(6950):810–816, 2003.

[9] Kishan Dholakia and Peter Reece. Optical micromanipulation takes hold. *Nano today*, 1(1):18–27, 2006.

[10] Peter J Shaw. Comparison of widefield/deconvolution and confocal microscopy for three-dimensional imaging. In *Handbook of biological confocal microscopy*, pages 453–467. Springer, 2006.

[11] M. Farsari and B. N. Chichkov. Materials processing: Two-photon fabrication. *Nature Photonics*, 3(8):450, 2009.

[12] DW Pohl, W Denk, and M Lanz. Optical stethoscopy: Image recording with resolution $\lambda/20$. *Applied physics letters*, 44(7):651–653, 1984.

[13] Rajesh Menon and Henry I Smith. Absorbance-modulation optical lithography. *JOSA A*, 23(9):2290–2294, 2006.

[14] Mark R Dennis, Kevin O'Holleran, and Miles J Padgett. Singular optics: optical vortices and polarization singularities. *Progress in Optics*, 53:293–363, 2009.

[15] Birka Hein, Katrin I Willig, and Stefan W Hell. Stimulated emission depletion (sted) nanoscopy of a fluorescent protein-labeled organelle inside a living cell. *Proceedings of the National Academy of Sciences*, 105(38):14271–14276, 2008.

[16] D Wildanger, R Medda, L Kastrup, and SW Hell. A compact sted microscope providing 3d nanoscale resolution. *Journal of microscopy*, 236(1):35–43, 2009.

[17] E. Hecht. *Optics*. Pearson education. Addison-Wesley, 2002.

[18] Scott Marshall Mansfield and GS Kino. Solid immersion microscope. *Applied physics letters*, 57(24):2615–2616, 1990.

[19] Min Gu. *Advanced optical imaging theory*, volume 75. Springer, 1999.

[20] E. Wolf. Electromagnetic diffraction in optical systems I. an integral representation of the image field. *Proc. Roy. Soc. A*, 253(1274):349–357, 1959.

[21] Kathleen Youngworth and Thomas Brown. Focusing of high numerical aperture cylindrical-vector beams. *Optics Express*, 7(2):77–87, 2000.

[22] B Richards and E Wolf. Electromagnetic diffraction in optical systems. II. structure of the image field in an aplanatic system. *Proceedings of the Royal Society of London. Series A. Mathematical and Physical Sciences*, 253(1274):358–379, 1959.

[23] Lars Egil Helseth. Focusing of atoms with strongly confined light potentials. *Optics communications*, 212(4):343–352, 2002.

[24] Xiang Hao, Cuifang Kuang, Tingting Wang, and Xu Liu. Effects of polarization on the de-excitation dark focal spot in sted microscopy. *Journal of Optics*, 12(11):115707, 2010.

[25] Stefan Hell and Ernst HK Stelzer. Properties of a 4pi confocal fluorescence microscope. *JOSA A*, 9(12):2159–2166, 1992.

[26] CJR Sheppard and T Wilson. Gaussian-beam theory of lenses with annular aperture. *IEE Journal on Microwaves, Optics and Acoustics*, 2(4):105–112, 1978.

[27] Haifeng Wang, Luping Shi, Boris Lukyanchuk, Colin Sheppard, and Chong Tow Chong. Creation of a needle of longitudinally polarized light in vacuum using binary optics. *Nature Photonics*, 2(8):501–505, 2008.

[28] Yuichi Kozawa and Shunichi Sato. Focusing property of a double-ring-shaped radially polarized beam. *Optics letters*, 31(6):820–822, 2006.

[29] Takahiro Kuga, Yoshio Torii, Noritsugu Shiokawa, Takuya Hirano, Yukiko Shimizu, and Hiroyuki Sasada. Novel optical trap of atoms with a doughnut beam. *Physical Review Letters*, 78(25):4713, 1997.

[30] Travis J Gould, Daniel Burke, Joerg Bewersdorf, and Martin J Booth. Adaptive optics enables 3d sted microscopy in aberrating specimens. *Optics express*, 20(19):20998–21009, 2012.

[31] Zongsong Gan, Yaoyu Cao, Richard A Evans, and Min Gu. Three-dimensional deep sub-diffraction optical beam lithography with 9 nm feature size. *Nature communications*, 4, 2013.

[32] Joel M Murray, Jean Wei, Jacob O Barnes, Jonathan E Slagle, and Shekhar Guha. Measuring refractive index using the focal displacement method. *Applied Optics*, 53(17):3748–3752, 2014.

[33] Lars Egil Helseth. Roles of polarization, phase and amplitude in solid immersion lens systems. *Optics communications*, 191(3):161–172, 2001.

[34] P Török, P Varga, Z Laczik, and GR Booker. Electromagnetic diffraction of light focused through a planar interface between materials of mismatched refractive indices: an integral representation. *JOSA A*, 12(2):325–332, 1995.

[35] P Török, P Varga, A Konkol, and GR Booker. Electromagnetic diffraction of light focused through a planar interface between materials of mismatched refractive indices: structure of the electromagnetic field. ii. *JOSA A*, 13(11):2232–2238, 1996.

[36] K Sakai and S Noda. Optical trapping of metal particles in doughnut-shaped beam emitted by photonic-crystal laser. *Electronics Letters*, 43(2):107–108, 2007.

[37] K Lalithambigai, P Suresh, V Ravi, K Prabakaran, Z Jaroszewicz, KB Rajesh, PM Anbarasan, and TVS Pillai. Generation of sub wavelength super-long dark channel using high na lens axicon. *Optics letters*, 37(6):999–1001, 2012.

[38] Wei Han, Wen Cheng, and Qiwen Zhan. Flattop focusing with full poincaré beams under low numerical aperture illumination. *Optics letters*, 36(9):1605–1607, 2011.

[39] Nils Huse, Andreas Scho, Stefan W Hell, et al. Z-polarized confocal microscopy. *Journal of biomedical optics*, 6(3):273–276, 2001.

[40] Rasheed MA Azzam and Nicholas Mitchell Bashara. *Ellipsometry and polarized light*. North-Holland. sole distributors for the USA and Canada, Elsevier Science Publishing Co., Inc., 1987.

[41] Yan Sheng et al. Cerenkov-type second-harmonic generation in two-dimensional nonlinear photonic structures. *IEEE Journal of Quantum Electronics*, 45(11):1465–1472, 2009.

[42] Kyoko Kitamura, Kyosuke Sakai, and Susumu Noda. Sub-wavelength focal spot with long depth of focus generated by radially polarized, narrow-width annular beam. *Optics Express*, 18(5):4518–4525, 2010.

[43] Bo Tian and Jixiong Pu. Tight focusing of a double-ring-shaped, azimuthally polarized beam. *Optics letters*, 36(11):2014–2016, 2011.

[44] Ralf Dorn, S Quabis, and G Leuchs. Sharper focus for a radially polarized light beam. *Physical review letters*, 91(23):233901, 2003.

[45] HM Haskal. Laser recording with truncated gaussian beams. *Applied optics*, 18(13):2143–2146, 1979.

[46] Yajun Li. Light beams with flat-topped profiles. *Optics letters*, 27(12):1007–1009, 2002.

[47] Qiwen Zhan and James Leger. Focus shaping using cylindrical vector beams. *Optics Express*, 10(7):324–331, 2002.

[48] Marlan O Scully. A simple laser linac. *Applied Physics B*, 51(3):238–241, 1990.

[49] Dennis McPhail and Min Gu. Use of polarization sensitivity for three-dimensional optical data storage in polymer dispersed liquid crystals under two-photon illumination. *Applied physics letters*, 81(7):1160–1162, 2002.

[50] Ngoc Diep Lai, Jian Hung Lin, Po Wen Chen, Jaw Luen Tang, and Chia Chen Hsu. Controlling aspect ratio of focal spots of high numerical aperture objective lens in multi-photon absorption process. *Optics communications*, 258(2):97–102, 2006.

[51] Stefan W Hell. Far-field optical nanoscopy. *science*, 316(5828):1153–1158, 2007.

[52] Dominik Wildanger, Brian R Patton, Heiko Schill, Luca Marseglia, JP Hadden, Sebastian Knauer, Andreas Schönle, John G Rarity, Jeremy L O'Brien, Stefan W Hell, et al. Solid immersion facilitates fluorescence microscopy with nanometer resolution and sub-ångström emitter localization. *Advanced Materials*, 24(44):OP309–OP313, 2012.

[53] Volker Westphal and Stefan W Hell. Nanoscale resolution in the focal plane of an optical microscope. *Physical review letters*, 94(14):143903, 2005.

[54] Joachim Fischer, Georg von Freymann, and Martin Wegener. The materials challenge in diffraction-unlimited direct-laser-writing optical lithography. *Advanced materials*, 22(32):3578–3582, 2010.

[55] Na Liu, Hongcang Guo, Liwei Fu, Stefan Kaiser, Heinz Schweizer, and Harald Giessen. Three-dimensional photonic metamaterials at optical frequencies. *Nature materials*, 7(1):31–37, 2007.

[56] Nadia Belabas, Sophie Bouchoule, Isabelle Sagnes, Juan Ariel Levenson, Christophe Minot, and Jean-Marie Moison. Confining light flow in weakly coupled waveguide arrays by structuring the coupling constant: towards discrete diffractive optics. *Optics express*, 17(5):3148–3156, 2009.

[57] Xiangping Li, Yaoyu Cao, and Min Gu. Superresolution-focal-volume induced 3.0 tbytes/disk capacity by focusing a radially polarized beam. *Optics letters*, 36(13):2510–2512, 2011.

[58] Timothy F Scott, Benjamin A Kowalski, Amy C Sullivan, Christopher N Bowman, and Robert R McLeod. Two-color single-photon photoinitiation and photoinhibition for subdiffraction photolithography. *Science*, 324(5929):913–917, 2009.

[59] Yaoyu Cao, Zongsong Gan, Baohua Jia, Richard A Evans, and Min Gu. High-photosensitive resin for super-resolution direct-laser-writing based on photoinhibited polymerization. *Optics express*, 19(20):19486–19494, 2011.

[60] Trisha L Andrew, Hsin-Yu Tsai, and Rajesh Menon. Confining light to deep subwavelength dimensions to enable optical nanopatterning. *Science*, 324(5929):917–921, 2009.

[61] Hsin-Yu Sidney Tsai. *Absorbance modulation optical lithography*. PhD thesis, Massachusetts Institute of Technology, 2007.

[62] Mai Trang Do, Thi Thanh Ngan Nguyen, Qinggele Li, Henri Benisty, Isabelle Ledoux-Rak, and Ngoc Diep Lai. Submicrometer 3d structures fabrication enabled by one-photon absorption direct laser writing. *Optics express*, 21(18):20964–20973, 2013.

[63] Qinggele Li, Mai Trang Do, Isabelle Ledoux-Rak, and Ngoc Diep Lai. Concept for three-dimensional optical addressing by ultralow one-photon absorption method. *Optics letters*, 38(22):4640–4643, 2013.

[64] GP Karman, A Van Duijl, MW Beijersbergen, and JP Woerdman. Measurement of the three-dimensional intensity distribution in the neighborhood of a paraxial focus. *Applied optics*, 36(31):8091–8095, 1997.

[65] R Juškaitis and T Wilson. The measurement of the amplitude point spread function of microscope objective lenses. *J. Microsc*, 189(1):8–11, 1998.

[66] Rimas Juškaitis. Measuring the real point spread function of high numerical aperture microscope objective lenses. In *Handbook of biological confocal microscopy*, pages 239–250. Springer, 2006.

[67] Peter Török and Fu-Jen Kao. Point-spread function reconstruction in high aperture lenses focusing ultra-short laser pulses. *Optics communications*, 213(1):97–102, 2002.

[68] InCheon Song, HongKi Yoo, Jaebum Choo, and Dae-Gab Gweon. Measurement of point-spread function (psf) for confocal fluorescence microscopy. In *Optics & Photonics 2005*, pages 58781B–58781B. International Society for Optics and Photonics, 2005.

[69] H Yoo, I Song, and D-G GWEON. Measurement and restoration of the point spread function of fluorescence confocal microscopy. *Journal of microscopy*, 221(3):172–176, 2006.

[70] Richard W Cole, Tushare Jinadasa, and Claire M Brown. Measuring and interpreting point spread functions to determine confocal microscope resolution and ensure quality control. *Nature protocols*, 6(12):1929–1941, 2011.

[71] A. Ashkin, J. M. Dziedzic, and T. Yamane. Optical trapping and manipulation of single cells using infrared laser beams. *Nature*, 330(6150):769–771, 1987.

[72] M. Deubel, M. Von Freymann, G.and Wegener, S. Pereira, K. Busch, and C. M. Soukoulis. Direct laser writing of three-dimensional photonic-crystal templates for telecommunications. *Nature Materials*, 3(7):444–447, 2004.

[73] S. K. Rhodes, K. A. Nugent, and A Roberts. Precision measurement of the electromagnetic fields in the focal region of a high-numerical-aperture lens using a tapered fiber probe. *JOSA A*, 19(8):1689–1693, 2002.

[74] Ralf Dorn, Susanne Quabis, and Gerd Leuchs. The focus of light-linear polarization breaks the rotational symmetry of the focal spot. *Journal of modern optics*, 50(12):1917–1926, 2003.

[75] C. Huber, S. Orlov, P. Banzer, and G. Leuchs. Corrections to the knife-edge based reconstruction scheme of tightly focused light beams. *Optics Express*, 21(21):25069–25076, 2013.

[76] James Pawley. *Handbook of biological confocal microscopy*. Springer, 2010.

[77] DB Hovis and AH Heuer. The use of laser scanning confocal microscopy (lscm) in materials science. *Journal of microscopy*, 240(3):173–180, 2010.

[78] Rishi Kant. An analytical solution of vector diffraction for focusing optical systems with seidel aberrations: I. spherical aberration, curvature of field, and distortion. *Journal of Modern Optics*, 40(11):2293–2310, 1993.

[79] Rishi Kant. An analytical method of vector diffraction for focusing optical systems with seidel aberrations ii: Astigmatism and coma. *Journal of Modern Optics*, 42(2):299–320, 1995.

[80] B. Simon and O. Haeberlé. Multi-kernel deconvolution applied to confocal fluorescence microscopy with engineered point spread function. *Journal of the European Optical Society-Rapid publications*, 1(0):06028, 2006.

[81] DF Swinehart. The beer-lambert law. *Journal of chemical education*, 39(7):333, 1962.

[82] Bo Huang, Wenqin Wang, Mark Bates, and Xiaowei Zhuang. Three-dimensional super-resolution imaging by stochastic optical reconstruction microscopy. *Science*, 319(5864):810–813, 2008.

[83] Winfried Denk, James H Strickler, Watt W Webb, et al. Two-photon laser scanning fluorescence microscopy. *Science*, 248(4951):73–76, 1990.

[84] Nicholas G Horton, Ke Wang, Demirhan Kobat, Catharine G Clark, Frank W Wise, Chris B Schaffer, and Chris Xu. In vivo three-photon microscopy of subcortical structures within an intact mouse brain. *Nature photonics*, 7(3):205–209, 2013.

[85] Marius A Albota, Chris Xu, and Watt W Webb. Two-photon fluorescence excitation cross sections of biomolecular probes from 690 to 960 nm. *Applied optics*, 37(31):7352–7356, 1998.

[86] SA Prahl, M Keijzer, SL Jacques, and AJ Welch. A monte carlo model of light propagation in tissue. *Dosimetry of laser radiation in medicine and biology*, 5:102–11, 1989.

[87] S Kunzelmann and M. R Webb. Fluorescence detection of gdp in real time with the reagentless biosensor rhodamine–parm. *J. Biochemical*, 440(Pt 1):43–49, 2011.

[88] Camille Delezoide, Isabelle Ledoux-Rak, and Chi Thanh Nguyen. General approach for the sensitivity analysis and optimization of integrated optical evanescent-wave sensors. *JOSA B*, 31(4):851–859, 2014.

[89] Marc D Levenson, NS Viswanathan, and Robert A Simpson. Improving resolution in photolithography with a phase-shifting mask. *Electron Devices, IEEE Transactions on*, 29(12):1828–1836, 1982.

[90] Ngoc D Lai, Jian H Lin, Yi Y Huang, and Chia C Hsu. Fabrication of two-and three-dimensional quasi-periodic structures with 12-fold symmetry by interference technique. *Optics express*, 14(22):10746–10752, 2006.

[91] Heike Ebendorff-Heidepriem. Laser writing of waveguides in photosensitive glasses. *Optical Materials*, 25(2):109–115, 2004.

[92] Stephen Y Chou, Peter R Krauss, and Preston J Renstrom. Imprint of sub-25 nm vias and trenches in polymers. *Applied physics letters*, 67(21):3114–3116, 1995.

[93] Jiaqi Chen, Wei Jiang, Xiaonan Chen, Li Wang, Sasa Zhang, and Ray T Chen. Holographic three-dimensional polymeric photonic crystals operating in the 1550nm window. *Applied Physics Letters*, 90(9):093102, 2007.

[94] Hiroshi Ito. Chemical amplification resists for microlithography. In *Microlithography· Molecular Imprinting*, pages 37–245. Springer, 2005.